OUKA
The University of Osaka
Institutional Knowledge Archive

Title	Experimental Studies of Haldane Gap Antiferromagnet and Heavy Fermion Superconductor under Complex Extreme Conditions
Author(s)	幸田, 章宏
Citation	大阪大学, 1998, 博士論文
Version Type	VoR
URL	https://doi.org/10.11501/3144075
rights	
Note	

The University of Osaka Institutional Knowledge Archive : OUKA

https://ir.library.osaka-u.ac.jp/

The University of Osaka

#6491

Experimental Studies of Haldane Gap Antiferromagnet and Heavy Fermion Superconductor under Complex Extreme Conditions

by
Akihiro KODA

Osaka University
Graduate School of Engineering Science
Department of Material Physics
Toyonaka, Osaka

January 1998

To my past father
and
all victims of the Hanshin Awaji disaster.

Contents

Abstract

The Haldane gap antiferromagnet $Ni(C_5H_{14}N_2)_2N_3ClO_4$ (NDMAZ) and the heavy fermion superconductor UPt_3 have been studied under complex extreme conditions.

The heat capacity and the magnetization measurements of the single crystal of NDMAZ were carried out at low temperatures down to 0.1K and under magnetic fields up to 14T. We have observed three dimensional long range ordering of NDMAZ under magnetic field of $H \simeq 13$T applied parallel to the crystal c axis and at temperature $T \simeq 0.3$K, which is ascribed to be due to both the field induced gap quenching and the existence of finite interchain interaction J' in the real system. Applying the higher external field, the transition temperature increases up to $\simeq 0.7$K at 14T, showing a negative curvature with respect to the external field.

The heat capacity and the magneto-caloric effect measurements of the single crystal UPt_3 were carried out at low temperatures down to 0.2K, under high magnetic field up to 2T and under high pressures up to 8.7kbar. The heat capacity obeys T^2 law both at ambient pressure and under high pressures. Above $P_c \sim 3$kbar, no evidence of the successive transition was observed. By analyzing the data of magneto-caloric effect separately for the reversible and the irreversible part, it clearly shows the existence of the B–C phase transition and H_{c2} both at ambient pressure and under high pressures at reached low temperature. An irreversible heat up was observed just below H_{c2}, which is attributed to the peak effect.

At higher temperatures and under lower magnetic fields, it is not able to determine the B–C phase transition by means of the magneto-caloric effect measurement because of the serious irreversible heating of UPt_3 and the H–T–P phase diagram is not determined yet.

Part I

Heat capacity under complex extreme conditions

Chapter 1

General introduction

In recent years, the attention to complex extreme conditions is increasing. Its applications as mighty tools to study the various aspects of condensed matter physics as well as the peculiar phenomena there have been attempted. The heat capacity has an advantage since its measurement technique is easy to be applied under extreme conditions. Moreover, heat capacity is a very basic physical property and the most definite measure to confirm the phase transition. Particularly, under very low temperatures, it gives useful information about the low-lying excited states which play an important role on the quantum fluctuation.

In Part I, the fundamental procedures of the experimental technique are emphasized.

In Part II, the heat capacity of the Haldane-gap antiferromagnet $Ni(C_5H_{14}N_2)_2N_3ClO_4$, abbreviated as NDMAZ, under high fields is reported. Haldane-gap problem is the main subject of a quantum spin chain system. In 1983, F.D.M.Haldane conjectured that one dimensional linear chain Heisenberg antiferromagnet (1D-HAF) should have an energy gap between the ground state singlet and the first excited states in case of an integer spin quantum number, while the energy levels are gapless in case of a half integer spin [1]. He reveals that the ground state of 1D-HAF differs from the quasi-classical one as before and claims that the spin chain must be treated as a quantum many body system.

If Haldane-gap exists, three dimensional long-range order (3D-LRO) of the spin system does not occur down to T=0K because of the non-magnetic ground state even though the relatively smaller interchain interaction than the energy gap exists. However, under the external fields, upper magnetic excited states mixes with the ground state at a certain critical field H_c and the possibility of 3D-LRO revives. The magnetic field effects of the Haldane system are almost backward region from the theoretical point of view. Such a field-induced ordered state is entirely unknown. Realizing 3D-LRO is interesting for the competitive picture between the quantum spin fluctuation of one dimensional system and the cooperative phenomena of three dimensional system.

Recently, Z.Honda *et al.* have reported the heat capacity of NDMAZ and presented a sharp peak at around 0.6K under the fields of 12T [2]. This compound is a candidate for proving the existance of 3D-LRO at low temperature by the gap-quenching because of the absence of transverse staggered magnetic moments. In fact, the existence of finite gap under application of the external magnetic field and the resulting absence of 3D-LRO in case of $Ni(C_2H_8N_2)_2NO_2ClO_4$, abbreviated as NENP, is confirmed in the previous experiments [3].

Although the heat capacity measurement is the most direct way to detect the phase

transition, a question about the technical problems remains. That is, the relaxation method which they adopted is not suitable one to analyze the data obtained under such extreme conditions of very low temperatures and high fields. Thus the verification is to be carried out with the relatively more quantitative adiabatic method. Simultaneously, if 3D-LRO exists, establishing the phase diagram and examining the ordered state, by means of the most direct method of heat capacity measurement are the most important in the Haldane gap problem.

Next, in Part III, results of the heat capacity measurements of the heavy fermion superconductor UPt_3 under high pressures and magnetic fields are reported. UPt_3 is a convinced candidate of the triplet superconductor. It presents a quite impressive superconducting phase diagram, giving three distinct superconducting phases meeting at the tetracritical point. It is considered that these multiple phases are ascribed to the internal degrees of freedom of the triplet Cooper pair and its degeneracy is removed for some reason in UPt_3.

So far, what removes the degeneracy, the symmetry breaking field (SBF), has been thought to be due to weak antiferromagnetic ordering (AF), which is observed by the neutron scattering experiments at around 5K [58, 59]. Under high pressures of 3kbar, it looks like that the multiple superconducting phases degenerate along with AF vanishes [60, 61]. However, no other measurement detects AF, so the existence of AF is still controversial.

Furthermore, above the pressures where AF vanishes, M.Boukhny *et al.* carried out ultrasonic velocity measurements under the uniaxial stress and claimed that there still exist two distinct superconducting phases on the zero field plane in spite of the lack of SBF [62]. On the other hand, M.Sieck *et al.* pointed out that their heat capacity experiments under the hydrostatic pressures up to 7kbar show no succesive transition [64].

Although recent experimental and theoretical works have revealed the nature which is more dynamically coupled to the superconducting order parameter, such discrepancies are unresolved yet. Therefore, establishing the multiple phase diagram of UPt_3 is to be carried out with well characterized samples and under well qualified pressure conditions.

Chapter 2

Experimentals

In this chapter, the outline of the heat capacity measurement under multiple extreme conditions is described. For further details, see descriptions in each Part.

2.1 Heat capacity measurements

2.1.1 Principles of heat capacity measurements

In Fig. 2.1, a specimen A is connected to the external system B by the thermal link, where $C(C_0)$ is the heat capacity and $T(T_0)$ is the temperature of A(B). In case that C_0 is much larger than C, the external system may be regarded as a thermal bath. And then the temperature of the specimen obeys an exponential decay, like;

$$T - T_0 = \text{const.} \exp\left(-\frac{t - t_0}{RC}\right) . \tag{2.1}$$

If R is known, or it can be measured, the heat capacity is measurable with the temperature declination with time t. This technique is well-known as the relaxation method. However, generally, the thermal impedance R is unknown, and it depends on the temperature. Moreover, in case the multiple pathes of the heat flow exist, the thermal relaxation process is getting more complicated. It is also noteworthy that the thermal relaxation inside a specimen must be achieved in a short time duration because it overrides the relaxation curvature to the thermal bath. For the reasones mentioned above, the advantage of this method is limited to the case of very small C.

On these experiments in this thesis, we employed the adiabatic method. This method is performed under the high-R configuration, i.e. the time constant of the relaxation to the thermal bath is infinitely long. In such a case, the system may be treated as a quasi adiabatic system. If the whole energy supplied by a heat pulse (ΔQ) is spent to raise the temperature of the system, the sample temperature should shift by a certain value ΔT, giving by the following relation;

$$C = \frac{\delta Q}{dT} \simeq \frac{\Delta Q}{\Delta T} . \tag{2.2}$$

This is the principle of the heat capacity measurement by the adiabatic method.

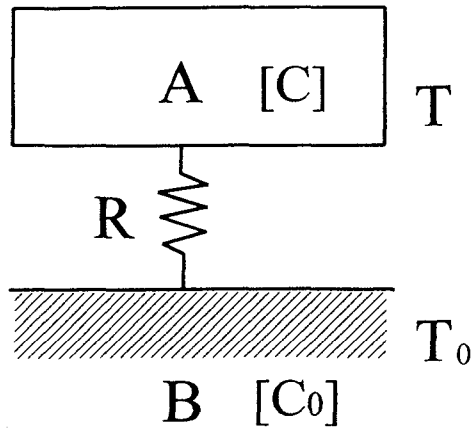

Figure 2.1: Simple model of the thermal relaxation. (see text)

2.1.2 Measurement procedure

Fig. 2.2 shows block diagram of a measuring system. The procedure is as following;

A heat pulse is supplied by the Joule heating of the heater H_{main}. The total amount of heat in one pulse is calculated as;

$$\begin{aligned} \Delta Q &= I_M V_M \Delta t \\ &= {I_M}^2 R_M \Delta t \,, \end{aligned} \tag{2.3}$$

where Δt is the width of a heat pulse, typically 10 seconds. The current I_M and the voltage V_M are both measurable parameters [1]. After a heat pulse, the temperature of the system rises suddenly and then gradually approaches to the thermal equilibrium.

In a real system, however, there are non-negligible heat leaks, for example, radiation, conduction through electrodes and so on. Assuming both a rather large thermal impedance and an almost temperature independent heat leak, eq. (2.1) is transformed, like;

$$\dot{T} = \frac{\dot{Q}}{C} \,, \tag{2.4}$$

where $\dot{Q}$ is the heat leak to the thermal bath. This gives the linear temperature drifts. Under low temperatures and quasi-adiabatic conditions, it is desirable to make $\dot{Q}$ negative so as to cancell the temperature drift by the aid of additional heater H_{sub}.

The manner of the thermal relaxation depends on the measuring configuration, as shown in Fig. 2.3. Temperature profiles just before and just after a heat pulse are fitted by linear dependence. The temperature difference ΔT is evaluated by extrapolation of temperatures from both sides at $t = \frac{t_1+t_2}{2}$. Thus the heat capacity of specimen is given by the definition of C (eq. 2.2). A typical measurement is done within a time interval of the order of 100 sec.

Of course, this C is the total heat capacity, or the heat capacities of sample addenda (heaters, Cu holders, a thermometer etc.) are included. The heat capacity of the sample is obtained by subtracting those "backgrounds", which are measured in a separate run.

[1] Needless to say, R_M is also measurable.

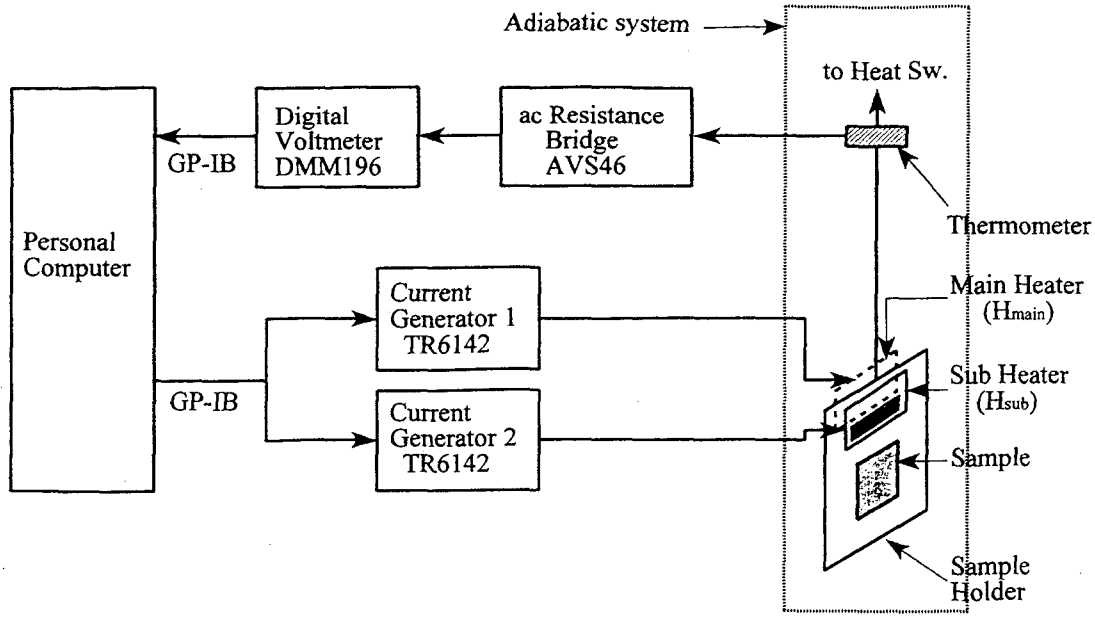

Figure 2.2: Block diagram of the heat capacity measurement system.

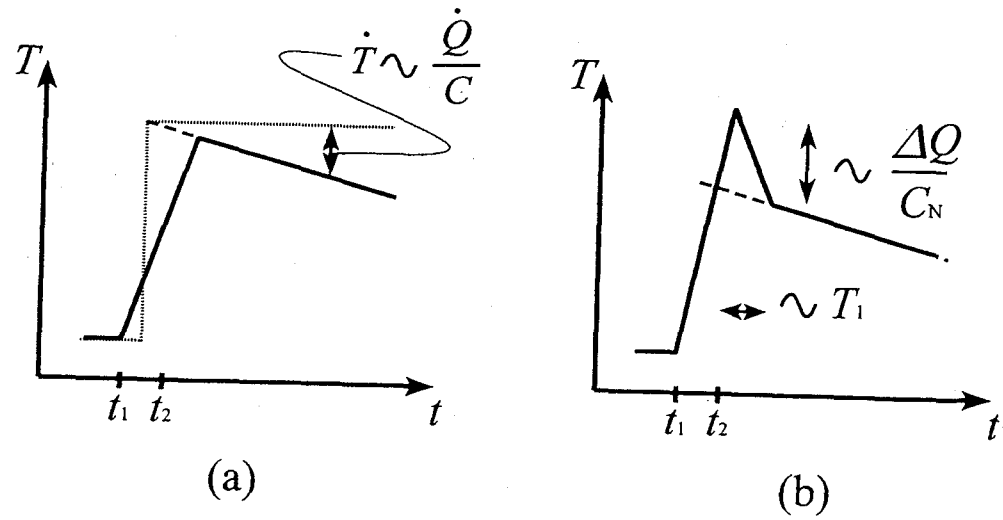

Figure 2.3: Examples of the temperaure profile in various configurations. The heat pulse is supplied between t_1 and t_2. (a) The broken line is the ideal case. In the real system, the heat leak to the thermal bath exists and the temperature profile shows a declination as $\dot{Q}/C$. (b) In case the nuclear magnetic heat capacity C_N is present, the temperature profile shows an overshoot and, after the duration of the nuclear spin lattice relaxation time T_1, the system settles down to the thermal equilibium.

In our laboratory, these procedures are automated by a computer controlled measurement system. Further details of the configuration of an automatic measurement system will be appeared in Appendix A.

2.2 Heat capacity measurement under very low temperature

2.2.1 Calibration of the thermometer

First of all, calibration of the thermometer is the most important for the measurement of heat capacity. The calorimetry is nothing but the thermometry.

In our laboratory, the temperature calibration below 1K is performed by the measurement of the susceptibility of $2Ce(NO_3)_3{\cdot}3Mg(NO_3)_2{\cdot}24H_2O$ (CMN) paramagnetic salt, which is calibrated with NBS #768 fixed points. Additionaly, the resistance at fixed points are measured for evaluation of calibration.

Above 1K, calibrated Ge thermometer is used. If necessary, NBS #767 fixed points or ^{4}He vapor pressure temperature scale are also available.

2.2.2 Heat switch

In general, the heat switch is the most principal part of the adiabatic method. Especially, at the temperature range of the dilution refrigerator, its importance increases. In the present study, a mechanical heat switch is employed, which is in common use at low temperatures. It is easy to handle the switch and has high reliability, while its vibration accompanying the switching on/off causes the heat up of the adiabatic system. Of course, the heat up depends on the heat capacity of the system. However, sometimes it reaches up to 100mK which becomes lower limit of the reached temperatures of the measurement.

The superconducting heat switch has also been used widely. Since finite R remains even after turning off the switch, it is useful technique to measure the sample with rather large heat capacity at very low temperatures. Trial use of a $5{\times}2{\times}0.1mm^3$ In (99.99%) foil is found to work well against a pressure cell made of Be-Cu with heat capacity of $C/T \sim 10^{-4}J/K^2$. In order to operate the switch, a superconducting solenoid with the coil constant of 1.04 gauss/mA is used. The sweep rate is 0.5mA/sec and it takes about 10 minutes to turn the switch on/off.

2.2.3 Heater

It is desirable that the resistance of the sample heater is temperature independent. In our laboratory, a plate type metal film resistor is employed as the heater, which has compact shape and hardly depends on both the temperature and the magnetic field.

The manganin wire is commonly used, too. However, it is noted that it shows a temperature dependence below 1K, changing nearly by a few percent.

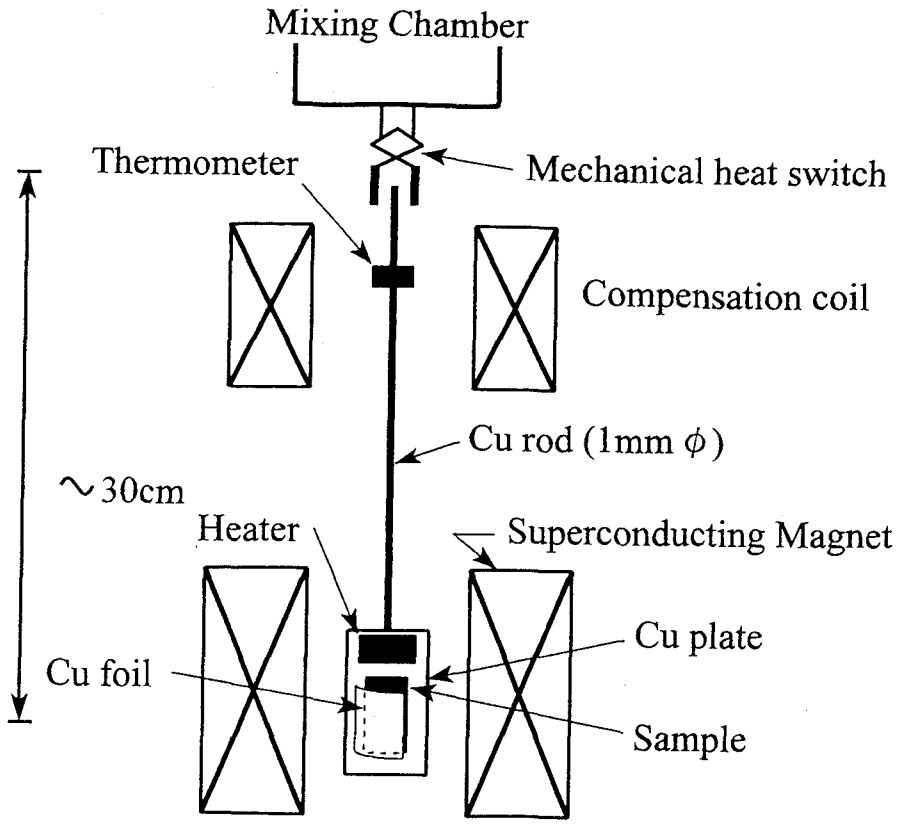

Figure 2.4: Schematic drawing of the heat capacity measurement system under high magnetic fields up to 14T.

2.3 Heat capacity measurement under high magnetic field

The most bothering problem under high magnetic field is field dependence of the resistance thermometer. In order to avoid it, a superconducting magnet with a field compensation coil is used. The thermometer (mostly Ge or carbon resistor) is placed in the field compensated area and connected to the center of the magnetic field with a Cu thermal link (1mmϕ and about 30cm length), as shown in Fig. 2.4

Without the field compensation coil, a RuO_2 thermometer is employed and placed in the same way described above. The thermometer is less dependent to the magentic field and its sensitivity is $\frac{dR}{dT} \sim$–4.6kΩ/K at 0.1K, which is comparable with that of Ge thermometer, $\frac{dR}{dT} \sim$–10kΩ/K.

It should be noted that the thermal impedance between the thermometer and the sample holder is small enough for measurements. It can be confirmed by the heat pulse. Actually, the temperature starts to increase within about one second after the heat pulse has turned on.

In addition, heat capacity of nuclear spin system appears at lower temperatures. The nucleus of Cu which is generally used as the sample addenda has nuclear spin moment. Thus, it exhibits Schottky-type anomaly due to the Zeeman splitting under external fields.

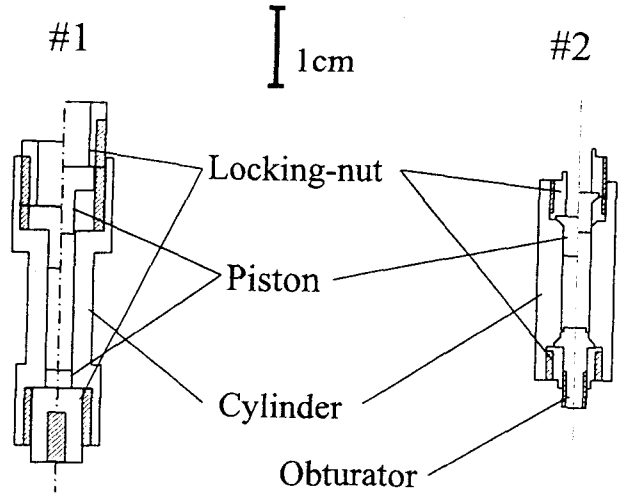

Figure 2.5: Schematic drawings of the piston-cylinder type self-clamping pressure cell.

For example, nuclear heat capacity reaches up to almost 50 times larger than the electronic specific heat of Cu, at temperature of 0.1K and under magnetic field of 10T. Since nuclear portion causes a reduction of measuring sensitivity, it is preferable that Au should be used, which shows no nuclear spin contribution and relatively small magnetoresistance.

2.4 Heat capacity measurement under high pressure

2.4.1 Pressure cell

In the experiments under pressures, a conventional piston-cylinder type pressure cell is used, which is shown in Fig. 2.5. In order to perform the sensitive measurement, the pressure cell should be made as small as possible because its contribution to heat capacity is nearly equal to the background.

The pressure cell is made of Be-Cu alloy. The total weight is 22g (#1) and it presents the heat capacity of $C/T = 4 \times 10^{-4}(\mathrm{J/K^2})$ below 1K, which is somewhat larger than that of pure Cu. The total weight has been reduced down to 14g in case of the pressure cell #2.

2.4.2 Applying the pressure

The mixture of Fluorinert FC70:FC77 (1:1) is used as the pressure transmitting medium in order to obtain hydrostatic pressures. The melting points are 248K for FC70 and 163K for FC77 respectively. The volume of the pressure medium reduces at low temperatures and it causes the pressure decreasing. Generally, it decreases about 3kbar lower than that clamped at room temperature.

In the present study, two methods of the pressure sealing are employed [4]. The former is shown in Fig. 2.6-(a). Pressure is simply sealed with Teflon disks which are made slightly larger than i.d. of the cylinder. Anti-extrusion rings of Cu or cupro-nickel with soldered

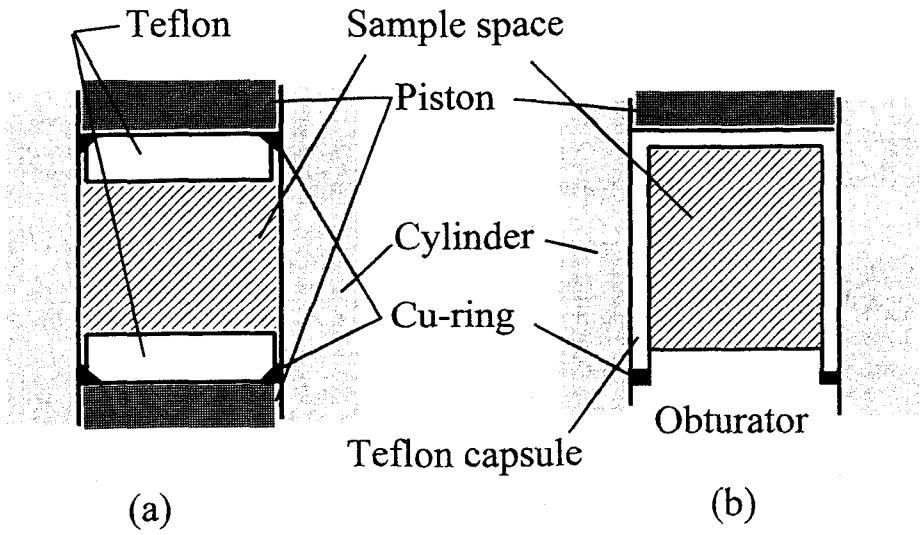

Figure 2.6: Schematic drawings of the pressure sealing. (see text)

surfaces are added to prevent leakage out of Teflon disks. This method highly depends on performance of the disk.

The latter is rather similar to the conventional Teflon capsule method, as shown in Fig. 2.6-(b). The lower side of the piston is processed for the Teflon capsule to be fixed directly, what is so called the obturator, and an anti-extrusion ring is also added. The capsule is carefully lathed under a microscope and its edge is especially sharpened by a cutter. The whole part should be prepressed with rather viscous pressure medium before the experiment [2]. GE7031 varnish may help the initial application of the pressure.

2.4.3 Heat capacity measurement under high pressures

The measurement scheme is the same as that described in the former section, except the heater. As the heater, manganin wires are directly wound on the pressure cell by means of bifilar way.

At low temperatures, the pressure medium shows poor thermal conductivity. In order to obtain a good thermal contact between a sample and the pressure cell, Ag powder is packed in the sample space. It also has the aim to cancell the pressure decrement at low temperatures. In typical case, for example, the weight of Ag powder is 33mg and the packing factor is about 7.5%. Without Ag powder, the relaxation time constant reaches up to 240 sec, while it is shortened down to about 60 sec.

2.4.4 Pressure calibration

Pressure at low temperatures is calibrated by the superconducting transition point T_c of Sn, which is detected by means of ac susceptibility measurement. The pressure dependence

[2]The mixture of Fluorinert can be used.

of T_c of Sn is linear within the range of pressure reached by the piston-cylinder cell and given by the following empirical formula;

$$T_c(\mathrm{K}) = 3.722 - 0.0447 \times P(\mathrm{kbar}). \tag{2.5}$$

The pick-up coil (14mmϕ, 33mm length) is located outside of the cell, consisting an astatic pair of coil and each coil is about 1000 turns. It is able to detect the transition of Sn (99.99%) of a 20 mg tip loaded in the pressure cell.

Part II

Haldane-gap Antiferromagnet NDMAZ

Chapter 3

Introduction

The nature of the low dimensionality lies under its instability. This is realized when quantum effects of the spin chain system , for example, Haldane gap and spin Pierls transition are taken into consideration.

3.1 Magnetism of low dimensional system

One dimensional Heisenberg antiferromagnet (1D-HAF) is expressed by the following simple spin Hamiltonian;

$$\mathcal{H} = -J \sum_i \boldsymbol{S}_i \cdot \boldsymbol{S}_{i+1} \,, \tag{3.1}$$

where J is the intrachain coupling constant and $J < 0$ for antiferromagnet.

The eigen states of eq.(3.1) were given by the Bethe *ansatz* in case of S=1/2 [5]. L.Hulthén used them to obtain the exact values for the ground state energy of an S=1/2 linear chain Heisenberg antiferromagnet [6]. C.N.Yang and C.P.Yang proved exactly the Bethe *ansatz* for the ground state of a finite chain [7]. Magnetization at zero temperature was calculated by R.B.Griffiths [8].

J.C.Bonner and M.E.Fisher carried out the numerical calculations for several number of spins up to N=11 and estimated the thermal and magnetic properties of an infinite chain by extrapolation [9]. They showed that the energy level of the spin chain system is gapless and no long range ordering occures down to T=0K.

The low-lying excited states are explained by the spin wave theories proposed by P.W.Anderson [10] and by R.Kubo [11] in 1952, and later exactly calculated for an S=1/2 infinite chain by J.des Cloizeaux and J.J.Pearson [12], which give the relation $\varepsilon(\boldsymbol{k}) = \pi |J| |\sin \boldsymbol{k}|$.

In spite of these tremendous number of work, the study for $S > 1/2$ was merely carried out because of difficulties of the calculation and it was believed that the physical properties are independent with respect to the spin quantum number until Haldane's conjecture comes out.

Some of magnetic compounds containing ions of *3d* transition metal, which have a low dimensional path of the exchange interaction, have been extensively studied since 1960's so as to examine experimentaly the theories described above. Here we show some results of "real" one dimensional magnets in Figs. 3.1, 3.2, 3.3 and 3.4.

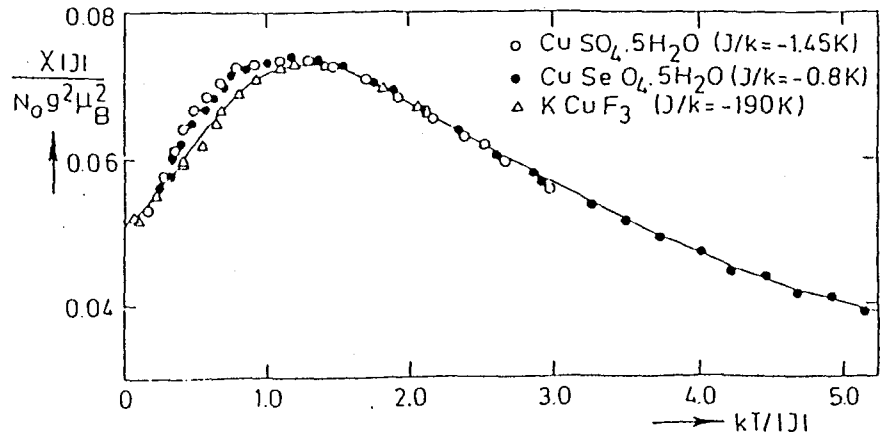

Figure 3.1: Examples of susceptibilities of 1D-HAF(S=1/2) [13]. The solid line is the theoretical result [9]. Susceptibility shows a broad maximum due to short-range ordering around $T = J/k_B$.

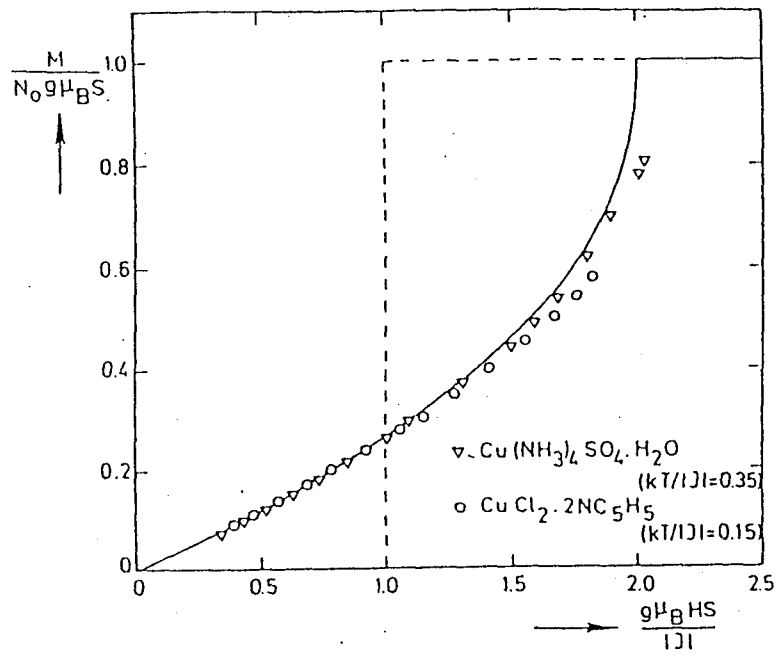

Figure 3.2: Examples of magnetizaions of 1D-HAF(S=1/2) [14]. The solid line is the theoretical result [8]. Magnetization curve shows a steep increment due to the spin fluctuation just below the saturation field.

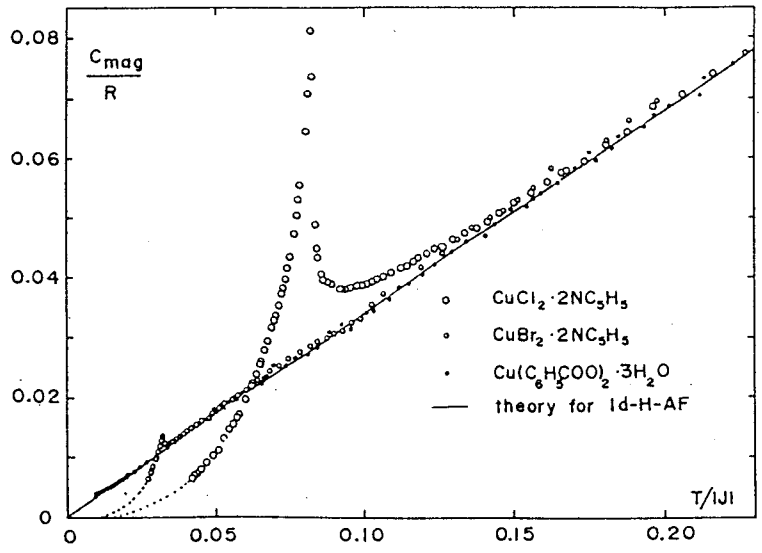

Figure 3.3: Examples of heat capacity of 1D-HAF(S=1/2) [15]. Heat capacity at low temperatures shows T-linear dependence expected by the spin wave theory and a sharp peak due to 3D-LRO.

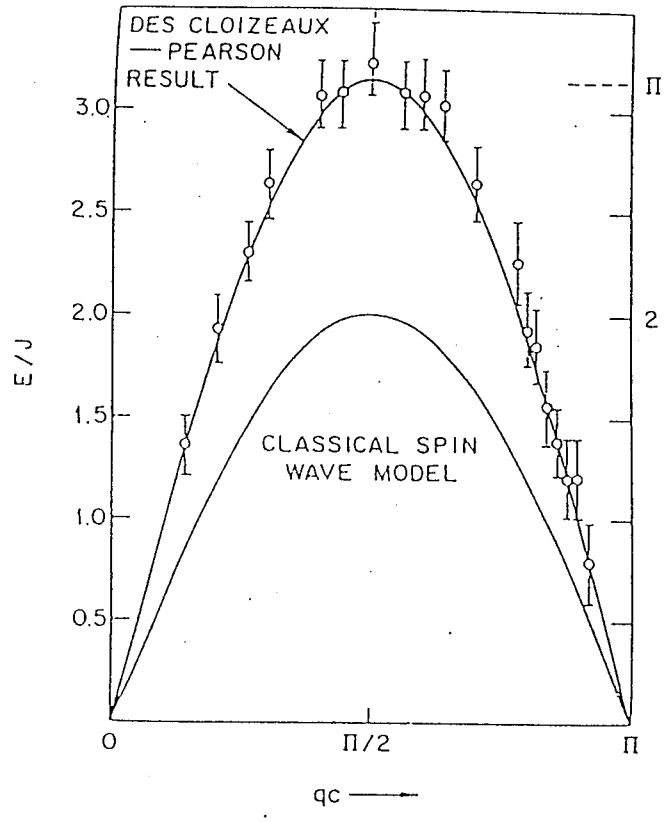

Figure 3.4: Spin wave dispersion curve of 1D-HAF(S=1/2), $CuCl_2 \cdot 2N(C_5D_5)$ [16]. Energy is scaled in units of J/k_B=13.4K. The solid lines represent the thoretical spin wave dispersion curves [12].

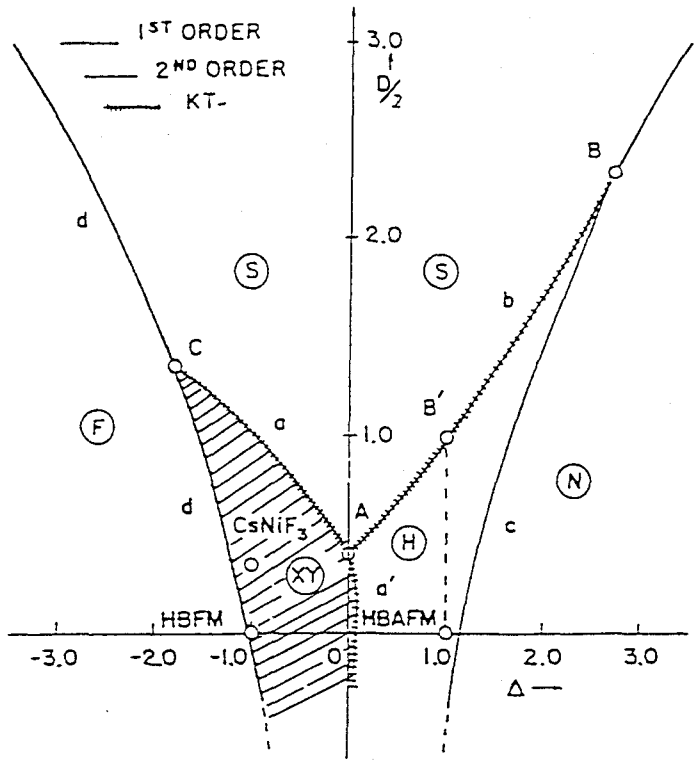

Figure 3.5: Phase daiagram obtained with the Hamiltonian; $\mathcal{H} = \sum\{-2J(S_i^x S_{i+1}^x + S_i^y S_{i+1}^y + \Delta S_i^z S_{i+1}^z) + DS_i^{z2}\}$, where S_i^x is the x-component of spin operator of the i-th site, Δ is the spin dimensionality parameter and D is the single ion anisotropy. The notations of phase diagram are as follows; H: Haldane phase, S: disordered phase with the singlet ground state and the large single ion anisotropy, N: Néel ordered phase, XY: gapless XY phase, F: Ferromagnetic ordered phase. [20]

The most important thing is that these real system show three dimensional long range ordering (3D-LRO) at low temperatures, as shown in Fig. 3.3, due to the existence of exchange interaction between chains J'. Temperature T_N which 3D-LRO occurs is estimated by the molecular field approximation, giving;

$$k_B T_N \simeq 2S^2 \sqrt{JJ'} \ . \tag{3.2}$$

3.2 Haldane gap system

3.2.1 Verification of the Haldane gap

In 1983, F.D.M.Haldane predicted [1] the existence of energy gap between the ground state and the first excited state and the exponentially decaying correlation functions in case of an integer spin chain, while a half integer spin chain has no energy gap and the correlation function with power law decay, as mentioned above. Since then, great number of theoretical and experimental studies have been carried out to verify Haldane's conjecture.

Most of the theoretical works have accepted the Haldane's conjecture. Some calculations

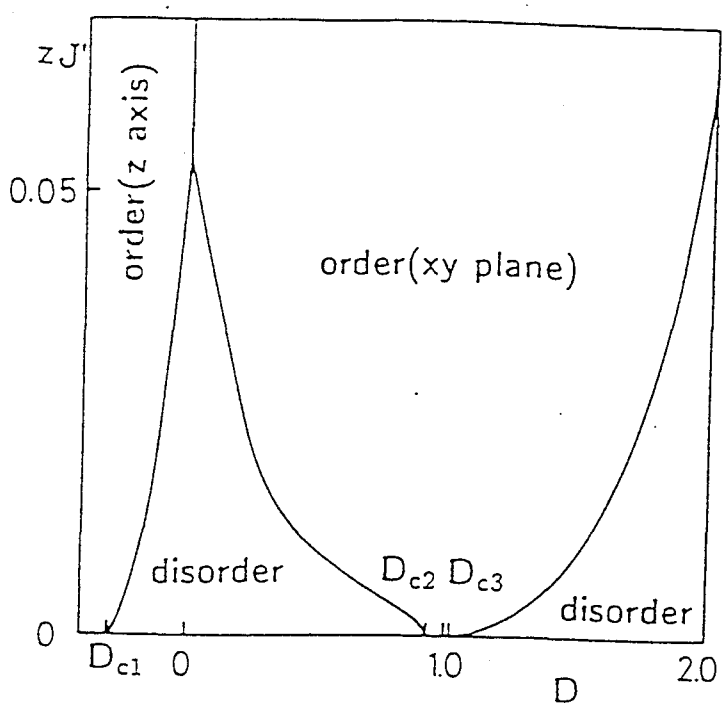

Figure 3.6: Phase diagram obtained with the Hamiltonian; $\mathcal{H} = \sum \mathrm{S}_i\mathrm{S}_{i+1} + D\sum S_i^{z2} + J'\sum \mathrm{S}_i\mathrm{S}_j$, where D is the single ion anisotropy and J' is the interchain exchange coupling constant.

give the value of the energy gap, $E_g \sim 0.41|J|$ [17, 18]. Also the applications to the real system, i.e. effects of the single ion anisotropy and the interchain interaction have been studied [19, 20, 21], resulting the existence of the Haldane gap as shown in Figs. 3.5 and 3.6.

Simultaneously, many magnetic compounds which show gap-like behavior at low temperatures have been found. Some of them are summarized in Table 3.1. Most of all, NENP ($Ni(C_2H_8N_2)_2NO_2ClO_4$) has been investigated by various techniques as a typical Haldane gap antiferromagnet. Experimental aspects of NENP is presented in the following section.

3.3 Haldane gap antiferromagnet NENP

The crystal structure of NENP is shown in Fig. 3.7. The Ni^{2+} ions are bridged by nitcrite groups bounded on one side be the nitrogen atom and the other side by one of the oxygen atoms.

The magnetic susceptibility shows a broad maximum at about 60K, as shown in Fig. 3.8

[1] $Ni(C_2H_8N_2)_2NO_2ClO_4$
[2] $Ni(C_3H_{10}N_2)_2NO_2ClO_4$
[3] $Ni(C_3H_{10}N_2)_2N_3ClO_4$
[4] $Ni(C_5H_{14}N_2)_2N_3ClO_4$
[5] $(CH_3)_4NNi(NO_2)_3$
[6] MIz=2-methylimidazole
[7] DMIz=1,2-dimethylimidazole

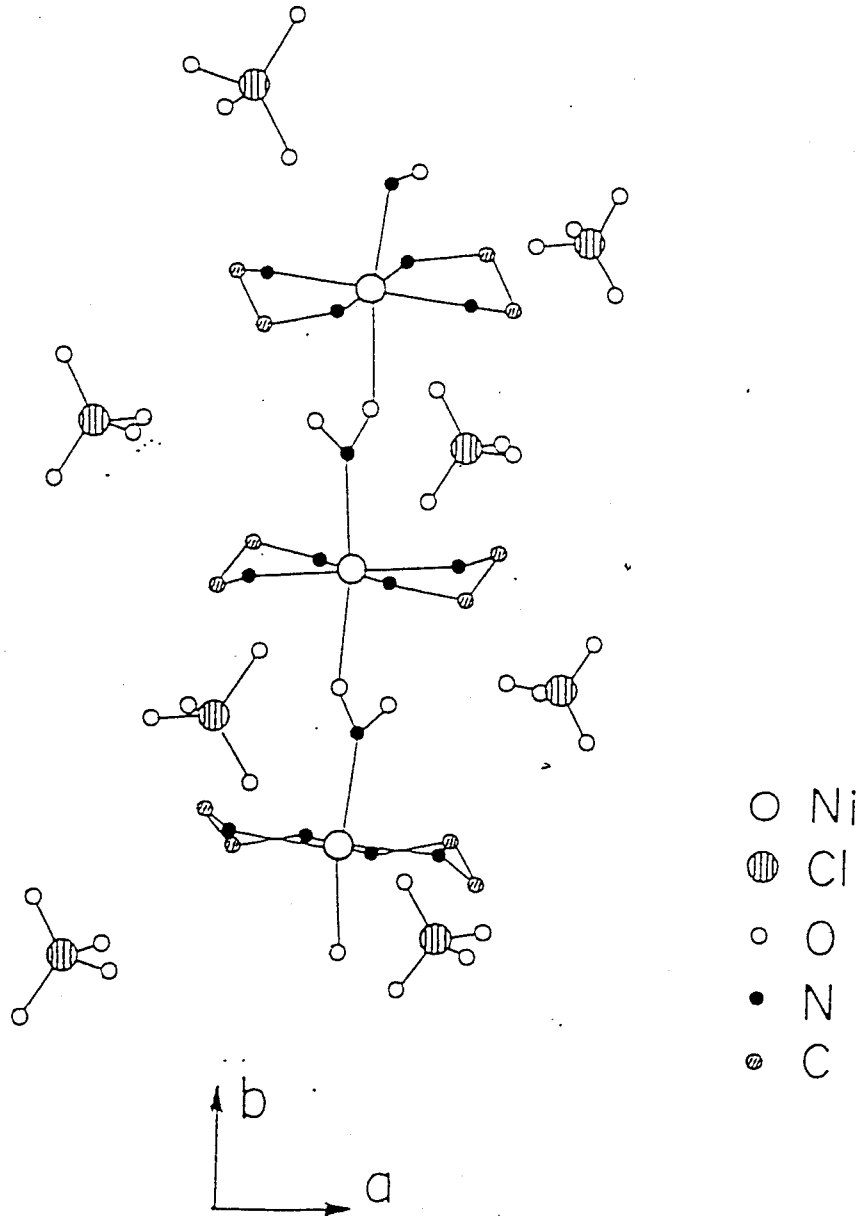

Figure 3.7: Crystal structure of NENP.

	J/k_B (K)	$\lvert J/J' \rvert$	D/k_B (K)	E_g/k_B (K)	Ref.
NENP[1]	−55	4×10^{-4}	−12	19	see §3.3
NINO[2]	−50	–	$\sim$ −14	13	[24, 30]
NINAZ[3]	$\sim$−120	–	–	$\sim$ 40	[32]
NDMAZ[4]	−70.6	–	–	21.6	see §3.5
TMNIN[5]	−12	–	$\sim$ 0.03	5	[33, 34]
$AgVP_2S_6$	−400	$\sim 10^{-5}$	–	320	[37]
$NiC_2O_4 \cdot 2MIz$[6]	−39.7	–	–	20.3	[38]
$NiC_2O_4 \cdot 2DMIz$[7]	−42.9	–	–	19	[38]
Y_2BaNiO_5	−285	–	–	100	[39]

Table 3.1: Magnetic parameters of Haldane gap antiferromagnets.

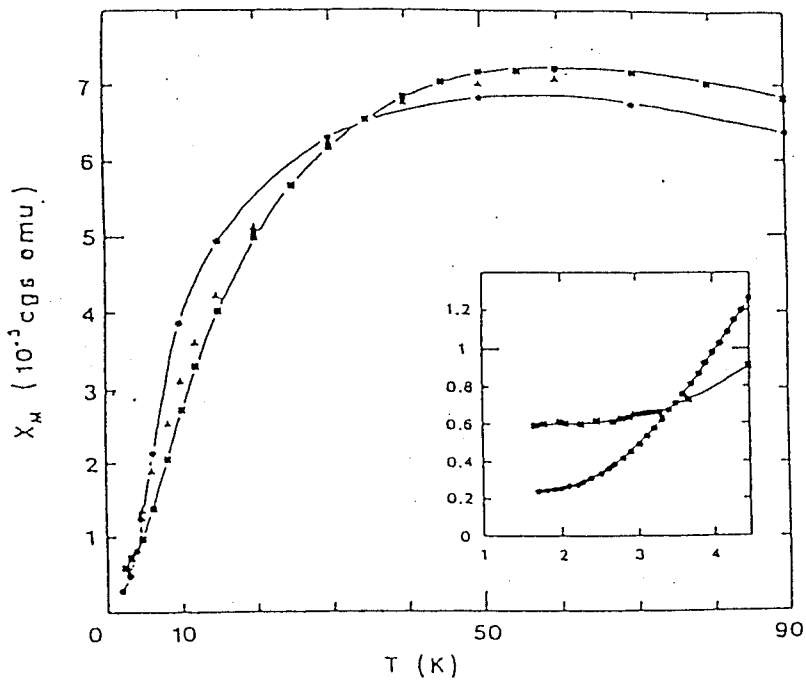

Figure 3.8: Magnetic susceptibility of NENP along with three crystal axes; solid square is a axis, solid circle is b axis and solid triangle is c axis, respectively. The lines are guides to the eye. [23]

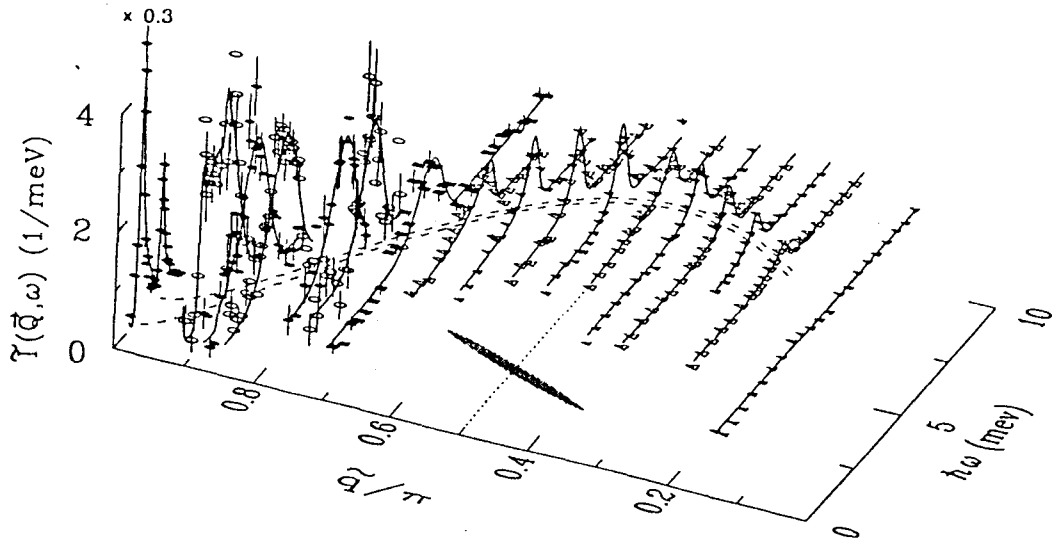

Figure 3.9: Normalized magnetic scattering intensity from NENP. Solid lines: Calculated intensity profiles for infinite-lifetime excitations based on the dispersion relation shown with a dashed line; $\omega_{\perp,\parallel}(\tilde{q}) = \{\Delta^2_{\perp,\parallel} + v^2 \sin^2 \tilde{q} + A_{\perp,\parallel} \cos^2(\tilde{q}/2)\}^{1/2}$. Circles, squares and triangles represent the measuring configuration. The ellipsoid is FWMH of the resolution for $\tilde{q}$=0.5π. [25]

[23], which is characteristic of 1D-HAF. As the temperature decreases further, however, it abruptly decreases. This behavior (T <5K) is ascribed to the existence of the Haldane gap, giving by the following relation;

$$\chi(T) = \chi(0) + C \exp\left(-\frac{E_g}{k_B T}\right) , \tag{3.3}$$

with E_g/k_B=11K and 17K for respective field directions parallel and perpendicular to the chain axis. In the high temperature region, the data are fitted by the theoretical curve with J/k_B=-47.5K and D ~12K [22]. Particularly, the susceptibility curves reveal no transition to 3D-LRO within the temperature range down to T=1.5K, which imply that the electron spin falls down to the non-magnetic ground state.

The direct observation of the Haldane gap is obtained by the inelastic neutron scattering measurement [23, 25]. As shown in Fig. 3.9, the dispersion curves show the energy gap at the zone boundary.

K.Katsumata *et al.* have performed the high field magnetization measurements and obtained a clear evidence for the existence of the Haldane gap. [26] The magnetization is very small in the low field region and begins to increase sharply at finite fields $H_c^{\parallel}$=8T and $H_c^{\perp}$=12T for the parallel and perpendicular directions with respect to the chain axis, as shown in Fig. 3.10. This result has been interpreted as the existence of the Haldane gap and the negative sign for the single ion anisotropy D' in the excited state. For the external field H applied along b-axis, the energy of one of the excited triplet (S_z=−1) decrease as;

$$E = E_g - \frac{|D'|}{3} - g_{\parallel}\mu_B H , \tag{3.4}$$

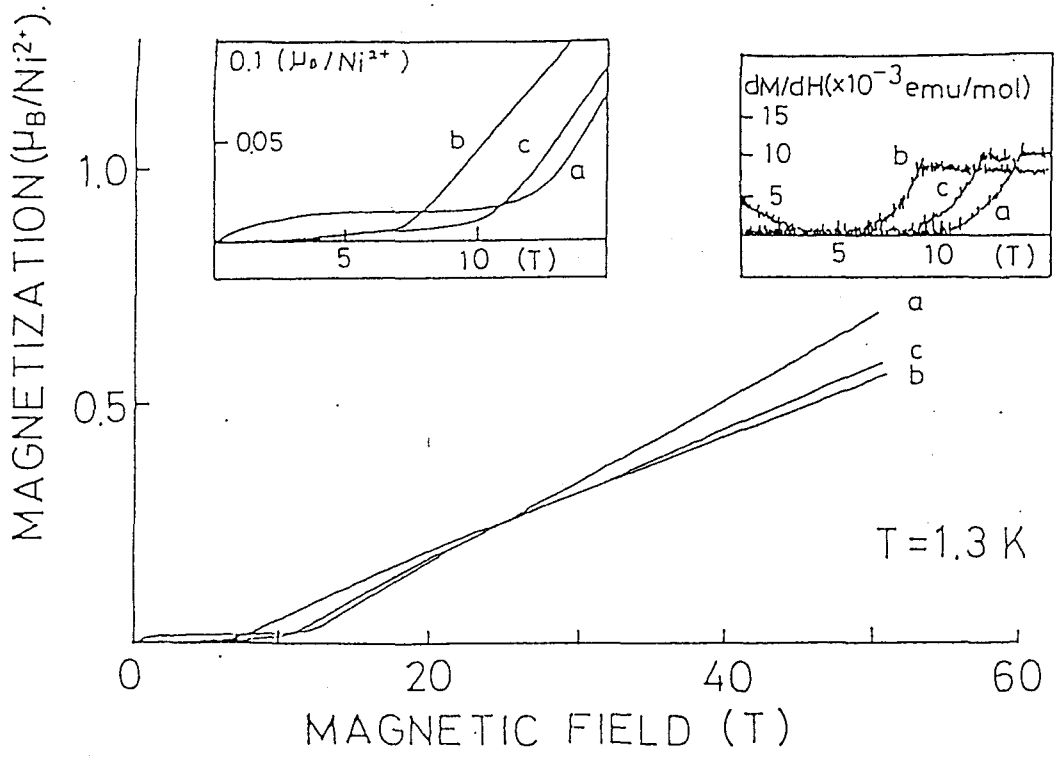

Figure 3.10: Magnetization curves of NENP along three crystal axes at 1.3K. Left panel: Low field part of the magnetization curves. Right panel: Derivative of the magnetization with respect to H, dM/dH vs. H curves obtained in the pulsed-field experiment. [26]

where $E_g - \frac{|D'|}{3}$ is the Haldane gap energy in zero external field and $g_{\parallel}$ is the g-value along the chain axis. When H is directed perpendicular to the chain axis, the effective energy is expressed as;

$$E = E_g + \frac{|D'|}{6} - \frac{1}{2}\left(D'^2 + 4{g_\perp}^2{\mu_B}^2H^2\right)^{\frac{1}{2}} , \tag{3.5}$$

where $g_\perp$ is the g-value perpendicular to the chain axis. Putting the experimental values for $H_c^{\parallel}$=8T, $H_c^{\perp}$=12T, $g_{\parallel}$=2.15 and $g_\perp$=2.22 into eqs. (3.4) and (3.5), the values E_g=17K and D'=−16K are obtained.

The qualitatively same results have been also given by Y.Ajiro *et al.* [27]

3.4 Searching 3D-LRO under high magnetic fields

If the energy gap exists, 3D-LRO does not occur down to T=0K even though the inter-chain interaction exists. However, the high field magnetizaion measurements revealed that the Haldane gap may vanish at above H_c and then the system becomes magnetic again. Under such conditions, 3D-LRO may occur. In order to realize 3D-LRO, the heat capacity measurements of the Haldane gap antiferromagnet under high magnetic fields have carried out.

3.4.1 NENP

The heat capacity of NENP is shown in Fig. 3.11. Under zero magnetic field, it exhibits an exponential decrement at lower temperatures. Approaching to H_c, the temperature dependence of heat capactiy comes to resemble a *gapless-like* behavior, expressed by the following relation;

$$C = \gamma T + \beta T^3 . \tag{3.6}$$

The T linear term is ascribed to the magnetic excitation and T cube term is the contribution from the lattice. Applying the external field above H_c, however, a broad anomaly appears and its peak moves to higher temperature for higher magnetic field. No sharp peak due to 3D-LRO has been observed. By analyzing the data with Schottky type anomaly of the simple two levels, which is given by;

$$C_m \sim \left(\frac{\Delta}{k_BT}\right)^2 \exp\left(-\frac{\Delta}{k_BT}\right) , \tag{3.7}$$

it is found that the energy gap still exists at H_c and opens again with increasing field, as shown in Fig. 3.12, though our results well reproduce the anisotropic behavior observed in the high field magnetization measurement. The absence of 3D-LRO at and above H_c may be caused by the remaining energy gap.

T.Sakai and H.Shiba [28] explained this characteristic field dependence of the gap on NENP by the existence of the transvers staggered field observed in ^{1}H-NMR measurements [29]. The staggered tilting of the principal axes of the g-tensor causes the staggered moment, as shown in Fig. 3.13. Then, our interest moves on the other Haldane gap antiferromagnet.

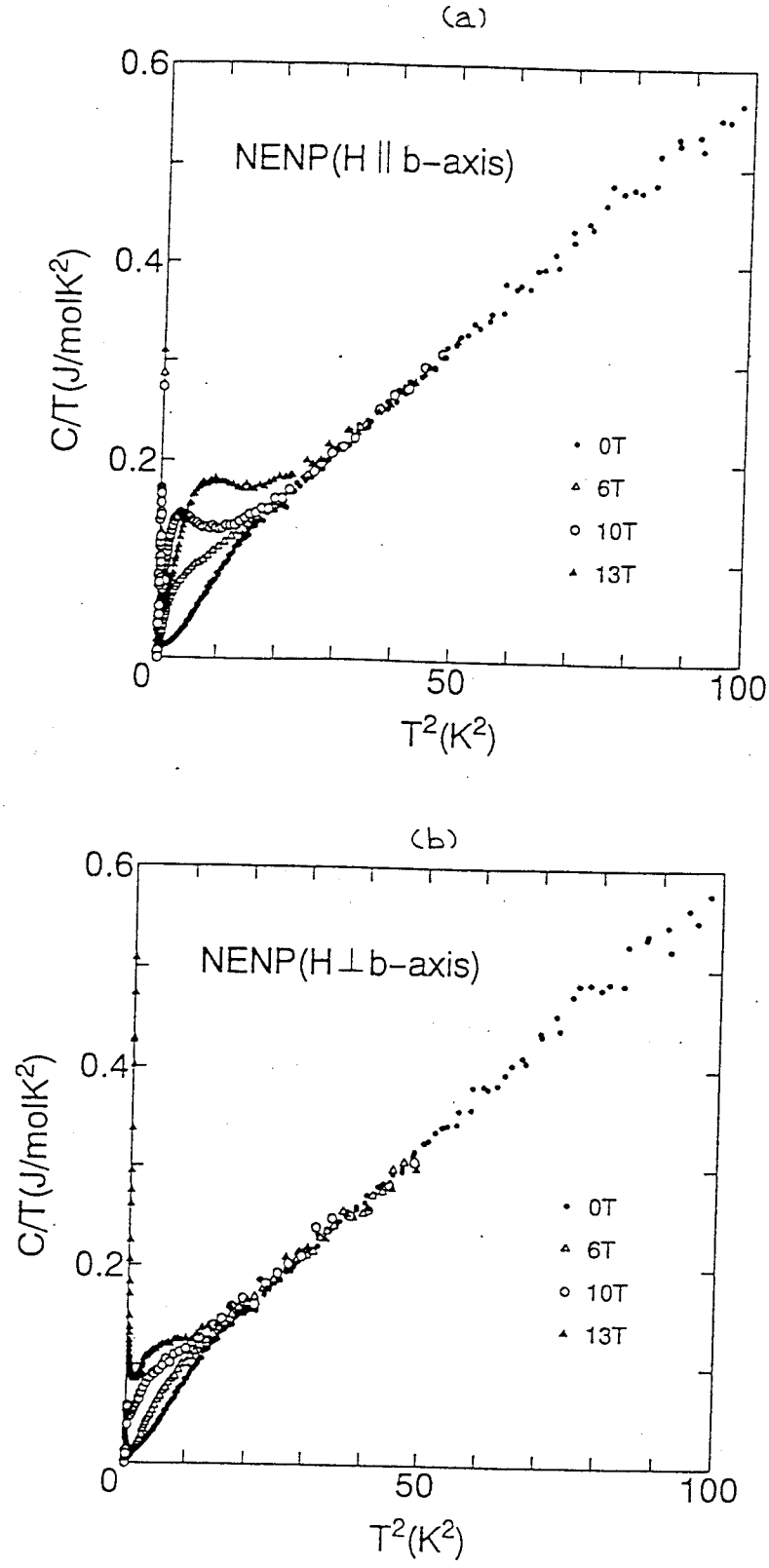

Figure 3.11: Heat capacities of a single crystal of NENP under magnetic fields by $C/T - T^2$ plot. Magnetic field up to 13T is applied parallel(a) and perpendicular(b) to the chain axis. [3]

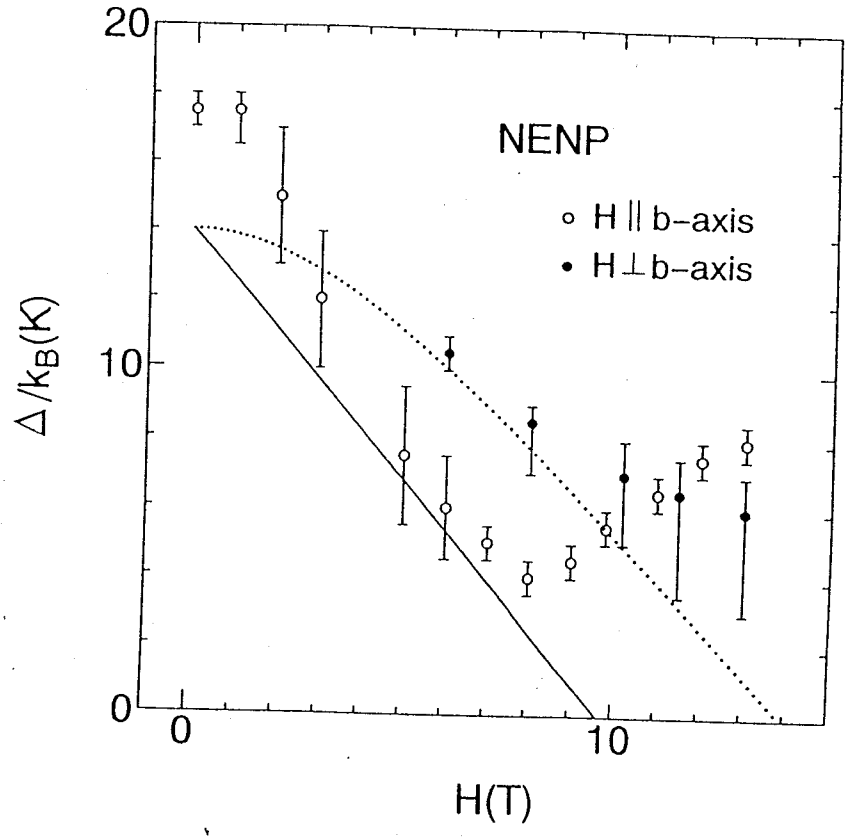

Figure 3.12: Field dependence of the energy gap Δ/k_B. The solid and broken lines are drawn by the fitting of eqs. (3.4) and (3.5), respectively.

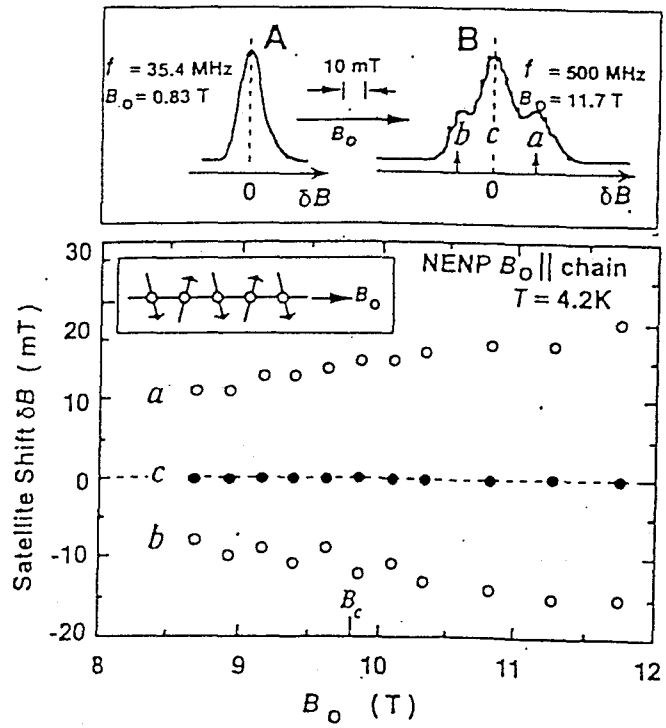

Figure 3.13: Field dependence of the satellite shift of the proton NMR from the main line across the critical field (B_c=9.8T). Solid circles show the main line and open circles show the satellite line. No singularity appears at B_c. [29]

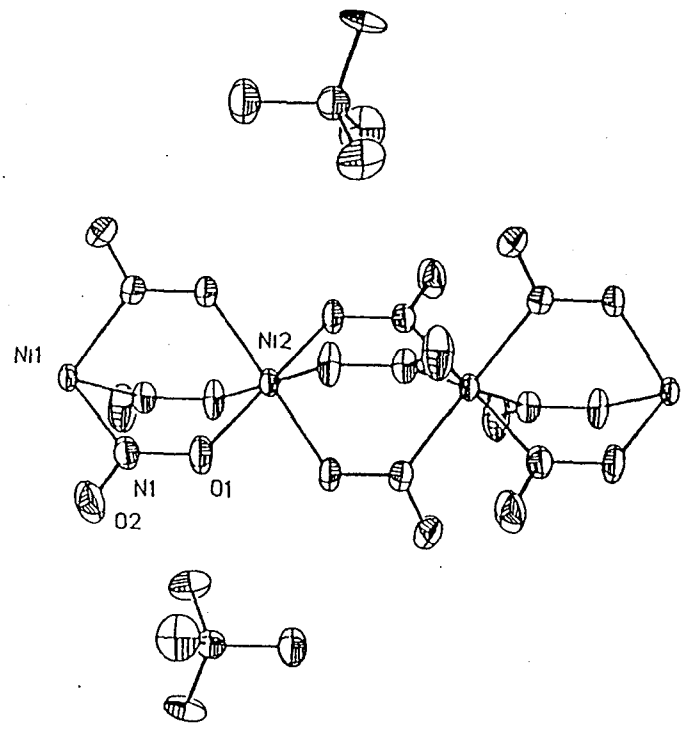

Figure 3.14: Crystal structure of TMNIN.

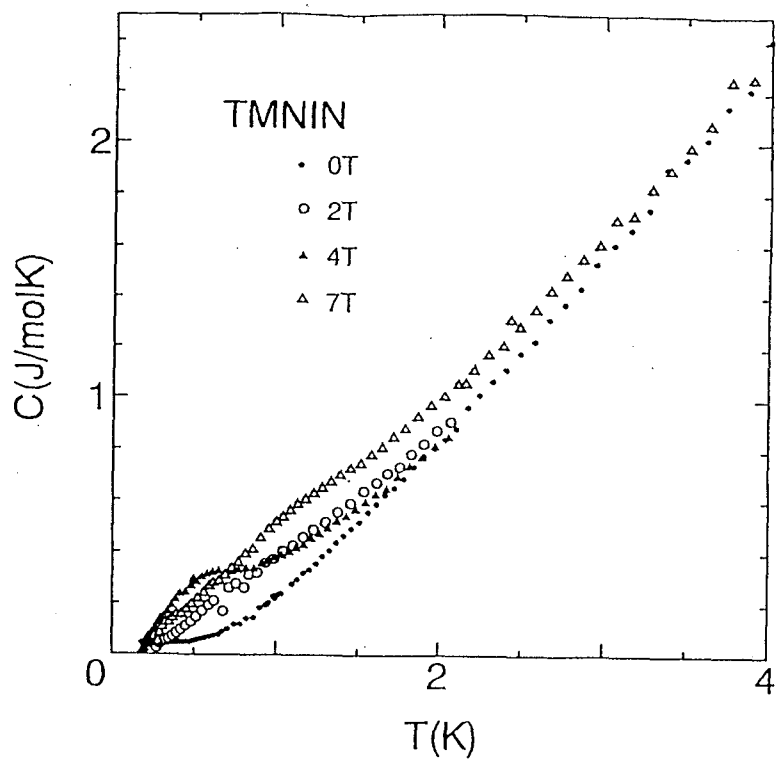

Figure 3.15: Heat capacities of polycrystalline sample of TMNIN under magnetic fields up to 7T. [36]

3.4.2 Other Haldane gap antiferromagnets

$(CH_3)_4NNi(NO_2)_3$ (TMNIN) is the most interesting candidate because of the crystallographically expected absence of the staggered tilting of Ni^{2+} sites, as shown in Fig. 3.14. Unfortunately, the single crystal of this compond has not been obtained yet, so the heat capacity of the polycrystalline sample of TMNIN was measured [36]. As seen in Figs. 3.15 and 3.16, the results are qualitatively the same as that of NENP. No 3D-LRO is observed with in our experimental range and the energy gap remains at and above H_c ~3T though the appearance of the staggered moment is not confirmed.

On the other hand, the structure of $Ni(C_3H_{10}N_2)_2NO_2ClO_4$ (NINO) is similar to that of NENP, as shown in Fig. 3.17. The staggered tilting of the principal axis of g-tensor is present as well and our preliminary result of ^{1}H-NMR measurement showed the appearance of the staggered field $0.8\mu_B$ at 4.2k and 10.3T [31]. The heat capacities of a single crystal of NINO under the fields up to 13T is shown in Fig. 3.18. The result is qualitatively the same as that of NENP, as shown in Fig. 3.19. The energy gap remains at and above H_c ~8T and no 3D-LRO is observed.

In summary, the relation between the appearance of the staggered moment and the remaining energy gap above H_c is still not clear. However, whenever the staggered moment is present, it causes the energy gap above H_c. Therefore, the investigation of other Haldane gap antiferromagnet which does not show the appearance of the staggered field is to be carried out in order to realize 3D-LRO under the high magnetic field.

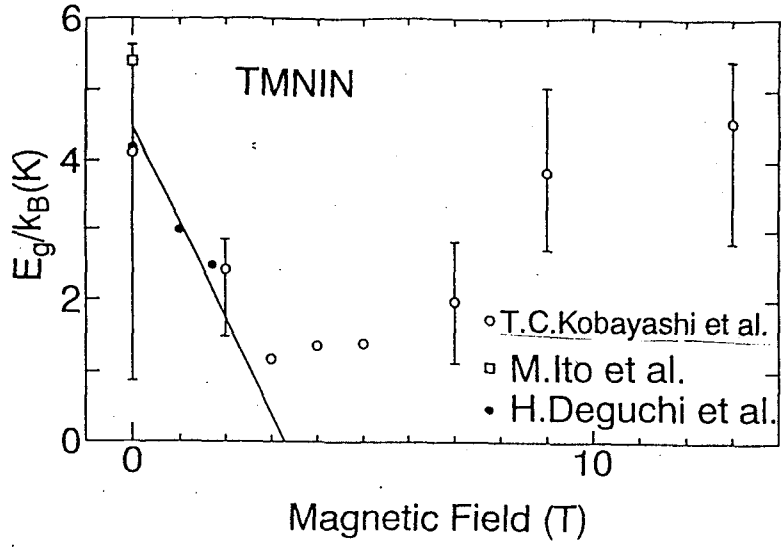

Figure 3.16: Field dependence of the energy gap E_g/k_B. The solid line is drawn by $E_g - g\mu_B H$ with the experimental values of the susceptibility measurement. [35, 36]

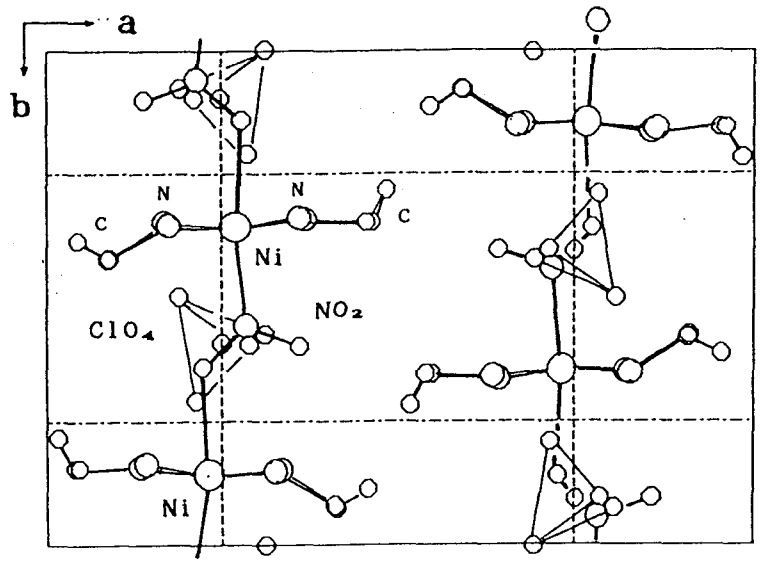

Figure 3.17: Crystal structure of NINO.

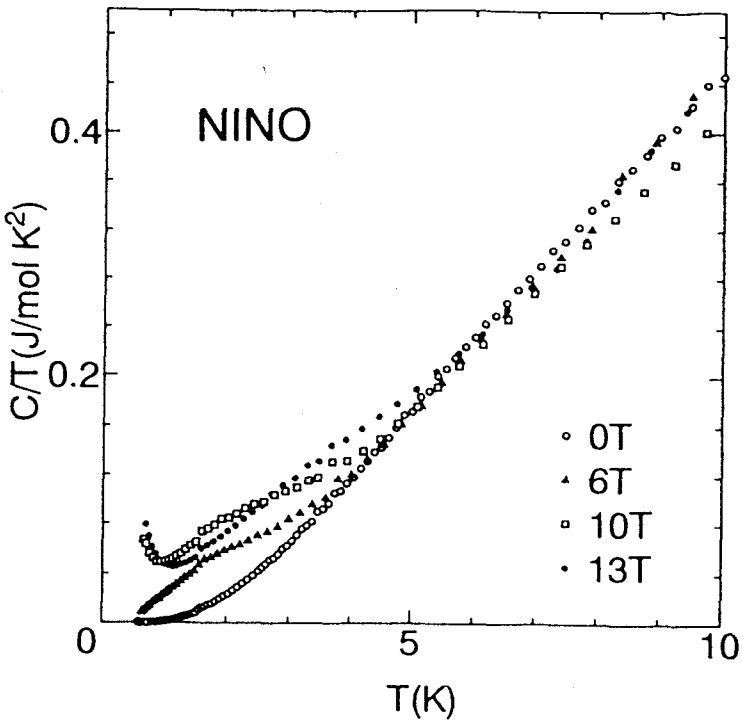

Figure 3.18: Heat capacities of a single crystal of NINO for the field applied parallel to the chain axis up to 13T. [31]

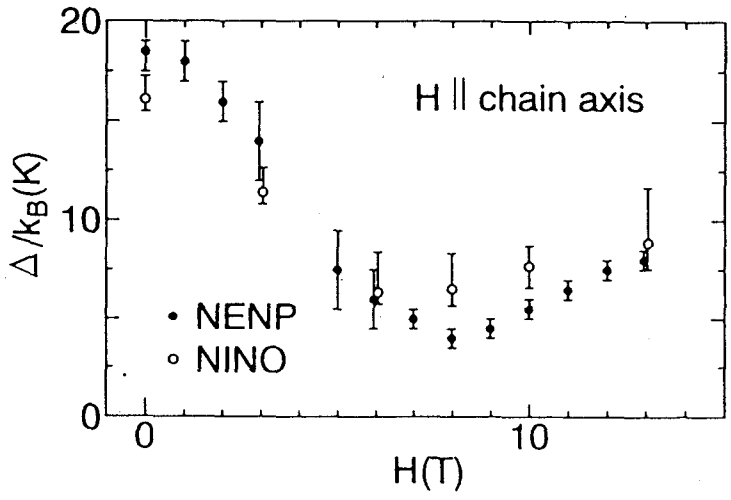

Figure 3.19: Field dependence of the energy gap of NENP and NINO. [31]

3.5 Haldane gap antiferromagnet NDMAZ

3.5.1 Crystal structure

The crystal structure of NDMAZ is monoclinic and the lattice constants are a=18.860Å, b=8.152Å, c=6.098Åand β=98.27° at room temperature [40]. The structure consists of Ni^{2+} chains along the crystal c axis and each Ni^{2+} is bridged by N_3^-, as shown in Fig. 3.20. Two 2,2-dimetyl-1,3-diaminopropane (dmpn) groups are connected with covalent bonding to a nickel ion and stacking along the crystal a axis with those of the adjacent chain. ClO_4^- anions separate each chain.

It is noteworthy that all Ni^{2+} sites are crystallographycally equivalent, while NENP has two inequivalent Ni^{2+} sites due to the bridging of NO_2^-. Thus, it is expected that the transverse staggered moment in case of NDMAZ is not induced under external fields, as shown in Fig. 3.21.

3.5.2 Magnetic properties

The magnetic susceptibilities of the single crystal of NDMAZ [2] are shown in Fig. 3.22. Though the data exhibit some anisotropy, still they give qualitatively the same results as those of NENP. The data show a broad peak at around 90K and exponentially decreases with lowering temperatures as given by eq. (3.3). The inset suggests rather large field dependence of Haldane gap along with the chain axis than that perpendicular to the chain, as is seen in case of NENP.

Previously, T.Takeuchi *et al.* have reported the magnetic susceptibility of the polycrystalline sample of NDMAZ [41] and fit the data to the theoretically calculated one with the parameters of g=2.21, J/k_B=−70.6K. They also estimated the magnitude of Haldane gap by fitting with eq. (3.3) and gave the value of E_g/k_B=22K. The authors have also presented the high-field magnetization process under magnetic fields up to 30T, as shown in Fig. 3.23. The field dependence of magnetization shows that the critical field H_c is at around 14T.

The results of the nuclear magnetic resonance measurement by S.Satoh and coworkers [42] are shown in Fig. 3.24. The shifts at higher temperature are attributed to the uniform magnetization of chains. The staggered field was not observed on NDMAZ under external fields up to 4T. The absence of the staggered moment implies that the possibility of 3D-LRO under high magnetic fields still remains.

Some parameters of NDMAZ are summarized in Table 3.2.

3.5.3 Previous study by RIKEN group

Before showing our result, we examine the heat capacity measurement of NDMAZ performed by RIKEN group. The results are shown in Fig. 3.25. The remarkable peak at around 0.6K under magnetic field of 12T is observed and they elucidated it as the occurence of 3D-LRO. The measurement were performed by means of the relaxation method.

However, the values of heat capacity below 0.6K are less than the caluculated ^1H nuclear spins portion. It is clear that they do not observe the whole amount of heat capacity of the

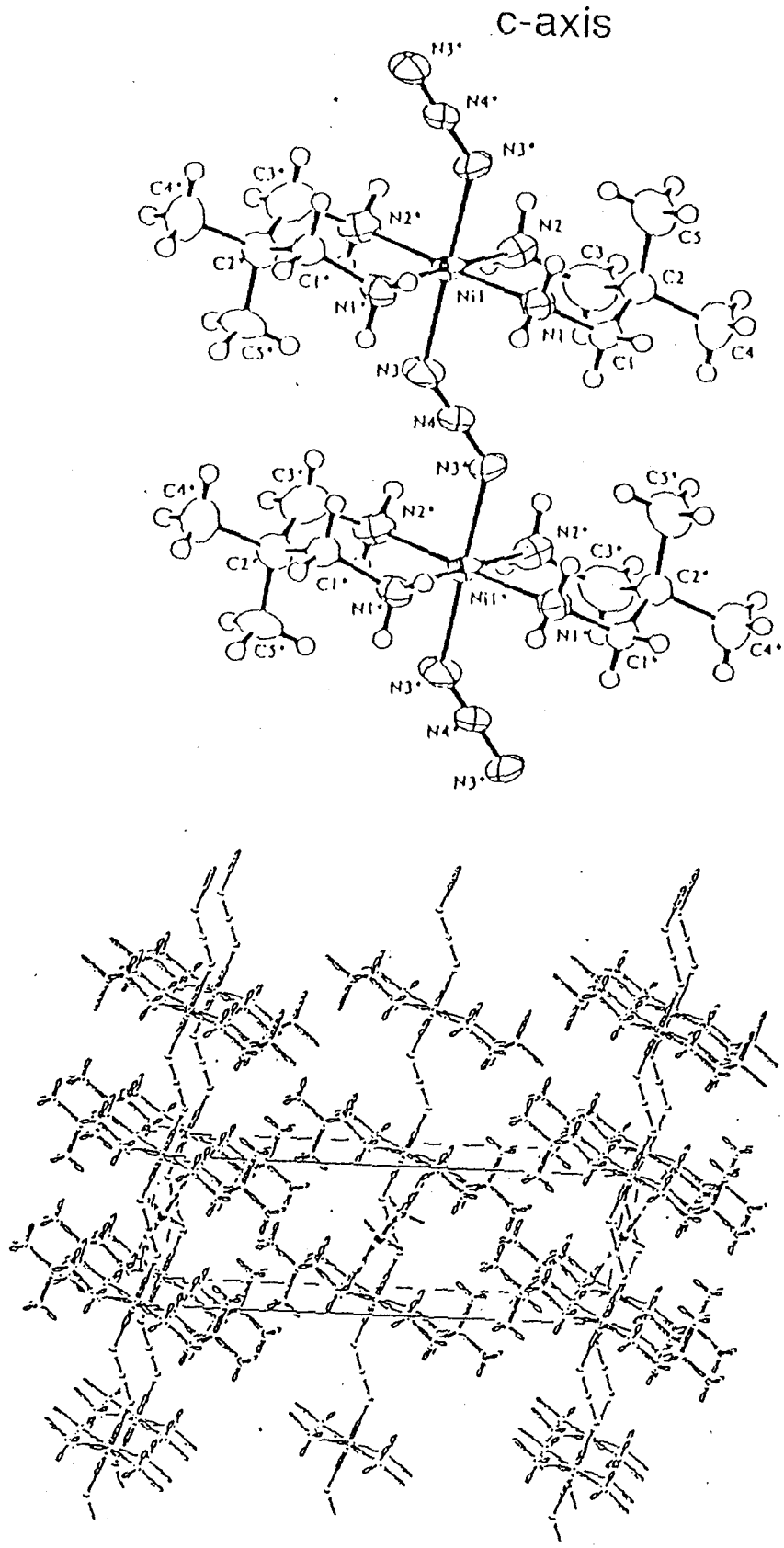

Figure 3.20: The crystal structure of NDMAZ.

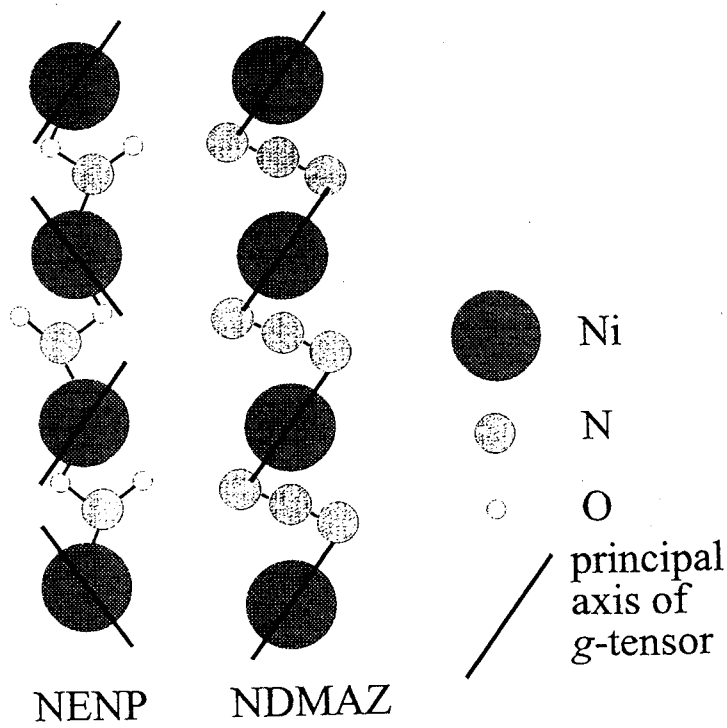

Figure 3.21: Schematic view of the structural difference between NENP and NDMAZ.

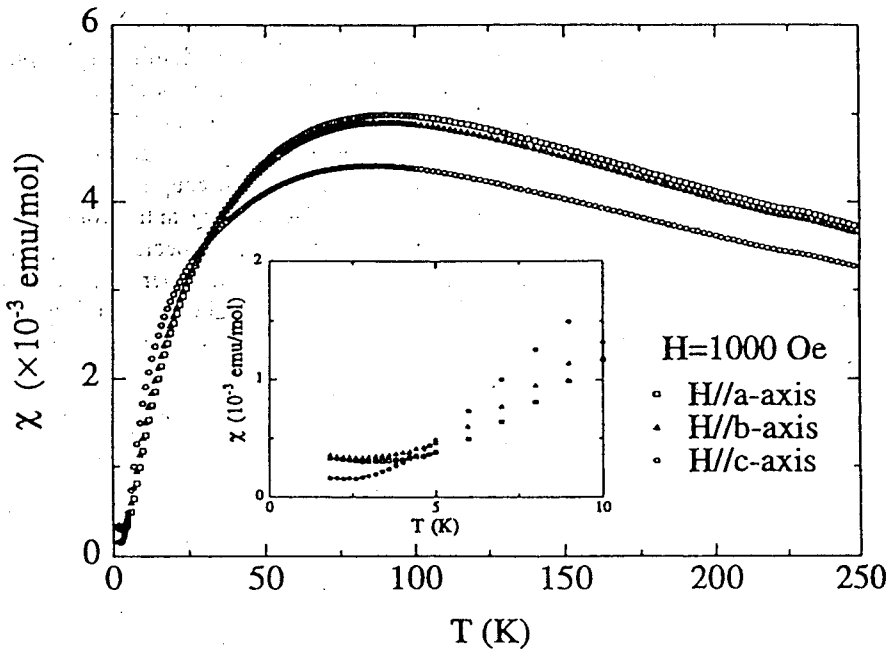

Figure 3.22: Temperature dependence of susceptibility along the crystal a, b and c axes of a single crystal sample of NDMAZ. The inset shows the low temperature part. [2]

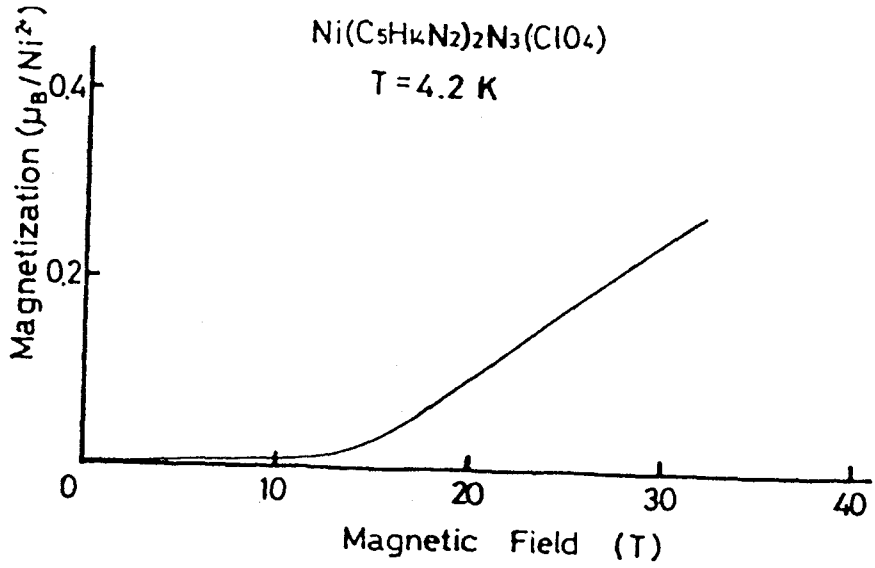

Figure 3.23: High field magnetization process of polycrystalline NDMAZ at 4.2K. [41]

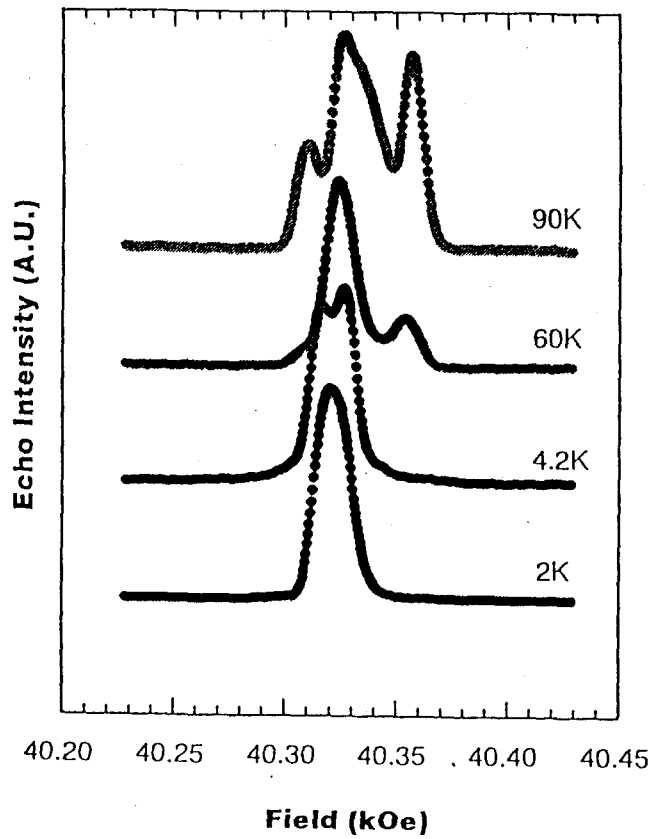

Figure 3.24: Resonance spectrum of ^{1}H in NDMAZ at f=170MHz [42]. The shift at higher temperature is attributed to the uniform magnetization of chains. No sign of the staggered moment is observed.

molecular weight	M	=	404.2
lattice constants (monoclinic)	a	=	18.860 Å
	b	=	8.152 Å
	c	=	6.098 Å
	β	=	98.27 °
exchange constant	J/k_B	=	–70.6K
energy gap	E_g/k_B	=	21.6K
critical field	H_c	$\sim$	14T

Table 3.2: Lattice and physical constants of NDMAZ.

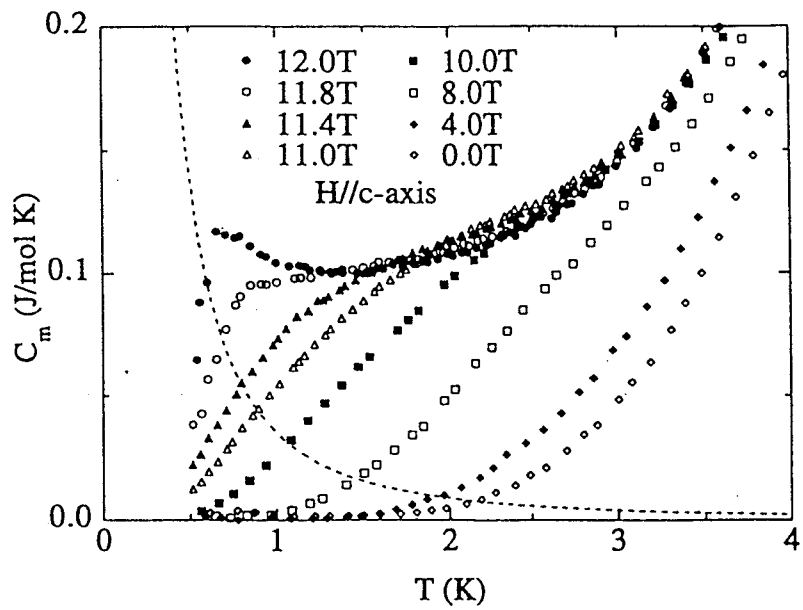

Figure 3.25: Magnetic heat capacity of NDMAZ under magnetic fields parallel to c axis up to 12T [2]. The dotted line is the calculated nuclear magnetic contribution of ^{1}H under the magnetic field of 12T.

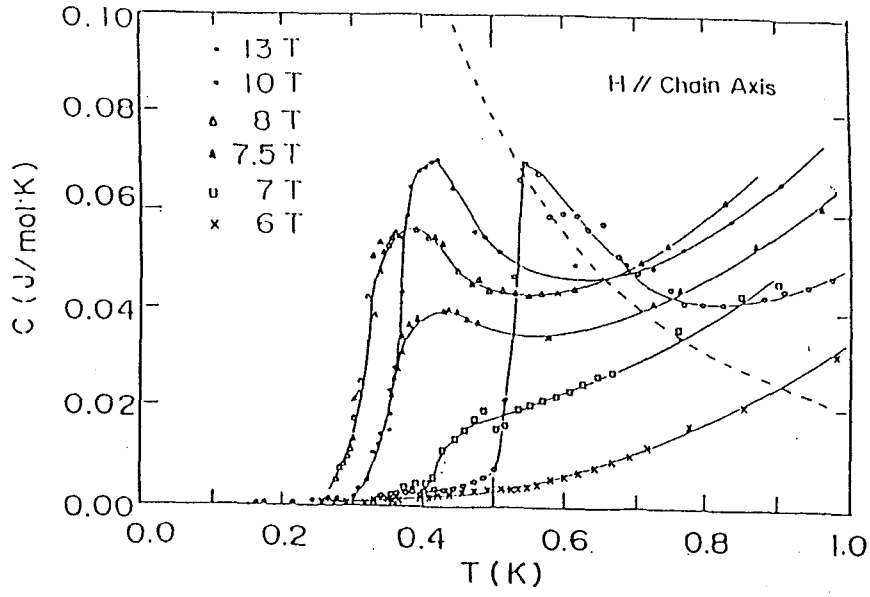

Figure 3.26: An apparent peak of heat capacity of NENP. (see text) The dashed line is the calculated nuclear magnetic contribution of ^{1}H under the magnetic field of 13T.

sample. Under high fields and at low temperatures, the nuclear spin show a considerably small thermal relaxation rate and it causes that the measurement evaluates the partially relaxed state, as seen in case of NENP [3]. (Fig. 3.26) That is to say, the relaxation exceeding the limit of the calorimeter is ignored and it results in an apparent peak.

Related with this, the authors analyzed data of the relaxation profile at T=0.5K, supposing two components of the thermal relaxation. They claimed that the measurement were done under the conditions that the nuclear spin system is thermaly isolated. They also pointed out that the change of heat capacity between H=11.8T and 12T is hardly explained by the change of the nuclear spin portion.

In Haldane gap system, however, the relaxation time constant may drastically change with approaching to the critical field H_c. If 3D-LRO occurs, it should become comparable to that of the electron spin system. Additionally, by the reasons stated in Chapter 2, the relaxation method is not suite for the measurement under such condition that the nuclear magnetic contribution is present. This obscurity must be solved by measuring heat capacity including the nuclear spin system by means of the adiabatic method.

Chapter 4

Experimentals

4.1 Sample preparation

Single crystals of NDMAZ were synthesized for the first time and supplied by M.Yamashita *et al.* of Graduate School of Human Information, Nagoya University [40]. The compounds are obtained by mixing of [Ni 2,2-dimethylpropylenediamine]$(ClO_4)_2$ and NaN_3 in aqueous solutions. Rectangular plate shaped single crystals (typical dimensions; $2\times0.5\times4mm^3$) are obtained by slow evaporation.

Diffraction data were collected at room temperature on a four-circle diffractometer (Rigaku AFC-5R) with a rotating anode generator and Mo Kα radiation (λ=0.71069Å) monochromated by a graphite plate.

The chain axis is along with the long axis of single crystal.

4.2 Heat capacity measurement

Experiments were performed with a hand-made $^3He/^4He$ dilution refrigerator (DR) assembled with a superconducting magnet (Oxford Instruments). The magnet generates a magnetic field of 12T@4.2K and 14T@2.2K, respectively. In the early stage, experiments were performed with another DR (Oxford Instruments) assembled with a 13T magnet (IGC), which has a field compensation coil.

On both cases, measurements were performed by means of the conventional heat pulse method with a mechanical heat switch. Further details of the measuring scheme are described in Chapter 2. 86mg of single crystals are attached to Cu plate with `Apiezon-N` grease for the thermal contact and c-axis is aligned along the field direction.

4.3 Magnetization measurement

The magnetization measurement was carried out by the use of the capacitance load cell. This method has many advantages on measuring under very low temperatures and high magnetic fields. In this section, the principle is briefly described.

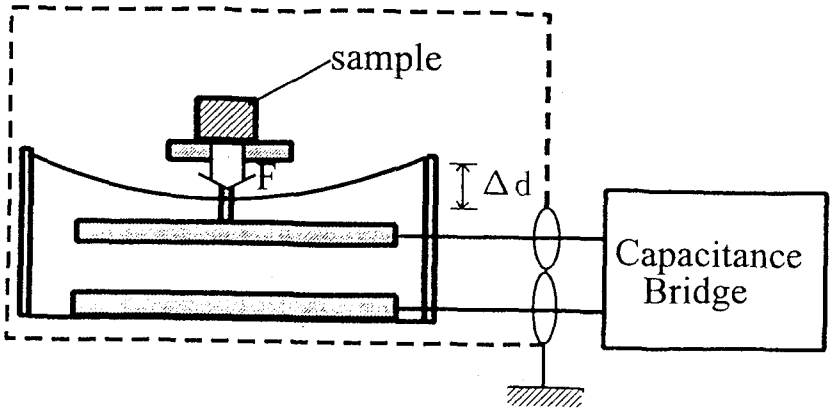

Figure 4.1: Principle of the magnetization measurement in use of the capacitance load cell.

4.3.1 Principle of the measurement

Our measurement system is based on that developed in Sakakibara laboratory, Hokkaido university. The outline of the measurement system is described in Ref.[43].

Under the existance of the magnetic field gradient, the sample experiences the force F in propotional to the magnetization M, given by;

$$F = M\frac{dH}{dz}, \tag{4.1}$$

and moves from the ballanced position by Δd, as shown in Fig. 4.1. The displacement Δd is able to be known through the change of the capacitance C from the relation,

$$C = \frac{\varepsilon S}{d}, \tag{4.2}$$

$$\Delta d = \varepsilon S\left(\frac{1}{C} - \frac{1}{C_0}\right), \tag{4.3}$$

where ε is permittivity, S is the surface area of the capacitor and C_0 is capacitance at the ballanced position.

4.3.2 Experimental details

On our system, the most different point from that of Sakakibara laboraory is that we use the inhomogenity of the magnet (10^{-3}/cm DSV), while they employs the additional coil for the field gradient. The load cell is placed at about 4cm upper position from the center of the magnet, where the magnitude of the field gradient is about 1200gauss/cm@12T. As the sensitivity increases with the central field value, the load cell has higher sensitivity for higher magnetic field.

Block diagram of the magnetization measurement system is shown in Fig. 4.2. Capacitance of the load cell is measured by an auto ballancing capacitance bridge Andeen-Hagerling 2500A, which has high resolution of 5×10^{-7}pF and high stability on temperature of 0.1ppm/°C.

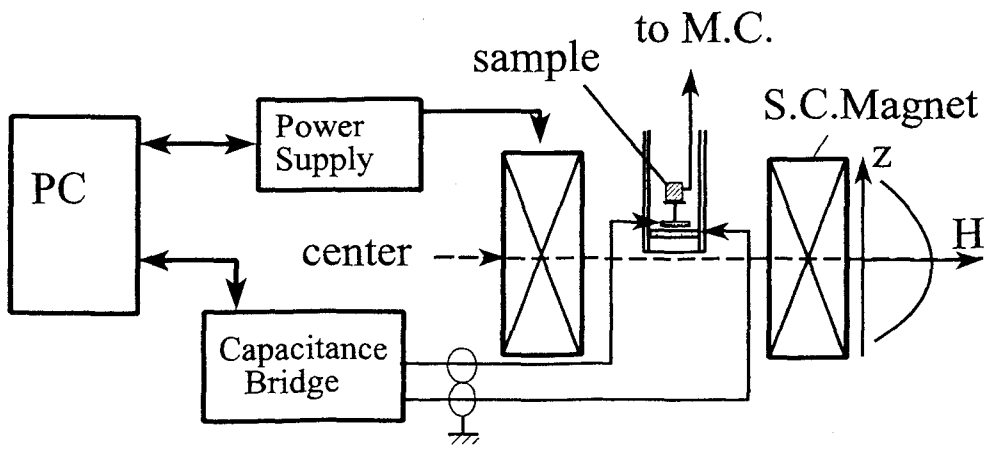

Figure 4.2: Block diagram of the magnetization measurement system

Movable side of the capaitor is made of epoxy resin (Stycast #1266) and suspended by the wires of phosphor bronze which act as the spring. The diameter of the electrode is 2.2cm and its surface is painted with silver paste. At room temperature, the capacitance is typically ~4pF and the spring constant is approximately 5×10^{-3}mm/gw. Of course, these values are dependent with temperature, so the calibration for both magnetic field and sensitivity must be performed at low temperature.

Stacked Cu foils are used in order to obtain thermal contact between the sample and the mixing chamber of DR where a RuO_2 thermometer is placed.

Chapter 5

Results and discussions

5.1 Heat capacity

In Fig. 5.1, the heat capacity data of the single crystal of NDMAZ obtained within our experimental range of the temperatures down to 0.2K and the magnetic fields up to 14T is shown by $C/T - T$ plot. The background including the nuclear magnetic contribution of Cu, which is used as the addenda, is subtracted by the separate run. In the present study, the external field is applied along the crystal c axis for which the lowest transition field is expected.

Field dependence is seen below 4K and the broad anomaly at around 3K slightly moves to lower temperatures with applying the external field from 0T to 9T, which is ascribed to the field dependence of the energy gap. Above 4K, a roughly estimation with eq. (3.6) gives the lattice contribution βT^3 with the value of β=0.022(J/K^{3}mol), which is comparable with that of NENP, β=0.0053(J/K^{3}mol). To obtain the magnetic heat capacity C_m, the lattice contribution should be subtracted from the total heat capacity C. However, its contribution is negligibly small below 1K, so that we may use C in the following analysis. It should be noted that heat capacity under zero external field is larger than those under the fields of 5 and 9T. That implies the existence of the paramagnetic portion, which may be attributed to the paramagnetic impurities and/or the degree of freedom of chain-end spins as seen in case of NENP. Anyhow, it is sufficiently saturated under the magnetic fields of 5T.

The heat capacity below 1K is enlarged in Fig. 5.2. It is remarkable that the field dependence is seen at around 0.6K. We consider that up-turn of the heat capacity at lower temperatures originates from the nuclear magnetic heat capacity of the protons which are contained in NDMAZ. and gives the Schottky type anomaly due to the Zeeman spilitting of the nuclear spin moment of the proton. Thus the heat capacity of the electron spin system is obtained by subtracting the nuclear magnetic portion from the total heat capacity. By the higher temperature approximation, the anomaly is given by;

$$\frac{C}{R} = \frac{1}{4}\left(\frac{\Delta}{T}\right)^2 \ (^1\text{H–atom}^{-1}), \tag{5.1}$$

where $\Delta = \mu_N H/k_B = 2.043 \times 10^{-3}(\text{K/T}) \times H$, we have shown the calculated contribution of the nucelar spin system at H=13T in Fig. 5.2 by the solid line. It is clear that our results

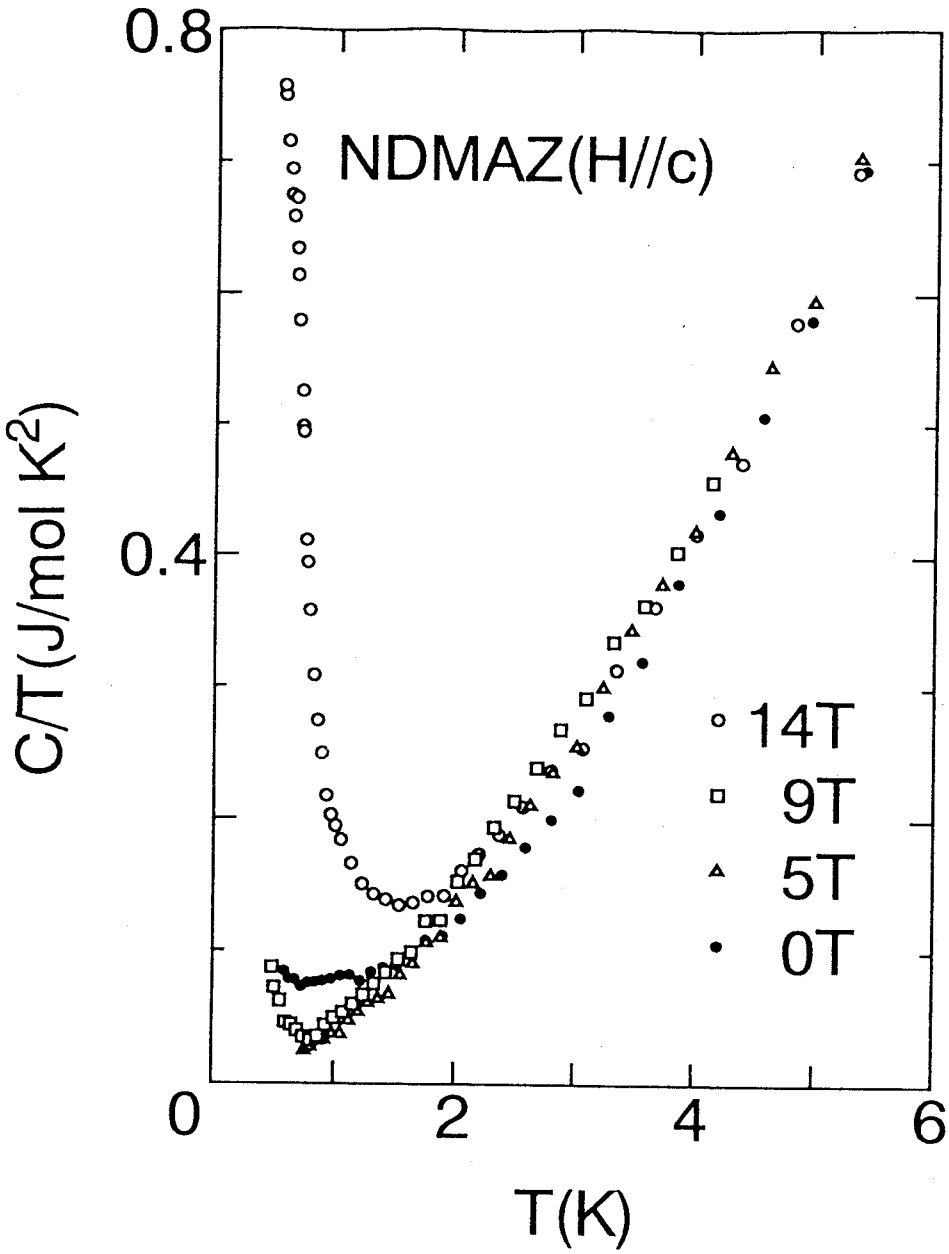

Figure 5.1: Heat capacity of the single crystal of NDMAZ by $C/T - T$ plot within our experimental range of the temperatures down to 0.2K and the magnetic fields up to 14T. The magnetic field is applied along the crystal c axis in the present study for which the lowest transition field is expected.

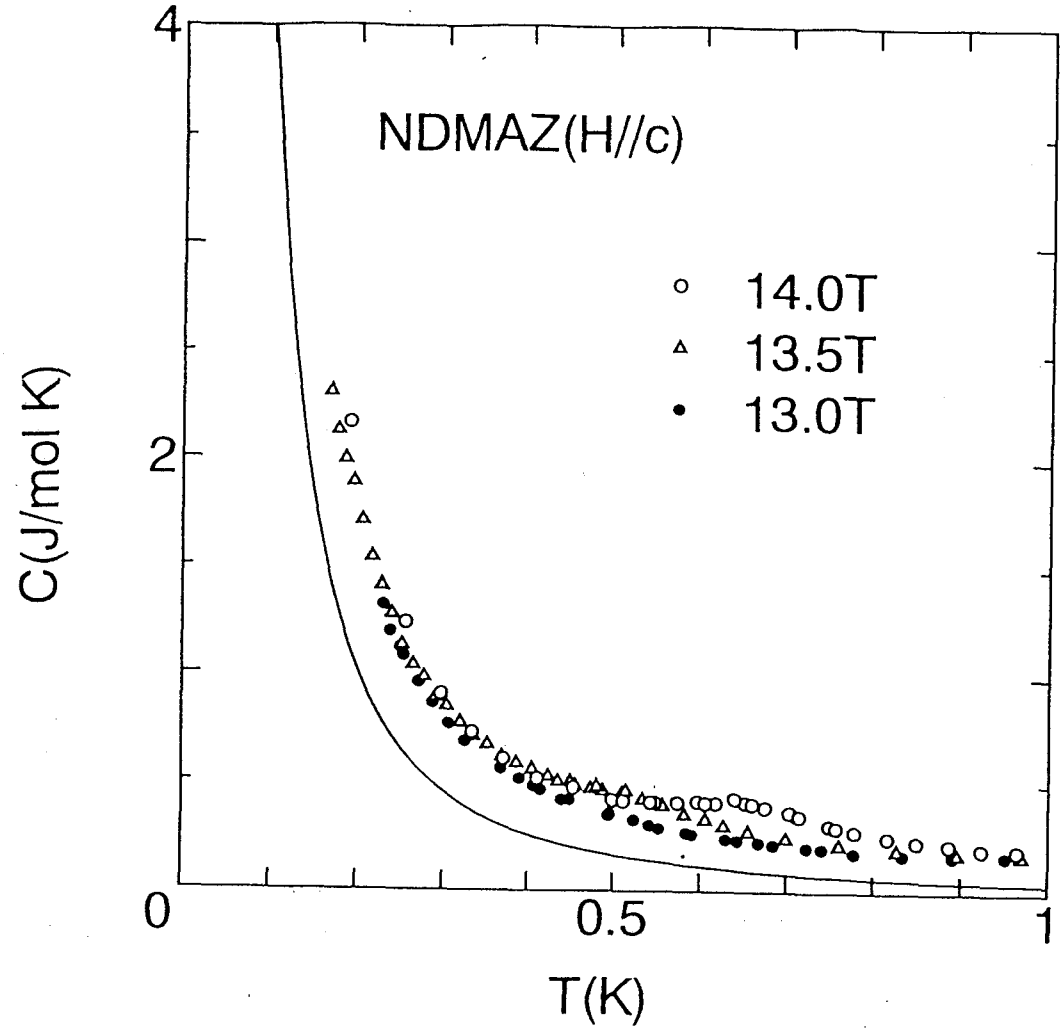

Figure 5.2: Heat capacity of NDMAZ below 1K and above 13T by $C-T$ plot. The solid line is the calculated nuclear magnetic contribution of ^{1}H at H=13T.

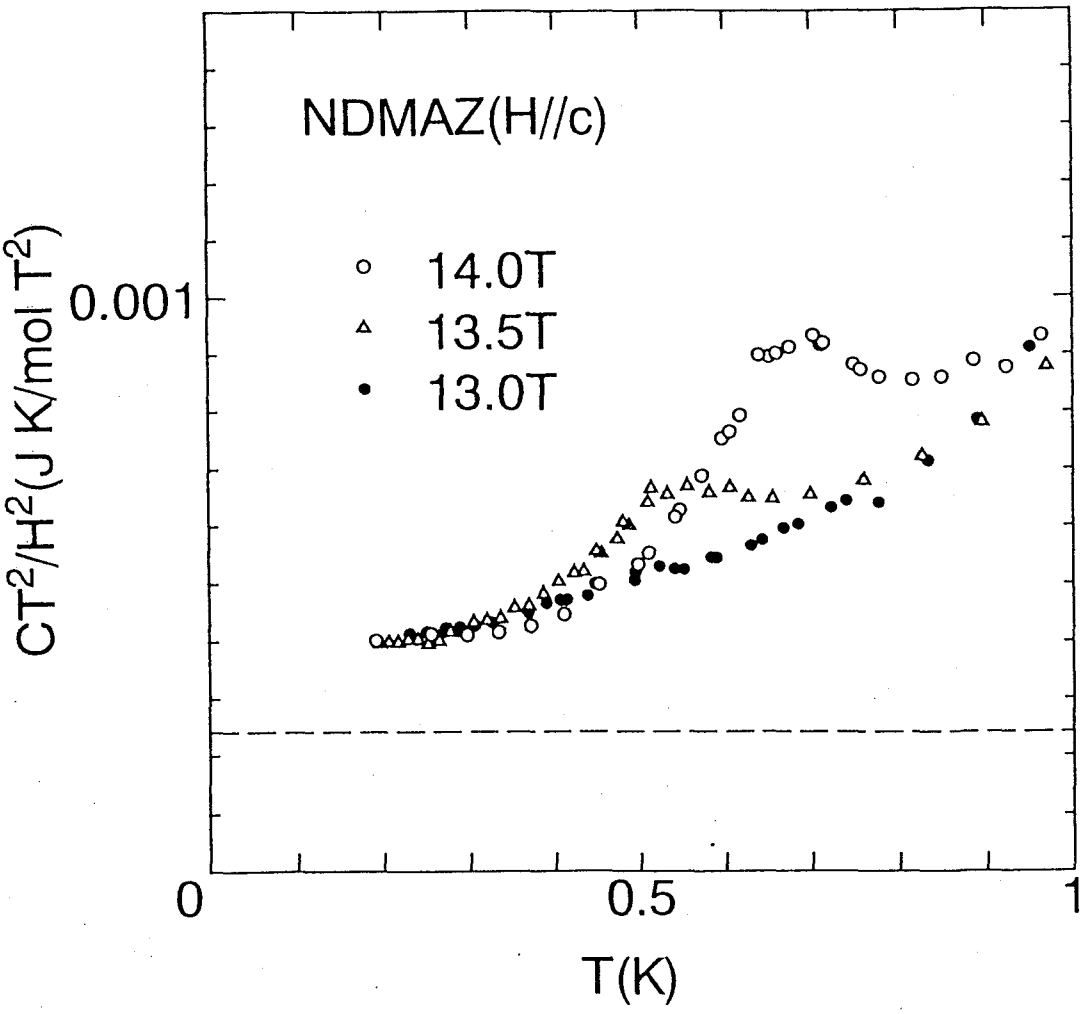

Figure 5.3: Heat capacity of NDMAZ below 1K and above 13T by $CT^2/H^2 - T$ plot. The broken line is the expected nuclear magnetic portion of the proton.

are larger than the expected nuclear magnetic portion of the proton at the whole range of the temperature. In order to clarify the dicussion, we plot the result by $CT^2/H^2 - T$ plot in Fig. 5.3. It is noticeable that the heat capacity at lower temperatures can be scaled by H^2/T^2. This fact suggests that the difference between the result and the expected nuclear magnetic contribution of the proton may be attributed to the nuclear magnetic one of the other nuclear species than the proton. It is difficult to be explained by the mis-subtraction of the nuclear magnetic contribution of the copper contained in the addenda because of the coincidence with the earlier result by another calorimeter. We will discuss this discrepancy later.

By subtracting the contribution obeying H^2/T^2 law, it is clearly seen that a sharp peak appears at around 0.5K. The peak moves to higher temperature with increasing the magnetic field up to 14T, as shown in Fig. 5.4. The heat capacity at higher temperature obeys T-linear law, which is expected by the spin wave theory. Although the reduced coefficient of temperature γ_m=9.3, which is geven by the formula $C/R = \gamma_m k_B T/|J|$ with the exper-

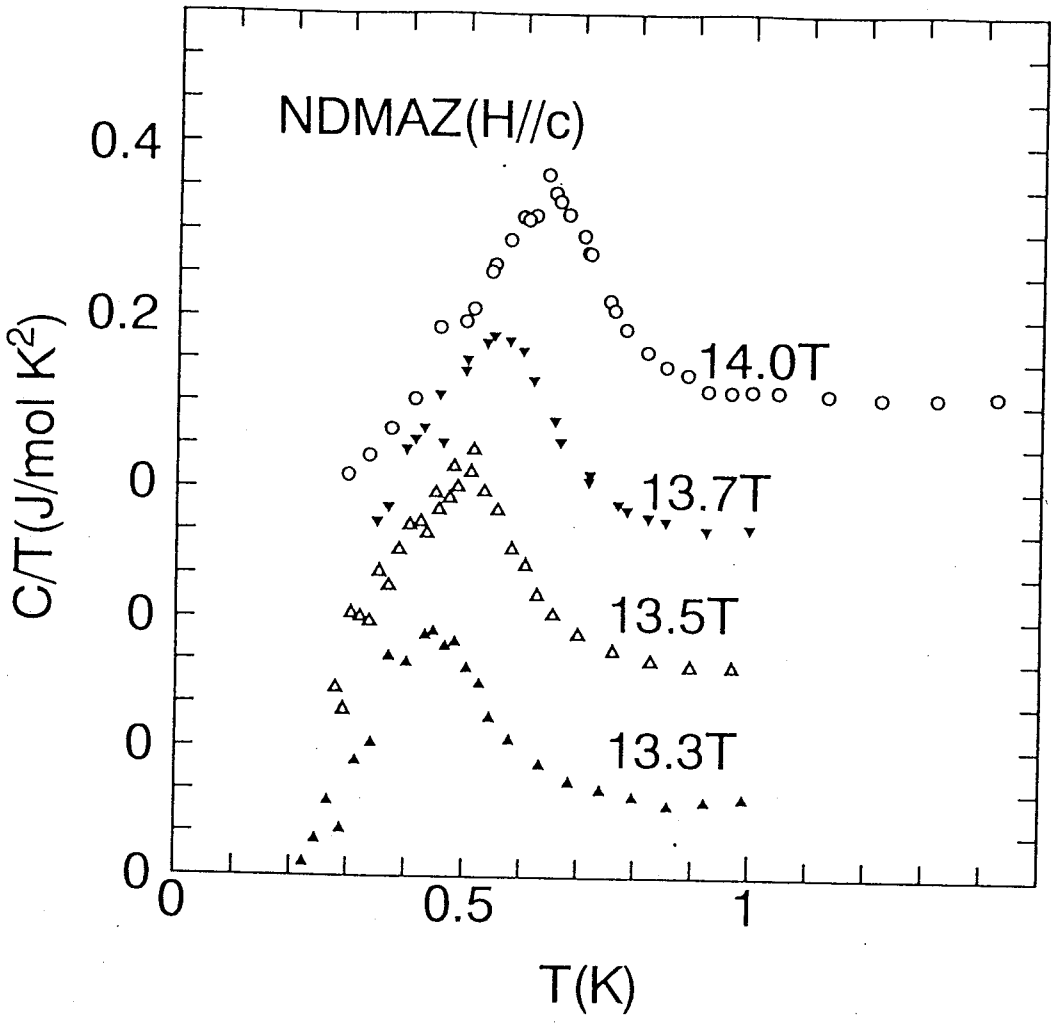

Figure 5.4: Heat capacity of the electron spin system of NDMAZ by $C/T - T$ plot. To clarify the subsequent runs, each data are shifted by 0.15J/molK^2.

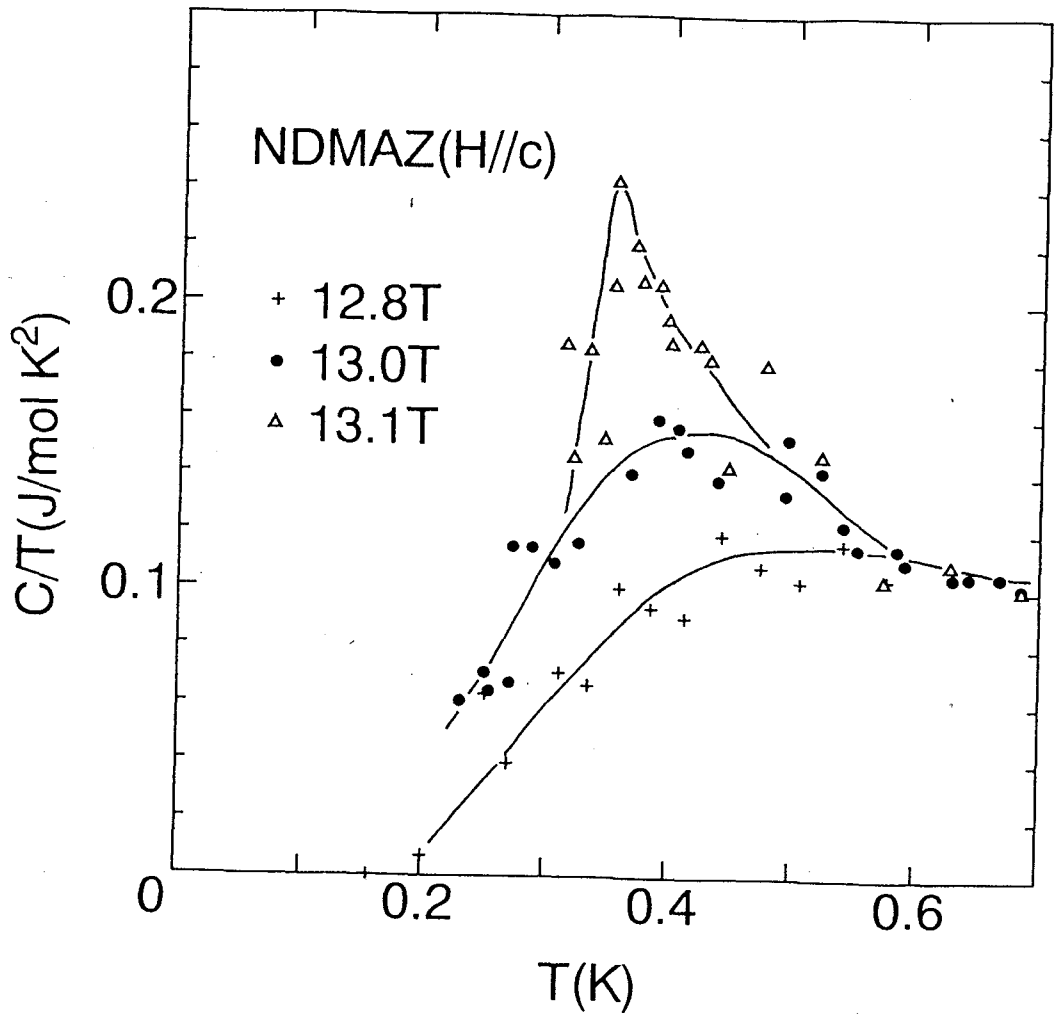

Figure 5.5: Heat capacity of the electron spin system of NDMAZ by $C/T - T$ plot in the vicinity of H=13T. The solid lines are guides to the eye.

imental value of J/k_B=−70.6K, is considerably larger than that of NENP, γ_m=0.26, the evaluation of the entropy change ΔS=0.05(J/Kmol) is roughly equal to the rest of the entropy. Therefore, we consider that the peak is ascribed to 3D-LRO of the electron spin system.

The heat capacity under the relatively low magnetic field is shown in Fig. 5.5. In spite of the scattering of the data, the sharp peak is seen under the magnetic field of 13.1T. However, with decreasing the external field, the peak disappears abruptly. Under the magnetic field of 12.8T, no anomaly other than the steep drop of the heat capacity is observed, suggesting the existence of the energy gap. Of course, there exits the possibility that the thermal relaxation time constant exceeds the limit of the calorimeter. It is, however, noteworthy that the heat capacity at around 0.5K does not vary with respect to the external field between 13.0 and 13.1T. It is considered that the short range ordering (SRO) develops in this temperature range but the rest of the entropy is gradually removed, reflecting the energy gap, in case of H=13.0T. Thus we may conclude that the lower end of the phase

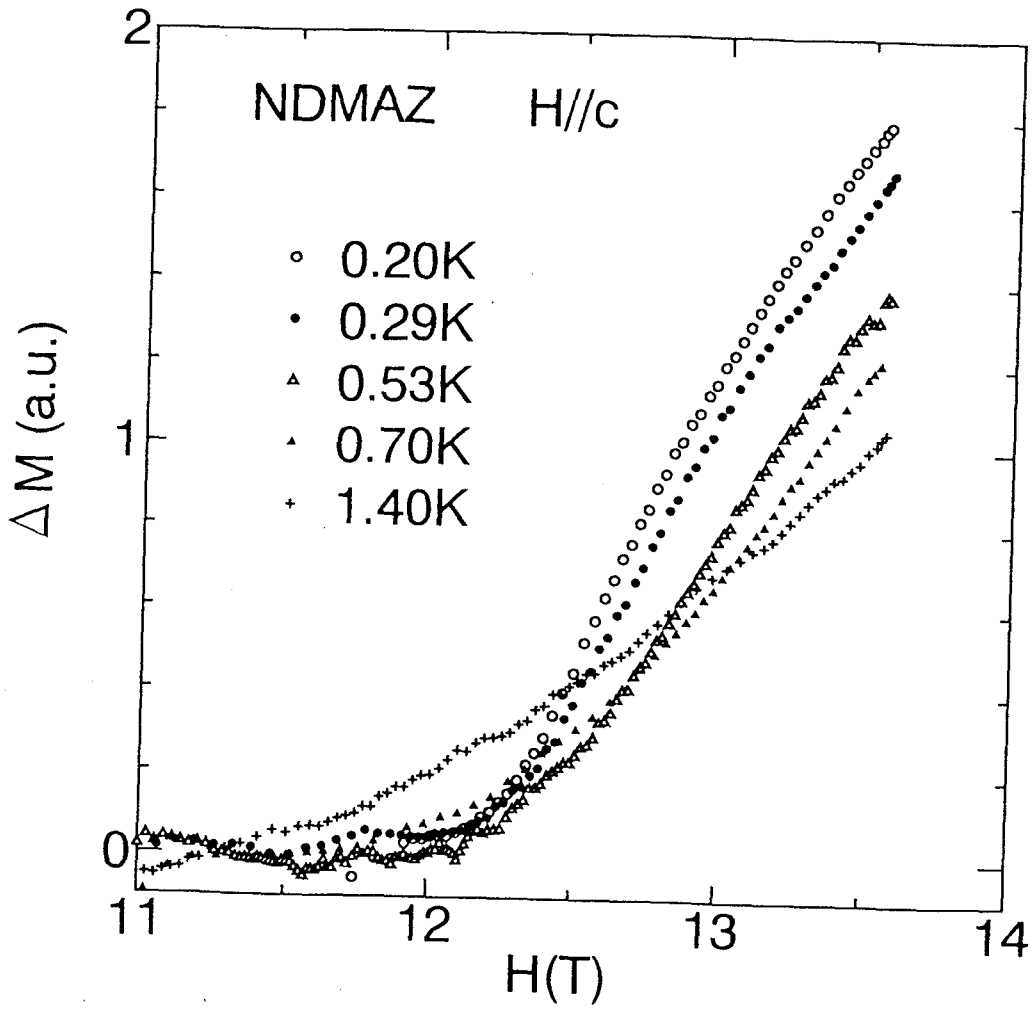

Figure 5.6: High field magnetizaion process of the single crystal of NDMAZ at various temperatures and under the static magnetic field.

boundary exists between 13.0 and 13.1T

5.2 Magnetization

In order to obtain the supporting evidence for the result of heat capacity, we carried out the magnetization measurement. The results are shown in Fig. 5.6. Unfortunately, the magnetometer is still uncalibrated, so that the magnetization is normalized with the value at H=11T and the magnetic field is estimated by the use of the field profiles at H=12T. The sweep rate of magnetic field is 0.1T per minute.

The magnetization appears suddenly and increases almost linearly above about 12T, as previously reported by use of the pulsed magnetic field [41]. It is remarkable that the magnetization at the lowest temperature of 0.20K appears with steeper derivative with respect to field and with a negative curvature above H=12.5T. With increasing temperature, the magnetization is found to increase with initialy a negative and then a positive curvature.

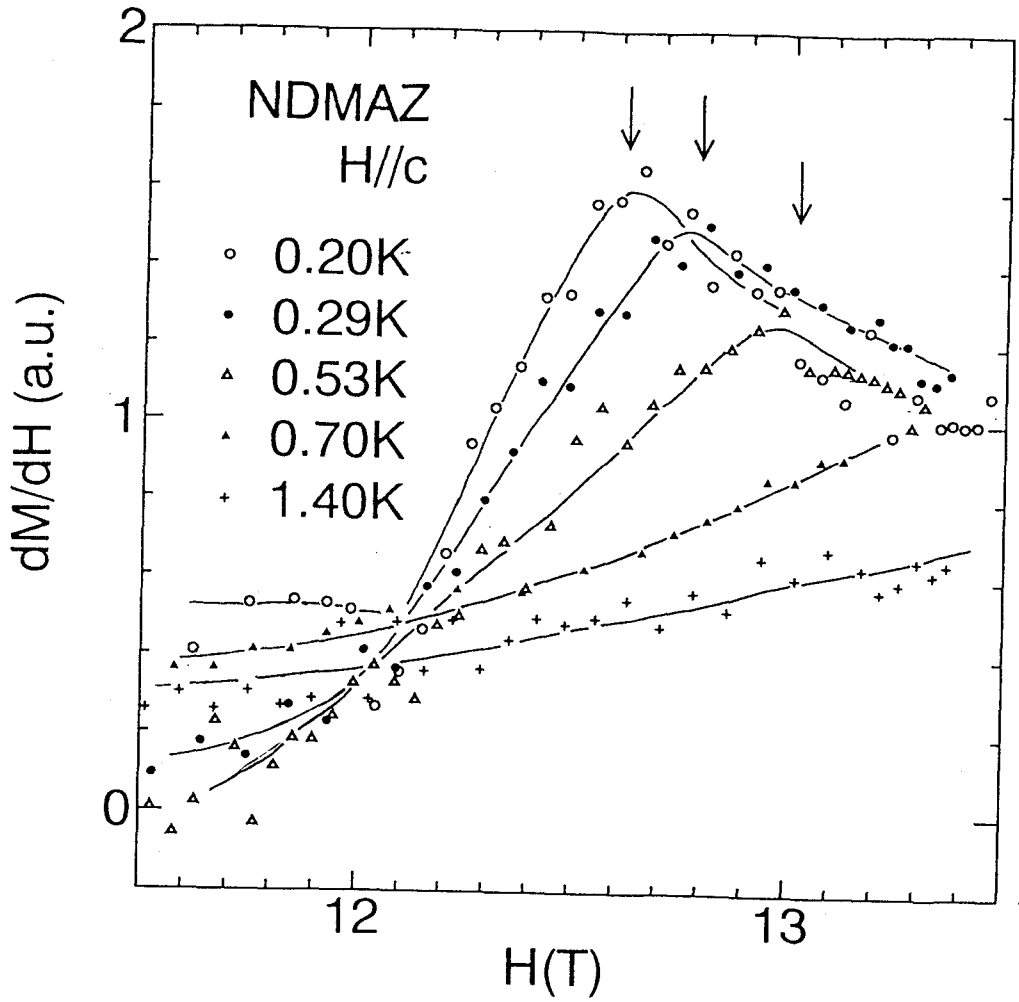

Figure 5.7: Derivative of the magnetization with respect to H. Arrows indicate the maxima of the derivative curve at various temperatures. The solid lines are guides to the eye.

The inflection point moves to higher magnetic field and becomes somewhat broadened. At the temperature of 1.40K, it clearly shows a positive curvature.

To clarify the data, the magnetization curves are numericaly differentiated with respect to H, as shown in 5.7. In spite of the scattering of the data, the derivative curves at lower temperatures than 0.70K show the maximum value while those at higher temperature than 0.70K monotonically increase within our experimental range. The maximum of the derivative curve clearly moves to higher magnetic field with increasing temperature.

In general, such a peak may be observed at the lowest temperature limit in Haldane gap antiferromagnet, as seen in case of NENP [26, 27]. Additionally, several theoretical works [45, 46, 47, 48] suggest the divergence of the field derivative at H_c. Though no theory at the finite temperature is available, the temperature dependence of the peak which we observed is hardly explained as the shift caused by simple thermal effect. Moreover, the difference of the curvature below and above T=0.70K is remarkable. We consider that it suggest the spin-flopping due to field-induced 3D-LRO.

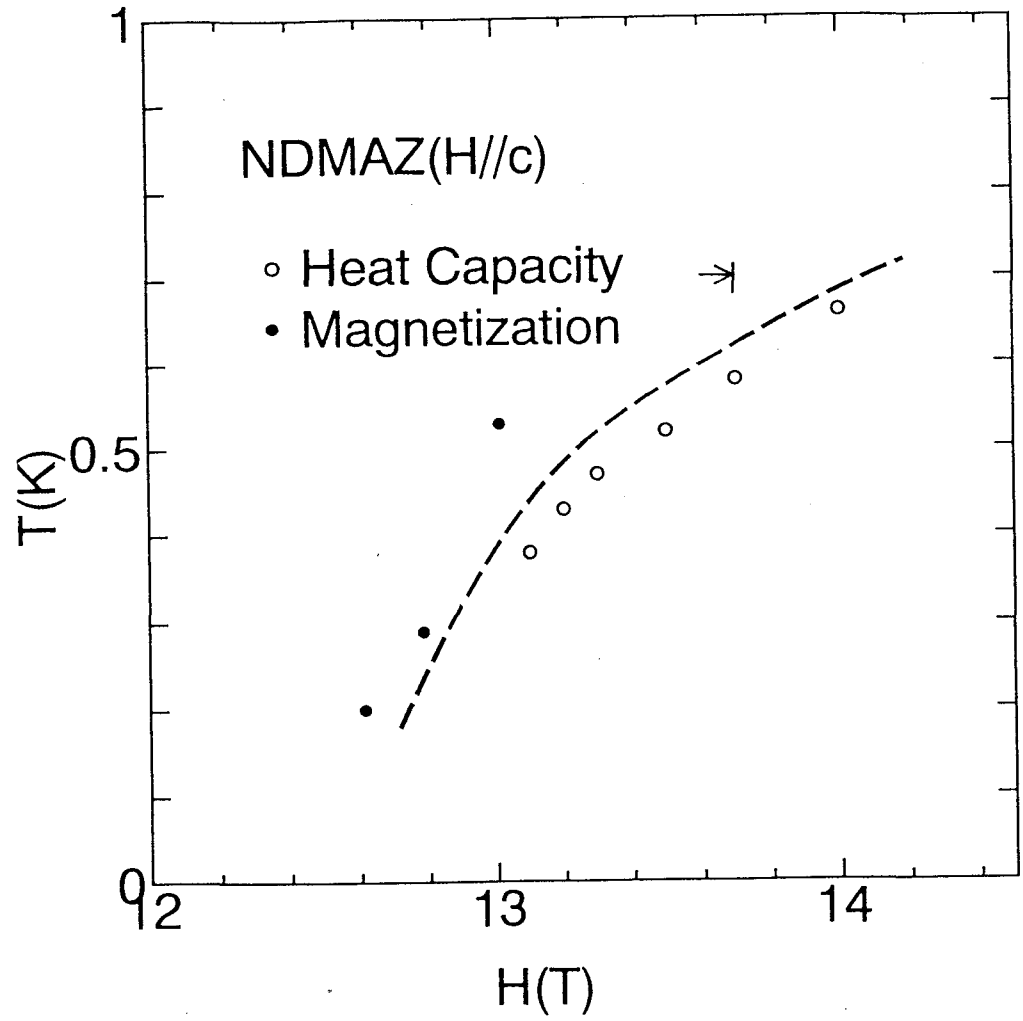

Figure 5.8: Phase diagram of the field-induced 3D-LRO of NDMAZ under the magnetic field applied along with c crystal axis. Open circles and closed circles are corresponding to the peak of heat capacity and the point of inflexion of magnetization, respectively. The broken line is guide to the eye.

5.3 Discussion

The phase diagram obtained in the present study is shown in Fig. 5.8, where open circles and closed circles are corresponding to the peak of heat capacity and the inflection point of magnetization, respectively. Taking the fact that the magnetization curve at T=0.70K shows no inflexion point with respect to the magentic field up to H=13.6T, into consideration, the results of high field magnetization support the field dependence of phase boundary of 3D-LRO obtained by heat capacity measurements. Deviation between these two measurements is surprisingly small and we consider that it may be mainly caused by the uncertaintity of the field calibration of the magnetization measurement. Or, in general, the spin systems with the energy gap quenching often show the adiabatic magnetization cooling in the imperfect isothermal case. It causes rather high transition temperature than

the real temperature of the spin system.

It is noteworthy that the ordered phase still exists under the field up to 14T. Theoretically, T.Sakai and M.Takahashi showed the possibility of 3D-LRO of the quasi one dimensional Haldane gap antiferromagnet by calculating the staggered susceptibility at the thermodynamical limit [46]. Assuming the molecular field approximation, 3D-LRO may exist in the range of the external field from just below H_c to the saturation field. This result supports our data.

In comparison with the previous work of RIKEN group, the transition (T=0.6K, H=12T) they argued is definitely far from the phase boundary which we obtained in spite of the necessary field calibration. The fact that their data at around the field where an anomaly is seen do not show T linear dependence, strongly implies that the separation between the electron spin system and the nuclear spin system is incomplete.

Now we consider the rest part of the heat capacity. As described before, the heat capacity shows a difference from the expected nucear magnetic part of the proton at very low temperatures. Since it is scaled by H^2/T^2, we can not attribute it to the splitting due to the nuclear quadrupole moment of, such as ^{14}N (I=1), ^{35}Cl (I=$\frac{3}{2}$) and ^{37}Cl (I=$\frac{3}{2}$). The possibility of the internal field due to 3D-LRO also seems to be negative because the difference still remains even under the magnetic field less than 13T, where no sharp peak is observed.

The gyromagnetic ratios of the other nuclei than the proton are one order smaller than that of the proton. Moreover, the number contained in the sample per mole is less than that of the proton. For example, an estimation for the ^{14}N nuclei gives three order smaller value than the rest contribution. If we assume the transfered hyperfine coupling at ^{14}N nucleus site, the enhancement is roughly 14 times as large as the external field. The origin is still unknown.

The recent result of magnetization process of the single crystal of NDMAZ under pulsed magnetic field is shown in Fig. 5.9. The obtained magnetization process gives qualitatively the same behavior as that of NENP [27] and suggests the existence of H_c at about 15T. It is noteworthy that the result at T=1.4K shows a negative curvature just above H_c. Though it is not clear if the inflection point arises from H_c or 3D-LRO, the possibility of 3D-LRO seems to be negative because the magnetization curves above H_c show no difference between T=1.4K and T=4.2K. We emphasize that the singularity is not seen at around 13T where we observed an abrupt increasing of magnetization at the reached lowest temperature.

Though 3D-LRO of Haldane gap antiferromagnet is realized, the picture of the ordered phase is still unknown. Further experimental, as well as theoretical, investigation of the ordered phase is required.

5.4 Summary

We have observed 3D-LRO of the Haldane gap antiferromagnet NDMAZ under the magnetic field $H \simeq$13T applied parallel to the crystal c axis and at temperature of $T \simeq$0.3K by means of the heat capacity and the magnetization measurement. Applying the higher external field, the transition temperature increaces up to $\simeq$0.7K at14T, showing a negative curvature with respect to the external field.

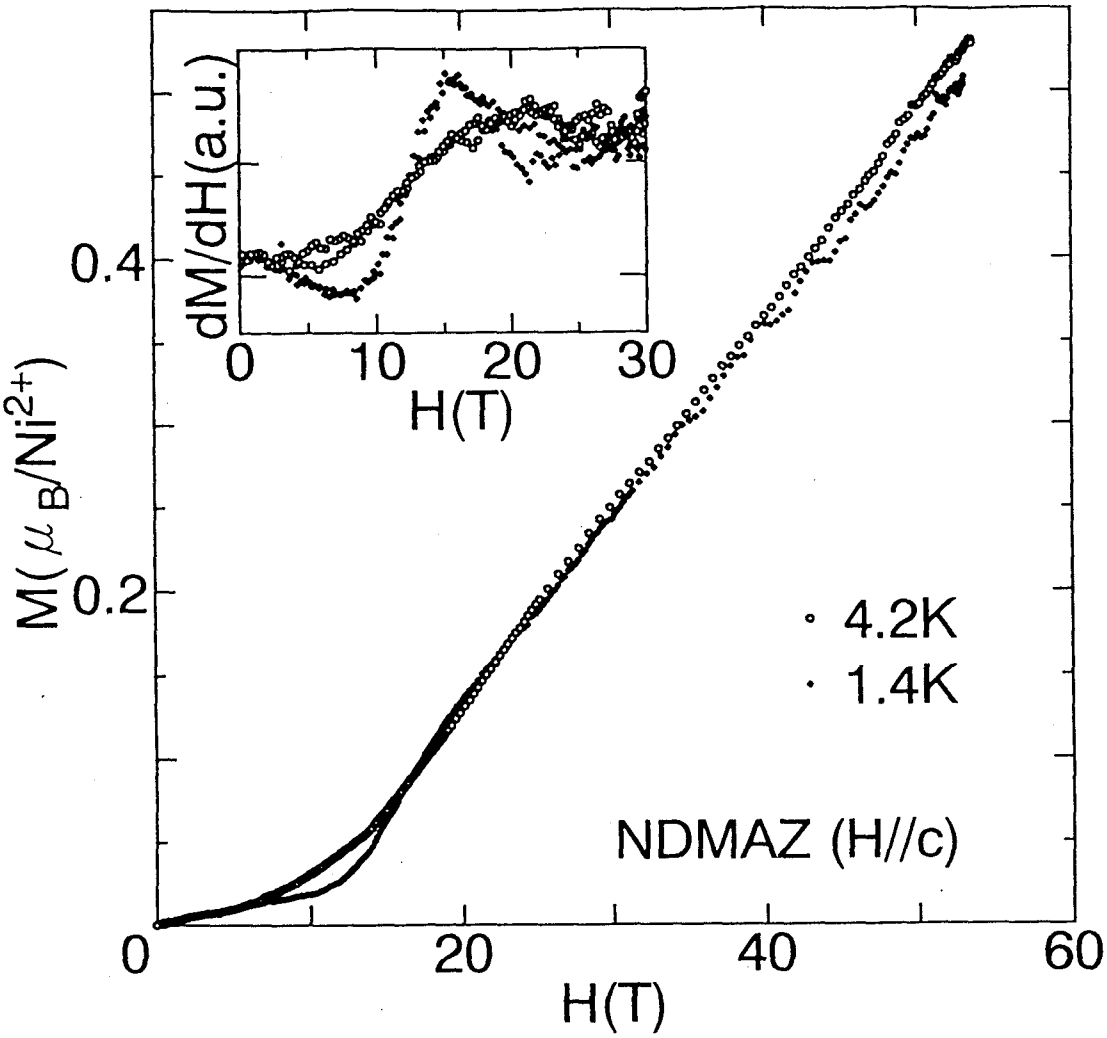

Figure 5.9: Magnetization curves under pulsed magnetic field applied to the crystal c axis. The inset shows the derivative curves of the magnetization with respect to H.

It is considered that the crystallographcally equivalent Ni^{2+} site is crucial for realizing 3D-LRO due to the gap-quenching in comparison with the previous result of other Haldane gap antiferromagnet, such as NENP.

Part III

Heavy Fermion Superconductor UPt_3

Chapter 6

Introduction

UPt_3 is the most fascinating heavy fermion superconductor (HFS) for its impressively complex phase diagram of the superconducting state, as shown in Fig. 6.2. In this chapter, the previous works on UPt_3 are reviewed.

6.1 Heavy fermion superconductor

HFS has been attracted much attention as the main street of investigating the unconventional superconductor. It is characterized by the anisotropic superconducting energy gap and its physical quantities obey power law of temperature, while the conventional i.e. BCS-type superconductor has the isotropic energy gap and therefore shows an exponential behavior below T_c.

So far, six HFSs ($CeCu_2Si_2$, UPt_3, UBe_{13}, URu_2Si_2, UNi_2Al_3, UPd_2Al_3) have been reported. Since many of them take along the magnetic ordering, it is natural to consider that those superconductivity have relation with the magnetic fluctuation on the basis of the strongly correlated electrons. Relating to this, some Ce-compounds ($CeCu_2Ge_2$, $CePd_2Si_2$, $CeRh_2Si_2$, $CeIn_3$) are reported to show the superconductivity after supression of the antiferromagnetic ordering under high pressures.

6.2 Previous work on UPt_3

The crystal structure of UPt_3 is shown in Fig. 6.1. The $MgCd_3$-type close-packed hexagonal structure belongs to the space group $P6_3/mmc$. Hereafter, we denote the three crystal axes, respectively $(11\bar{2}0)$ as the crystal a axis, $(10\bar{1}0)$ as the crystal b axis and (0001) as the crystal c axis. The lattice constants are a=5.764Å, c=4.899Åand c/a=0.850.

In Fig. 6.2, the multiple phase diagram of UPt_3 determined by the thermal expansion and the magnetostriction measurement [49] is shown. The same result is obtained from the ultrasonic velocity [50, 52] and the heat capacity [51]. It shows that three distinct superconducting phases (A,B and C) meet at tetracritical point for both directions parallel and perpendicular to the crystal c axis.

Thermal properties of superconductivity are investigated by various experiments [53, 54, 55, 56, 57]. All results show a power law behavior at low temperatures, suggeting the

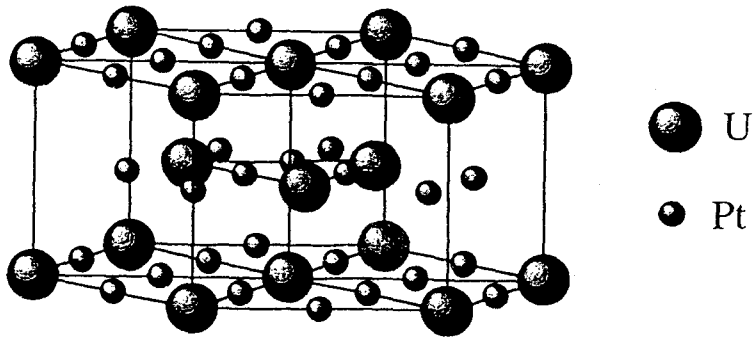

Figure 6.1: Crystal structure of UPt_3.

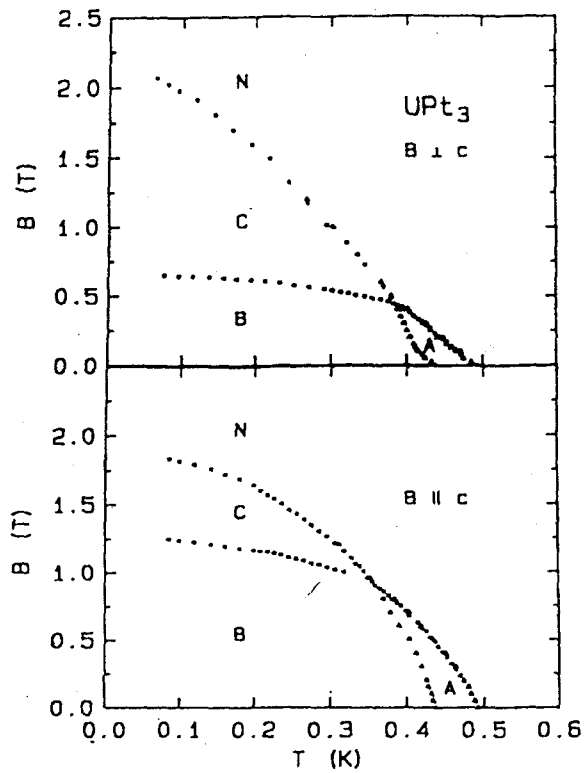

Figure 6.2: Multiple phase diagram of UPt_3 obtained from the thermal expansion and the magnetostriction measurement [49].

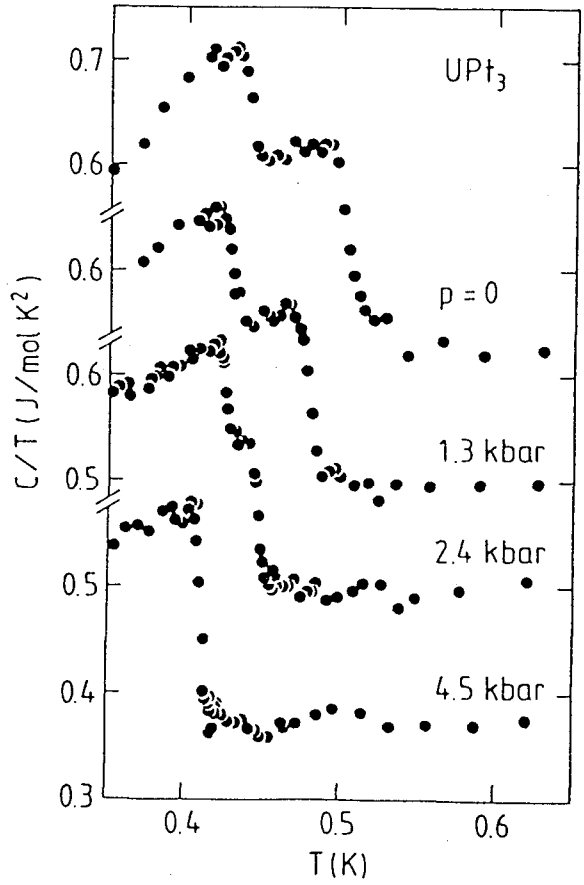

Figure 6.3: Heat capacity of UPt_3 in the vicinity of the superconductive transition by $C/T - T$ plot for various pressures. [60]

unconventional superconducting state of UPt_3.

Applying high pressures, the successive transition under zero external field merges into one [60], as shown in Fig. 6.3. The pressure dependence is alomost linear and the critical pressure P_c, where the tetracritical point lies on the zero field plain, is estimated as $\sim$3kbar. On the other hand, it has been reported that the weak antiferromagnetic ordering (AF), $T_N \sim$5K, which is observed by neutron scattering measurement shown in Fig. 6.4 [58, 59], vanishes under hydrostatic pressures of about 3kbar [61]. (6.5) Therefore, it was considered that AF couples with the superconducting order parameter. However, no other experiment has observed the appearance of AF. As shown in Fig. 6.6, no significant difference of the ^{195}Pt Knight shift is seen above and below T_N [68]. This fact strongly suggests that the magnetic ordering is not static one as before considered.

Above P_c, the agreement of the experimental result is not obtained. M.Boukhny *et al.* argued that T_c split again above P_c by their ultrasonic velocity measurement under uniaxial stress [62], as shown in Fig. 6.7. On the other hand, M.Sieck *et al.* showed that no splitting is seen on their thermometric measurement under hydrostatic pressure [64], as shown in Fig. 6.8. It is the remaining problem if the disagreement between these experiments is caused by the difference of the experimental technique, or by the quality of pressure, or simply by the sample dependence.

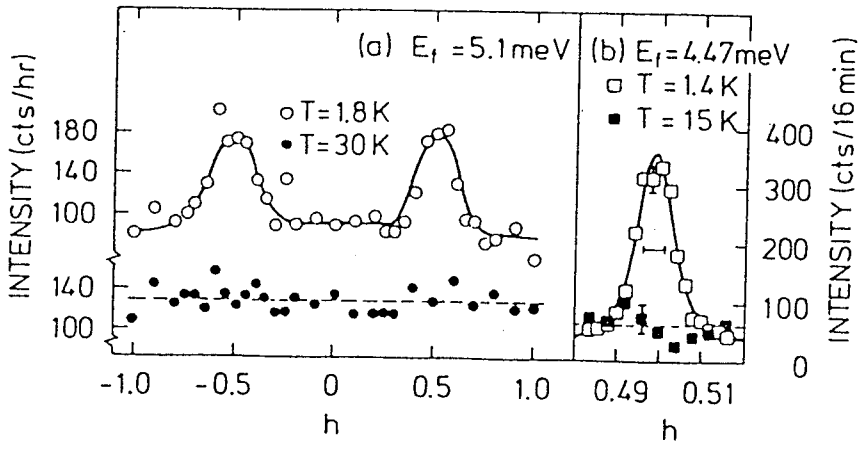

Figure 6.4: Constant-energy scans along (h,0,1) above and below T_N. [58]

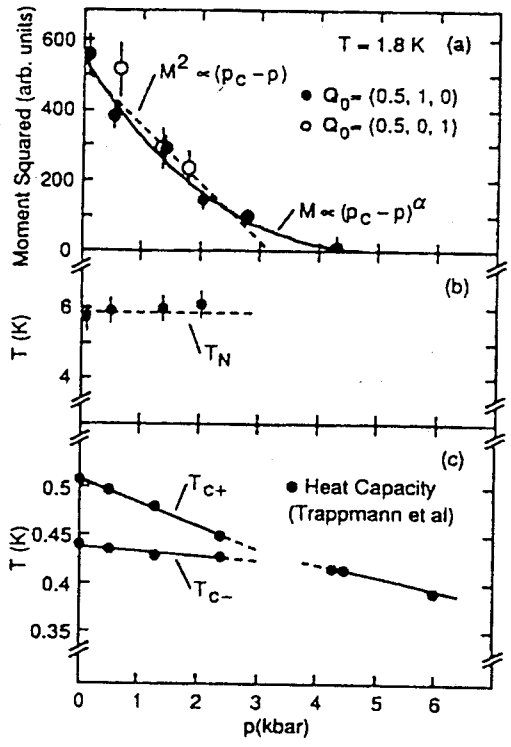

Figure 6.5: (a) Pressure dependences of the integrated intensity of the magnetic peak which means M^2 and (b) the Néel temperature. (c) Upper and lower critical temperature determined from low temperature specific heat. [60, 61]

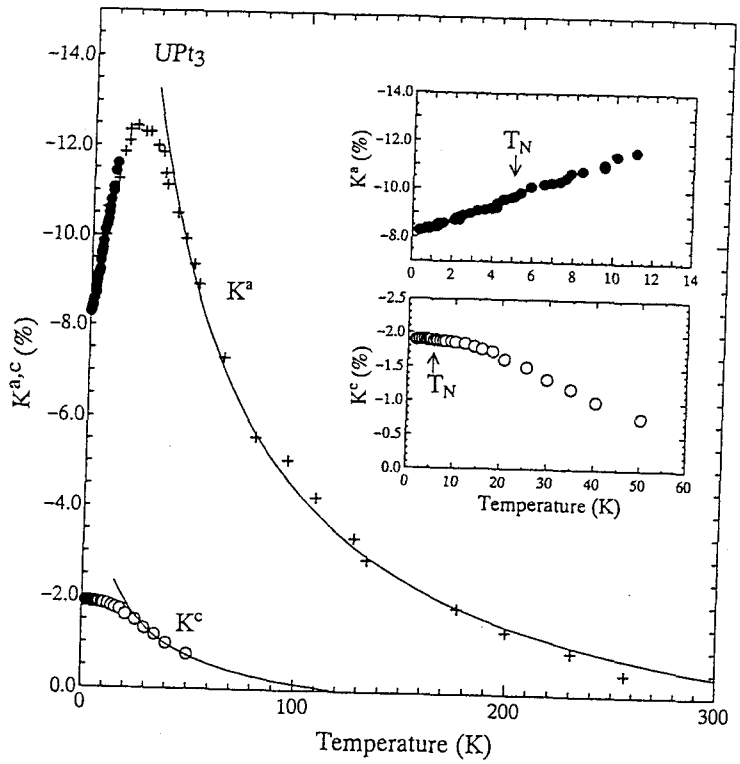

Figure 6.6: ^{195}Pt-NMR Knight shift as the function of temperature along the crystal c and a axes. Insets show the lower temperature side. No singularity is found at around expected $T_N \sim$5K. [68]

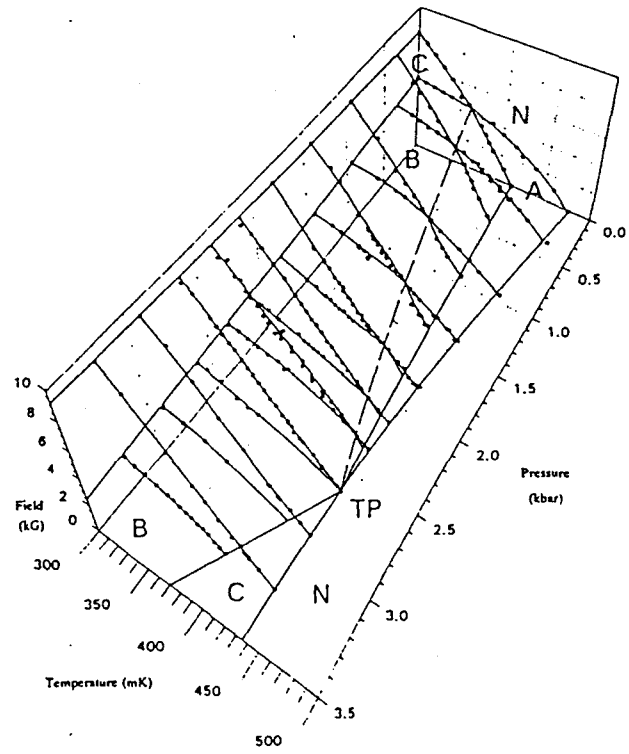

Figure 6.7: H–T–P phase diagram of UPt_3 for $H \perp c$ and uniaxial stress $P \parallel c$ determined by the longitudinal sound velocity variation [62].

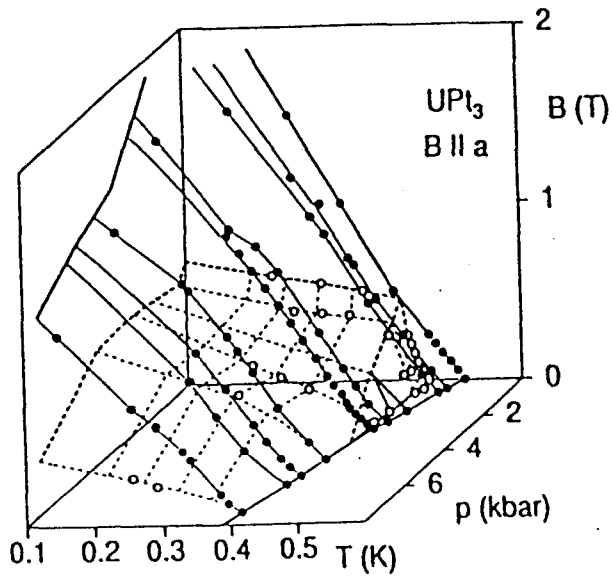

Figure 6.8: H–T–P phase diagram of UPt_3 for $H \perp c$ and hydrostatic pressure determined by specific heat and magneto-caloric effect [64].

Chapter 7

Experimentals

7.1 Sample preparation

Single crystals of UPt_3 used in the present study are prepared in Ōnuki laboratory, Fac. of Science, Osaka University [67]. An U-rod as the starting materials is pre-refined before growing UPt_3, by means of the solid state electrotransport method (SSE) and the zone melting method (ZM). The single crystal of UPt_3 is grown by the Czochralski pulling method (CZ) in the tetra-arc furnace. After the ingot of the single crystal is obtained, it is annealed for 7 days at 1200°C by SSE.

We employed four samples, denoted as #3S, #4, #6 and #18. Each sample is cut from the ingot by an electrode spark cutter after determined crystaline directions by the X-ray Laue method. Characterization by means of electrical resistivity is also carried out by N.Kimura [67]. Some characteristic parameters are summarized in Table 7.1. All samples present quite high quality.

It is noteworthy that the sample #3S and #4 are cut from the same batch which is used in NMR experiments at Osaka University [68, 69] and in magnetization experiments at Hokkaido University [70, 71, 72]. The sample #18 is cut from the ingot after using in neutron scattering measurements at Japan Atomic Energy Research Institute [73], which show the weak antiferromagnetic ordering at around 5K.

		Electrical resistivity ($J \parallel c$)[a]			
	m(g)	$\rho_0(\mu\Omega \cdot \mathrm{cm})$	RRR	Remarks	
#3S	0.152	0.235	511	cubic	($2\times2\times2\mathrm{mm}^3$)
#4	0.328	0.222	540	cylindrical	($3\mathrm{mm}\phi\times2.5\mathrm{mm}$)
#6	1.050	0.174	689	cylindrical	($3\mathrm{mm}\phi\times10\mathrm{mm}$)
#18	0.768	0.217	553	rectangular	($2\times2\times10\mathrm{mm}^3$)

[a]The values of electrical resistivity are quoted from Ref. [67]

Table 7.1: Characteristic parameters of single crystals of UPt_3

7.2 Heat capacity measurement

Experiments were performed with ^{3}He/^{4}He dilution refrigerator made by Oxford instruments, on which either a 2T hand-made superconducting magnet or a 8T magnet could be assembled . The outline of the heat capacity measurement is described in Chapter 2. Measurements at ambient pressure were carried out in the range of temperatures down to 90mK and magnetic fields up to 3T. Under pressures up to 8kbar, measurements were done in the range of temperatures down to 200mK and magnetic fields up to 2T.

It is generally said that U-compound exhibits self-heating due to the radio activity; given by [1],

$$\dot{Q} \sim 6\mu\mathrm{W/mol}. \tag{7.1}$$

Though it produces a constant heat leak of nearly 10nW, it has no significance on measurements within our experimental range.

7.3 Magneto-caloric effect

Measurements of the magneto-caloric effect were carried out both at ambient pressure and under high pressures. This section is devoted to the experimental scheme of the magneto-caloric effect measurement.

7.3.1 Principle of the magneto-caloric effect

In an adiabatic system, if external field shifts by ΔH, the temperature change ΔT is expressed by the following thermodynamic relations;

$$\begin{aligned} \frac{\Delta T}{\Delta H} \simeq \left(\frac{\partial T}{\partial H}\right)_S &= -\frac{\left(\frac{\partial S}{\partial H}\right)_T}{\left(\frac{\partial S}{\partial T}\right)_H} \\ &= -\frac{T}{C_H}\left(\frac{\partial S}{\partial H}\right)_T . \end{aligned} \tag{7.2}$$

The case of $\left(\frac{\partial S}{\partial H}\right)_T < 0$ is well-known as the adiabatic demagnetization cooling method of the paramagnetic spin system, giving $\frac{\Delta T}{\Delta H} > 0$.

In case of superconductor, $\left(\frac{\partial S}{\partial H}\right)_T$ is positive because the superconducting energy gap is suppressed by external magnetic field. Thus, $\frac{\Delta T}{\Delta H}$ reflects the field dependence of the gap and gives evidence of phase transition between the multiple superconducting phases of UPt_3, as reported by B.Bogenberger *et al.* [63].

7.3.2 Measurement procedures

The measurement is performed by the use of the same system for the heat capacity measurement. In a conventional way, continuous sweep of magnetic field yeilds temperature deviation, which is continuously recorded against field, under an adiabatic condition. However,

[1] Of course, the amount highly depends on sample and should be evaluated on each sample.

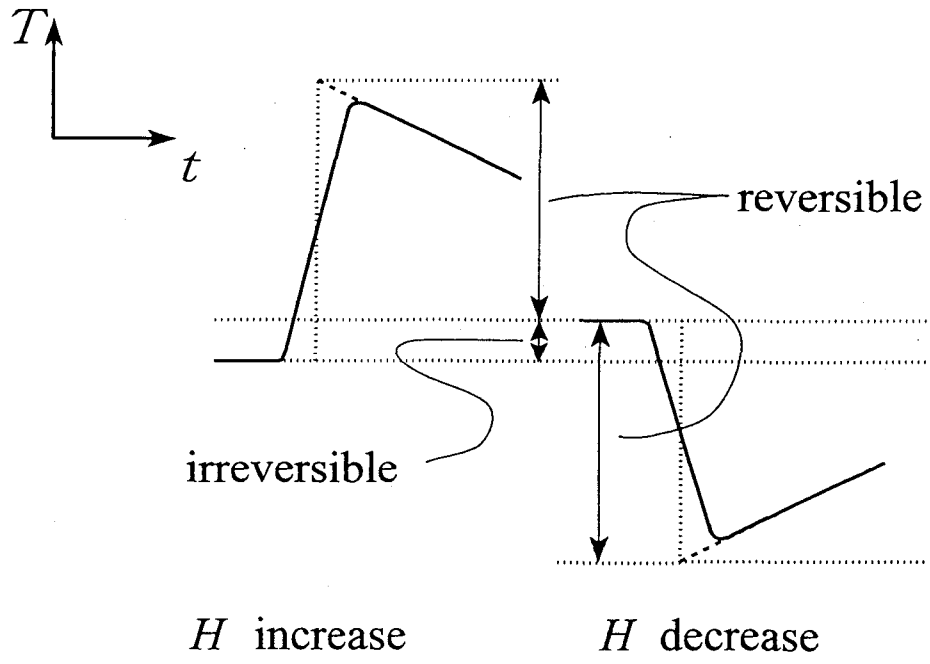

Figure 7.1: Examples of the magneto-caloric effect measurement in case of $\left(\frac{\partial S}{\partial H}\right)_T < 0$. (see text)

quantitative analysis is available by means of field sweeping by a step. It can be also applied to the system which has relatively long relaxation time constant, such a sample as in the pressure cell. The procedure of the measurement is quite similar to that of the heat capacity measurement, as follows;

1. Achieve a quasi adiabatic condition by heating of the additional heater.
2. Increase or decrease the magnetic field by a ΔH.
3. After the field sweep, temperature of the system move to upper or lower side of the equilibrium temperature, and then gradually drifts to the thermal equilibrium by the same manner in case of the heat capacity measurement.
4. Evaluate the temperature difference ΔT by extrapolations of temperature profiles before and after the field sweep, as shown in Fig. 7.1.

Measured ΔT includes both of the reversible and the irreversible temperature deviation to magnetic field. For example, heating by eddy current is the irreversible one. Each contribution can be separated from another by measuring both process on increment and decrement in the same interval of field. Denoting as ΔT_+ for $\Delta H > 0$ and ΔT_- for $\Delta H < 0$, then each part is given as following;

$$\text{reversible part:} \quad \frac{\Delta T_+ - \Delta T_-}{2} \tag{7.3}$$

$$\text{irreversible part:} \quad \frac{\Delta T_+ + \Delta T_-}{2}. \tag{7.4}$$

Furthermore, the contribution from the background can be subtracted though it is a little complicated;

$$dS = \left\{\frac{\partial S}{\partial H}dH + \frac{\partial S}{\partial T}dT\right\}_{\text{sample}} + \left\{\frac{\partial S}{\partial H}dH + \frac{\partial S}{\partial T}dT\right\}_{\text{BG}} = 0$$

$$\left(\frac{\Delta T}{\Delta H}\right)_{meas} \simeq -\frac{T}{C_{\text{sample}} + C_{\text{BG}}}\left\{\frac{\partial S}{\partial H}_{\text{sample}} + \frac{\partial S}{\partial H}_{\text{BG}}\right\}. \tag{7.5}$$

It should be noted that the field dependence of heat capacity is required [74].

In Fig. 7.2, we show some properties of the reversible and the irreversible part of magneto-caloric effect of the pressure cell #1 (see Section 2.4.1) as examples. The reversible behaviors can be about completely explained by eq. (7.2). On the other hand, the irreversible heating is considered to arise from the Joule heating of the eddy current, which is proportional to $\frac{\partial \Phi}{\partial t}$ [2].

[2]The eddy current is in proportion to $\left(\frac{\partial \Phi}{\partial t}\right)^2$, while the duration which the heat is applied is in proportion to $\left(\frac{\partial \Phi}{\partial t}\right)^{-1}$.

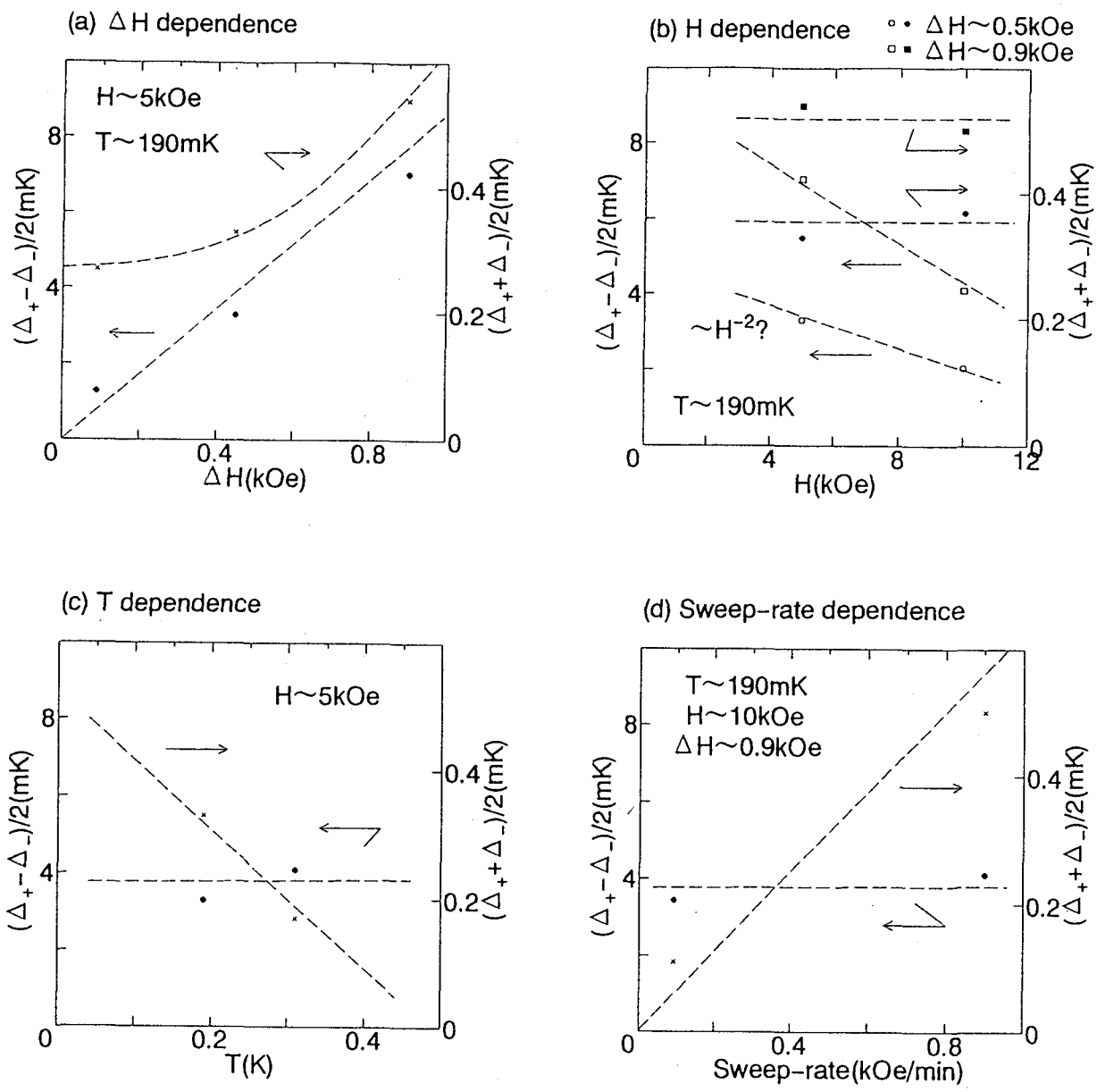

Figure 7.2: Some properties of the reversible and the irreversible part of magneto-caloric effect of the pressure cell #1. The broken lines are guides to the eye. (a) ΔH dependence. (b) H dependence. (c) T dependence. (d) Sweep-rate dependence.

Chapter 8

Results and discussions

8.1 At ambient pressure

8.1.1 Heat capacity

The heat capacity of a single crystal of UPt_3 is shown in 8.1. It clearly exhibits a successive transition, respectively, at T_c^+=0.525K and T_c^-=0.478K under zero external field. Applying the higher external field, these transitions move to lower temperature with approaching each other and under the magnetic field about 0.5T they merge into the single transition. No anomalous peak due to the phase transition between B and C phase is observed.

The heat capacity below T_c obeys T^2 law in the wide range of temperature and it suggests the unconventional superconducting state with the line node on the Fermi surface. However, as lowering temperature, it shows an increment of C/T at around 0.15K. It is considered to associate with the heat capacity anomaly at very low temperatures reported by E.A.Schuberth *et al.* [65]. It is almost field independent up to 2T as well. By extrapolation of the higher temperature region, it shows no residual electronic specific heat.

It should be noted that C/T of the normal state slightly increases with decreasing temperature, leading to a broad maximum at about 0.6K. It may concern with the contribution of the spin fluctuation, $T^3 \ln(T/T^*)$ term, which is observed relatively high temperatures [75, 76].

In Fig. 8.2, the H–T phase diagram of UPt_3 is shown in good agreement with the magnetization measurement by Sakakibara group [70, 71, 72].

8.1.2 Magneto-caloric effect

In Fig. 8.3, the results of the magneto-caloric effect measurement are shown. The contribution from the background, e.g. Cu addenda, is not subtracted yet, so that the absolute value has no significance. However, since the data under higher magnetic field approach zero asymptotically, we consider that those contributions are negligibly small.

Firstly, the reversible part shows the step-like behaviors at H_{BC} and H_{c2} as previously reported by B.Bogenberger *et al.* [63]. It should be noted that the reversible part shows a negative value which is caused by the field dependence of the superconducting energy gap. In spite of the difficulty of the quantitative analysis, it implies the anisotropic behavior of

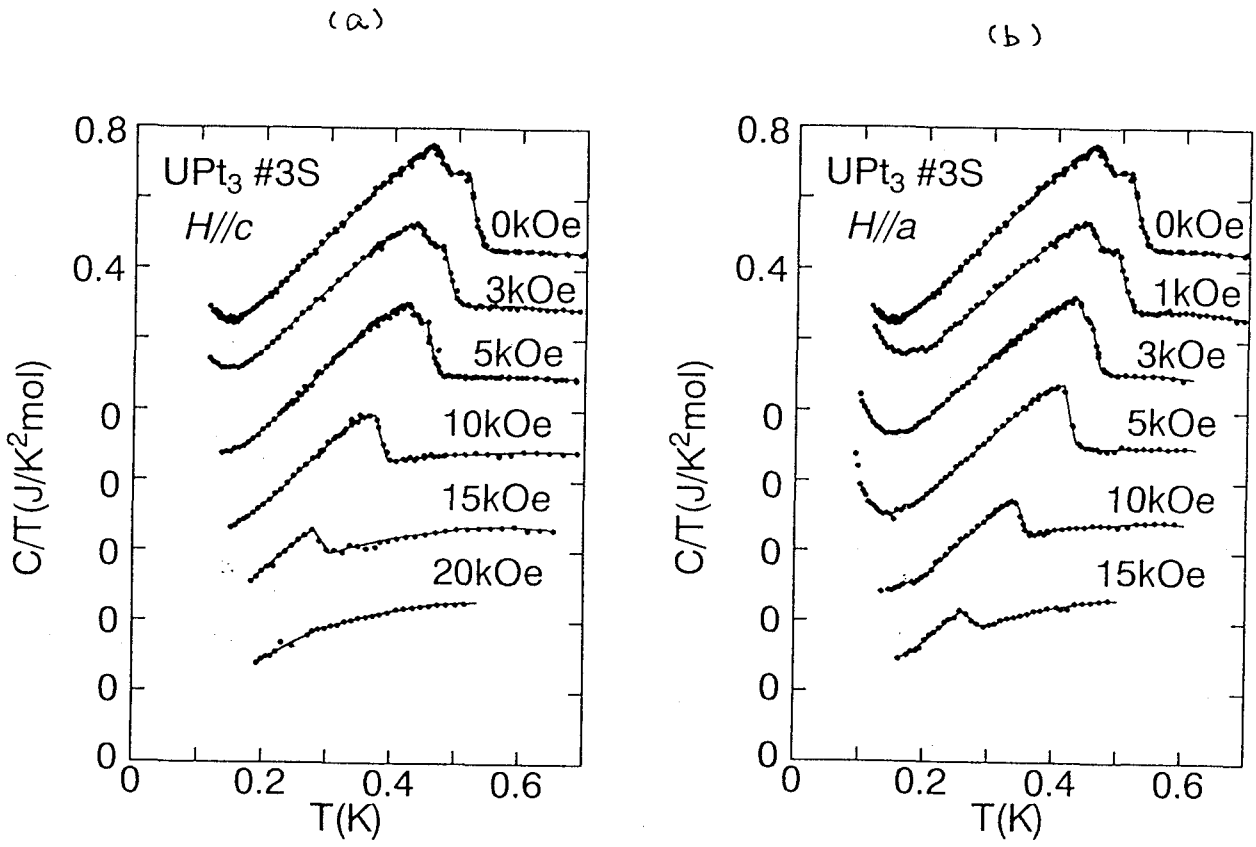

Figure 8.1: Heat capacity of a single crystal of UPt_3(#3S) by $C/T - T$ plot under various magnetic fields applied parallel to the crystal c axis (a) and to the crystal a axis (b). The solid lines are guides to the eye.

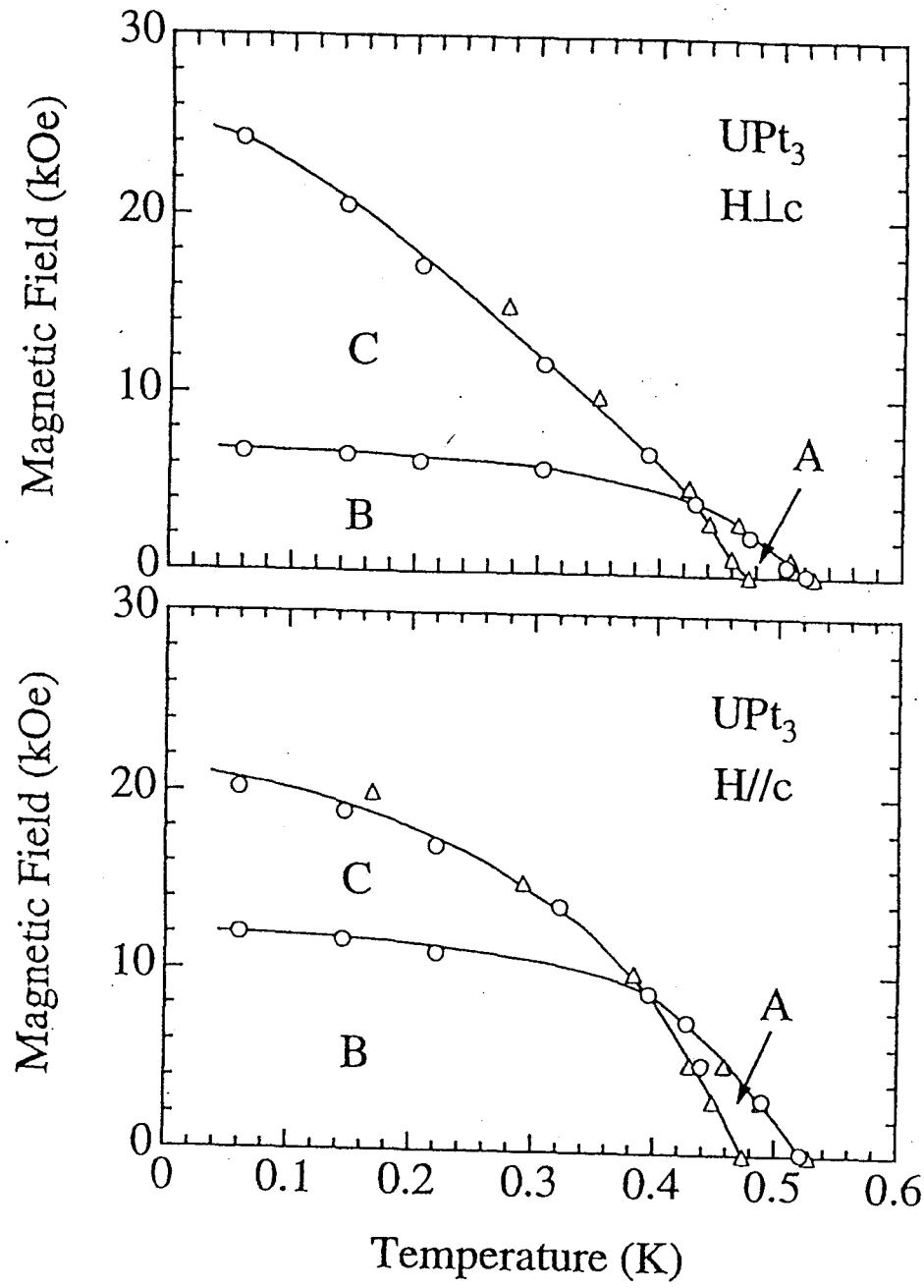

Figure 8.2: H–T phase daigram of a single crystal of UPt_3. The magnetic field applied perpendicular to the crystal c axis and parallel to the crystal c axis. Open circles represent the magnetization measurement by Sakakibara group [70, 71, 72]. Open triangles represent this study. The solid lines are guides to the eye.

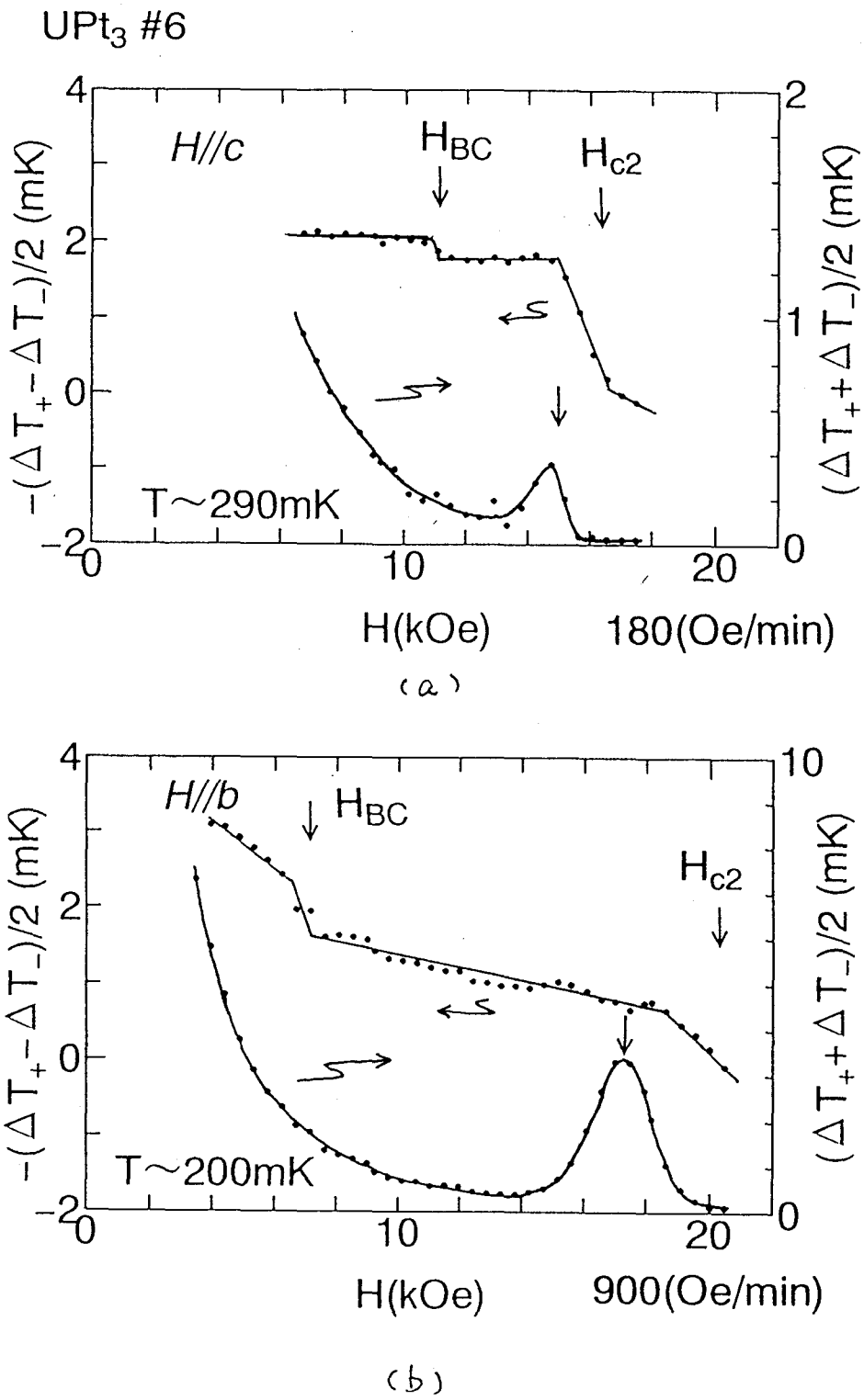

Figure 8.3: Magneto-caloric effect of a single crystal of UPt_3(#6) under the magnetic field up to 2T applied along with the crystal c axis (a) and the crystal b axis (b). The left coordinate and the right coordinate represent the reversible part and the irreversible part, respectively. The arrows respectively indicate H_{BC}, H_{c2} and the anomalous peak of the heat up. The solid lines are guides to the eye. The contribution from the background is not subtracted.

magneto-caloric effect. That is, the change at H_{BC} for $H \parallel b$ is somewhat larger than that for $H \parallel c$.

Secondly, we consider the irreversible part of the magneto-caloric effect. It shows a positive value in the entire magnetic field range, namely heating up. It is noticeable that the irreversible part exhibits an anomalous peak just below H_{c2} and, at lower magnetic fields, the heat up steeply increases with decreasing field. This remarkable feature can not be explained by the heating of the eddy current. We consider that the origin of the heat up is associated with the flux motion. Comparing with the results of the magnetization measurement, the behavior roughly coincides with the hysteresis of the magnetization. It may be interpreted as following. The hysteresis of the magnetization is caused by the flux pinning. In such region of magnetic field, slightly moving fluxes which overcome the pinning potential yield the heating-up. Or, the elastic strain may be caused. Thus the heat up is proportional to the flux pinning force.

It is noteworthy that the anomalous peak just below H_{c2} is attributed to the peak effect of UPt_3. It is suggested that the magneto-caloric effect is available for investigation of the peak effect.

8.2 Under high pressures

8.2.1 Heat capacity

In Fig. 8.4, we show the heat capacity of a single crystal of UPt_3 under hydrostatic pressures up to 8.7kbar. The double peaks of heat capacity due to the successive transition between A and B phases disappears under pressure of ~4kbar. Above P_c, no evidence of the successive transition is obtained within our experimental accuracy. The temperature dependence of the heat capacity of the superconducting UPt_3 is T-square, and no obvious change is observed.

In Fig. 8.5, the heat capacity under pressure of 3.8kbar at various magnetic fields applied along with the crystal c axis is shown. The round shape of heat capacity of normal state devided by T is seen as well, and its broad peak slightly moves to lower temperatures ~0.45K.

The results of the magneto caloric effect under pressure of 4.0kbar is shown in Fig. 8.6. The magnetic field is applied along with the crystal c axis. The contribution of the background is not subtracted yet.

Clear jumps at both H_{BC} and H_{c2} are observed in the reversible part. It should be noted that the anomalous peak of the heat up remains just below H_{c2} in the irreversible part.

In order to establish the H–T phase diagram under high pressures, it is required to measure the magneto-caloric effect at higher temperatures. However, with increasing temperature, the magneto-caloric effect is getting smaller as the heat capacity increases. Moreover, the expected B–C transition moves to lower field side and is covered with the serious heat up of the irreversible part even at T=0.25K. In conclusion, it is difficult to detect the B–C transition at higher temperature and under lower magnetic field by means of the magnetocloric effect because of the heavy irreversible heating.

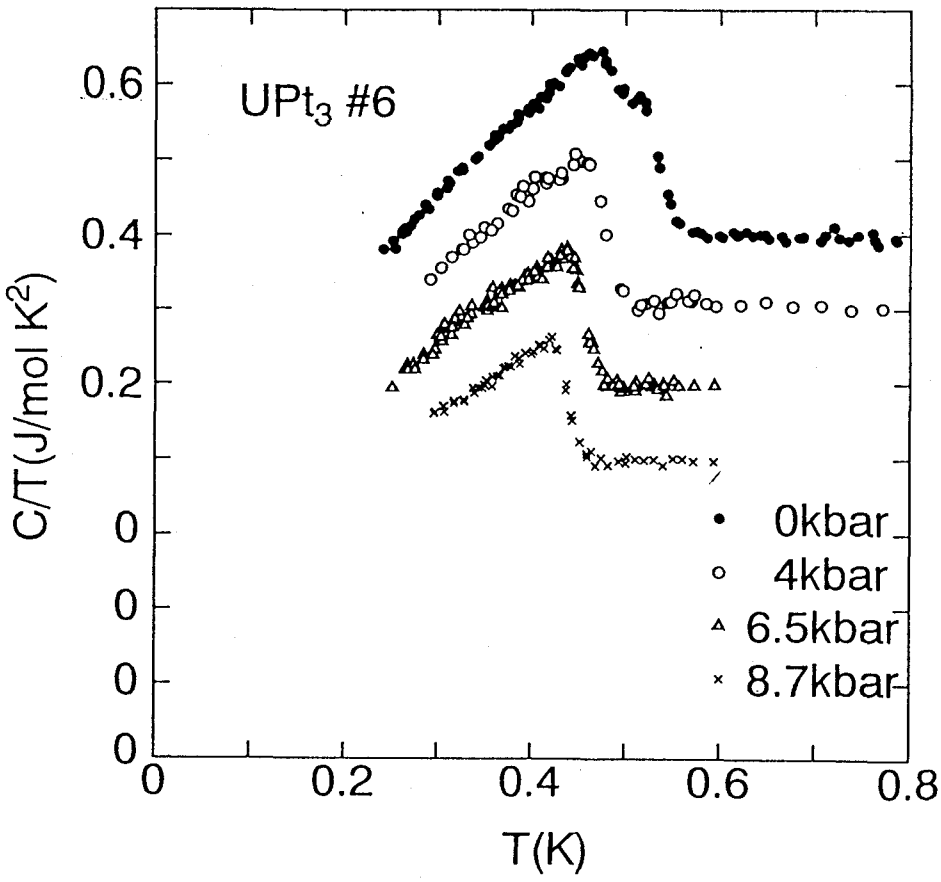

Figure 8.4: Heat capacity of a single crystal of $UPt_3(\#6)$ by $C/T-T$ plot under hydrostatic pressures up to 8.7kbar. To clarify the subsequent runs, the data are shifted by $0.1 J/K^2 mol$.

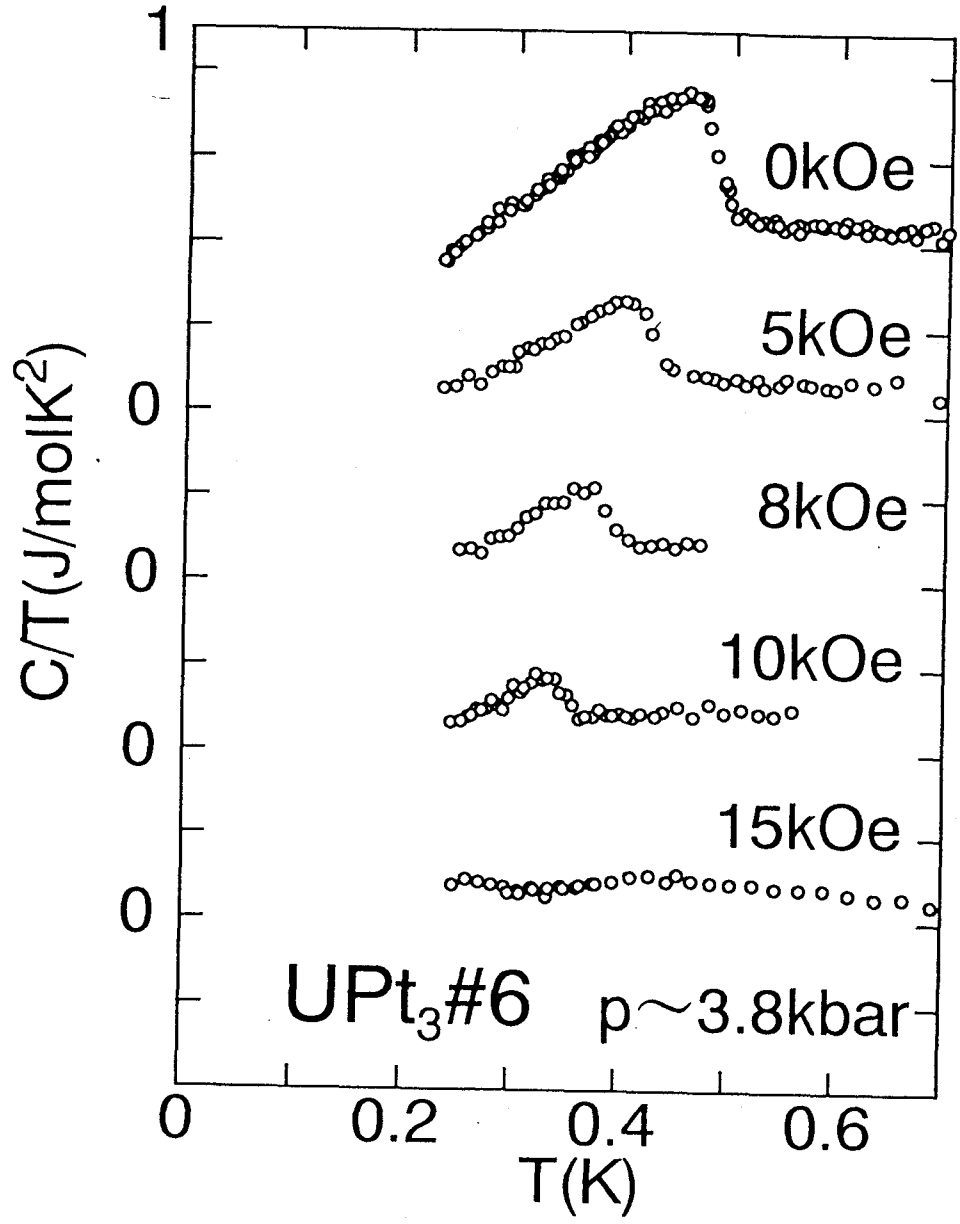

Figure 8.5: Heat capacity of a single crystal of UPt_3(#6) by $C/T-T$ plot under hydrostatic pressure of 3.8kbar and at various magnetic field applied along with the crystal c axis. To clarify the subsequent runs, the data are shifted by $0.4J/K^2mol$.

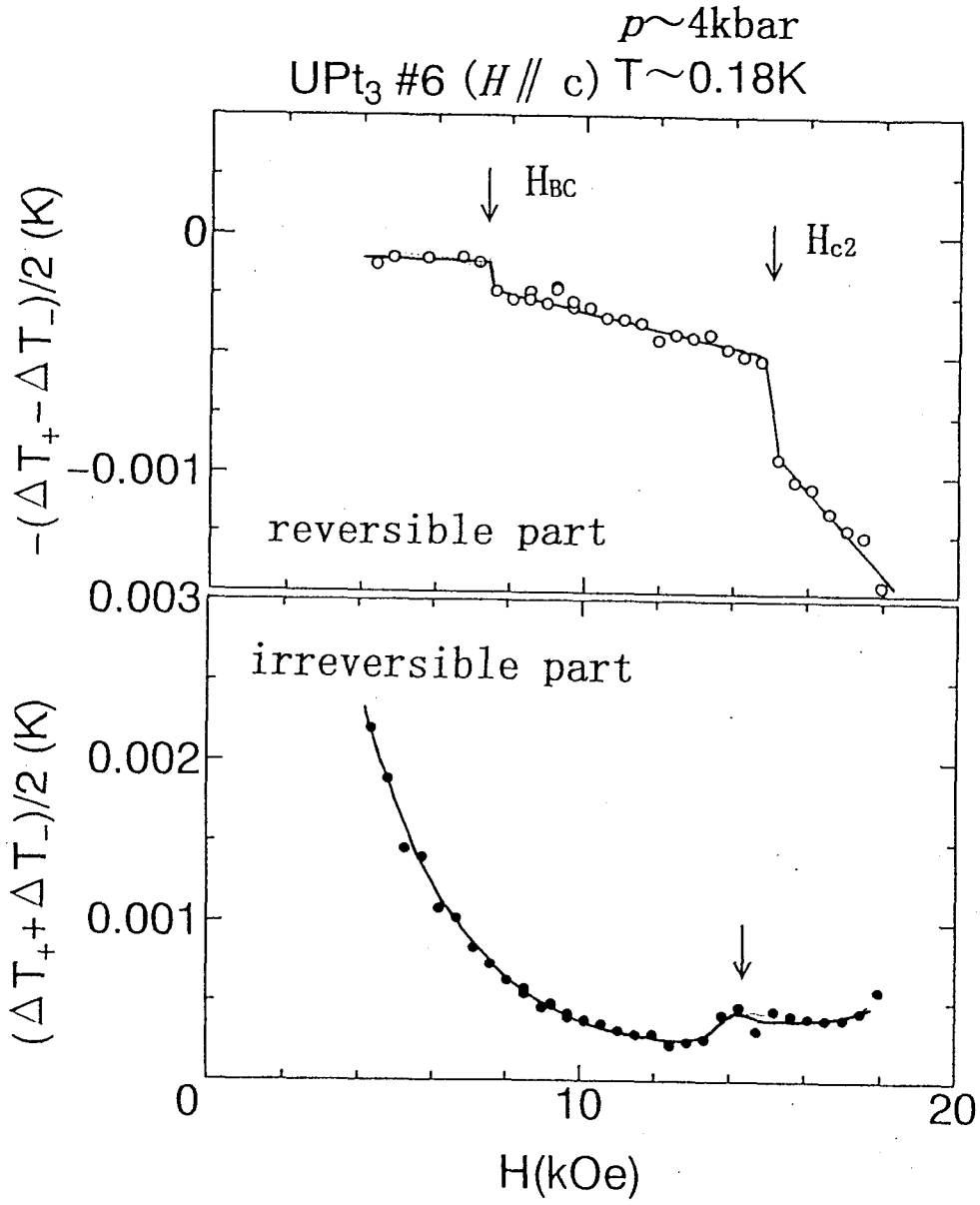

Figure 8.6: Magneto-caloric effect of UPt_3(#6) under pressure of 4.0kbar. The magnetic field is applied parallel to the crystal c axis. The arrows indicate H_{BC}, H_{c2} and the anomalous peak of the heat up. The solid line is guide to the eye. The contribution of the background is not subtracted.

8.3 Summary

We observed that the heat capacity of a single crystal of UPt_3 obeys T^2 law both at ambient pressure and under high pressures. Above P_c, no evidence of the successive transition is seen.

We also carried out the magneto-caloric effect measurement. By analyzing the data separately for the reversible and the irreversible part, it clearly shows the existence of the B–C phase transition and H_{c2}, both at ambient pressure and under high pressures, at reached low temperature. In addition, an irreversible heat up is observed just below H_{c2}, which is attributed to the peak effect. This anomaly remains above P_c.

However, at higher temperatures and under lower magnetic field, it is not able to determine the B–C phase transition and the H–T–P phase diagram is not obtained as the result.

Appendix A

The Automation of the Heat Capacity Measurement

In our laboratory, the heat capacity measurement is performed with a computer controlled system. The fundamental concept of the measurement procedure is discribed in Ref.[77]. Measurement program was originaly written by S.Miyamoto. Later, it has been modified by those who are the predecessors of the heat capacity measurement in Amaya laboratory, S.Kumayasu and Y.Tabuchi. I have made some improvements and source-level diet. In this chapter, the concept of automated measurement is to be appeared. The ability of extention is also discussed.

A.1 Hardware configuration

The temperature of a sample is measured with an AC-resistance bridge, RV-elektroniikka AVS-46, which is in general use of our laboratory. Since the resolution of the original AD converter is $4\frac{1}{2}$ digits, a digital volt meter (DVM), Keithley 196 or 2000, which has the high resolution of $6\frac{1}{2}$ digits and the high accuracy, is connected to an analog output of the bridge in order to read out the resistance.

In ordinary case, two heaters are furnished on the sample addenda. One is to supply a heat pulse and another is to compensate the heat leak, which are called "Main Heater" and "Sub Heater," respectively. Each heater is connected to a programable current generator (CG), Advantest R6142. The minimum presettable output current is 10^{-7}A.

For evaluation of the total amount supplied by a heat pulse, the voltage of the main heater is measured by another DVM. However, if the resistance of the main heater is rather temperature independent, it may be in substitute for this function. (See page 6.)

The whole equipments (except AVS-46) are under the control of a personal computer via the IEEE488 interface bus (GP-IB). The measurement program takes data acquisition every seconds, so that DVMs should be set to make data average within the range of a second.

A.2 Measurement procedure

A.2.1 The heat pulse

A heat pulse is supplied by the Joule heating of the main heater, presented in Eq.(2.3). In a subsequent measurement, the heat pulse to be supplied is estimated by refering the former;

$$\Delta Q = C\{(1+\alpha)T - T\} = \alpha CT\,, \tag{A.1}$$

where α is the ratio of measurement step. Thus the current in the next trial is calcurated as following;

$$\begin{aligned} I_M &= \sqrt{\frac{\Delta Q}{R_M \Delta t}} \\ &= \sqrt{\frac{\alpha CT}{R_M \Delta t}}\,. \end{aligned} \tag{A.2}$$

If there is entirely no reference, e.g. at the first attempt, the heat capacity of the background would be helpful information because the total heat capacity must be larger than it.

A.2.2 Thermal relaxation

After a heat pulse, the system settles down to the thermal equilibium. The profile of the temperature is a mix of miscellaneous thermal relaxation, e.g. the relaxation from the electron spin and the nuclear spin, or the heat leak to the thermal bath, and so on. So one must pay attention when the specimen relaxes thoroughly.

In case of the quasi-adiabatic configuration, thermal impedance between the specimen and the thermal bath is so high that the heat leak to the thermal bath can be considered to be constant, i.e. the relaxation time constant τ_{bath} is to be infinity. Thus the profile of the system is gradually getting to a straight line after the specimen thermaly relaxes.

The program watches out whether the profile may be regarded as a straight line within a given time constant, $\tau_{sample} \ll \tau_{bath}$. If not, it waits repeatedly. When the system fully relaxes, the heat capacity is calcurated by fitting the profile before and after the heat pulse, and the time constant of this measurement is refered by the subsequent trial. If it is longer (shorter) than the given value, the program makes τ_{sample} on the next attempt longer (shorter). How to decide τ_{sample} is mentioned in the following Section A.3.1.

For the later convinience, the profile is recorded as the resistance value because the calibration of thermometer is often improved later. Then, eq. (2.2) is transformed to;

$$C \simeq \frac{\Delta Q}{\Delta R} \cdot \frac{dR}{dT}\,. \tag{A.3}$$

A.2.3 Stabilizing temperature

Heat capacity is nothing but a thermal response of the system. With utilizing it, the temperature is controlable better than that with the PID (proportional, integral and derivative) method, which is the most popular technique.

After the thermal equilibrium is reached, the temperature of the system drifts, obeying eq.2.4. In case $\dot{T}$ is negative, the heat leak can be compensated by heating of an auxilary heater,

$$\dot{Q} + {I_S}^2 R_S = 0\,. \tag{A.4}$$

So the quasi-adiabatic circumstance is achieved.

The current of the sub heater is obtained from Eq. 2.4 and Eq. A.4;

$$\delta I_S = \sqrt{\frac{C\dot{T}}{R_S}}\,. \tag{A.5}$$

The program observes $\dot{T}$ for a duration [1], which is the order of τ_{sample}, and fixes I_S repeatedly;

$$I_S^{next} = \sqrt{{I_S}^2 + \frac{C\dot{T}}{R_S}}\,, \tag{A.6}$$

until it converges within a given range.

A.3 Hints and tips on programing

A.3.1 Finding the thermal relaxation

The key point for the automation of the measurement is how to evaluate the thermal relaxation after the heat pulse. In a usual way, the relaxation process τ is devided into three periods. In the first $\tau/3$, there remains the transient after effect of the heat pulse, or the much faster thermal relaxation within the addenda is in progress. The program treats it as dead time. In the succeeding $\tau/3$, the temperature profile is approximated as straight line by the least squears method. Finaly, the program evaluates how far the points in the last $\tau/3$ deviate from it. If the deviation exceeds the limit which is judged by the observer, the measurement is to be extended further by $\tau/3$ and again evaluated.

Needless to say, the above stated way of the data analysis is one of the many solutions. It ignores how the profile is roundish and how dispersive. In case there exists heat capacities of the nuclear spin, those information may be beneficial. Because the spin-lattice relaxation time constant T_1 is so long at low temperatures that the profile generally shows an overshoot and the following non-linear decay in a long term.

However, though the program shows references, the decision if it is straight or not is up to the observer of the mesurements. The complete automation has no sence. Never forget to keep a ruler in mind.

A.3.2 Single heater method

Usually, the heat leak to the thermal bath is compensated by the sub heater as seen in eq. (A.4). Then the heat pulse may be regarded as an excessive heat flow $I_M^2 R_M$ supplied

[1] Idealy, $\dot{T}$ equals the declination of the thermal relaxation of the previous profile.

by the main heater. If R_M and R_S are the same order, heating by the single heater is equivalent;

$$I_M{}^2 R_M + I_S{}^2 R_S \simeq I^2 R\,. \tag{A.7}$$

It comes that measurements with one heater can be performed. The actual current is

$$I = \sqrt{I_M{}^2 + I_S{}^2}\,. \tag{A.8}$$

In this way, one of two heaters is not necessary and current generators, too. Also the work of the sample stage is made easy. In other words, the measuring apparatus becomes much simplified, giving less the unexpected failure.

However, this method is not necessarily satisfactory. The range of each imaginary I_M and I_S affects the resolution. For example, if the imaginary I_M is 10.00mA, the resolution of the imaginary I_S is limitted to 0.01mA.

A.3.3 A negative heat pulse

In general, heat capacity measurements by the heat pulse method are performed with increasing temperature since the heat pulse is served by the Joule heating in an adiabatic system. However, demands on measuring with decreasing temperature actually exist. For example, the supercooled liquid hydrogen in restricted geometries is believed to be another candidate of the superfluidity. Since the supercooled state is the quasi-stable transient state from liquid to solid, measurements with decreasing temperatures are required. In order to measure the heat capacities of those system, the relaxation method or the AC method are limited choices in usual way.

In case of the single heater configuration, pseudo negative heat pulse can be supplyed. That is to say, in eq. (A.4), the decreace of the current in a certain duration is equivalent to the negative heat pulse.

$$\Delta Q = \left\{(I + \Delta I)^2 R + \dot{Q}\right\} \Delta t \quad \text{for} \quad \Delta I < 0\,. \tag{A.9}$$

Of course, this method premise that there exist large heat leaks to the thermal bath. Under such circumstances, one must be cautious about the temperature gradient between the specimen and the thermometer.

Appendix B

Schottky type anomaly of heat capacity

B.1 2-levels

$$\begin{aligned} z &= 1+\exp\left(-\frac{\Delta}{k_BT}\right) \\ \frac{C}{R} &= \frac{1}{z^2}\left(\frac{\Delta}{k_BT}\right)^2 \exp\left(-\frac{\Delta}{k_BT}\right) . \end{aligned} \tag{B.1}$$

Low temperature approximation [$\exp\left(-\frac{\Delta}{k_BT}\right) \ll 1$]:

$$\frac{C}{R} = \left(\frac{\Delta}{k_BT}\right)^2 \exp\left(-\frac{\Delta}{k_BT}\right) . \tag{B.2}$$

High temperature approximation [$\exp\left(-\frac{\Delta}{k_BT}\right) \simeq 0$]:

$$\frac{C}{R} = \frac{1}{4}\left(\frac{\Delta}{k_BT}\right)^2 . \tag{B.3}$$

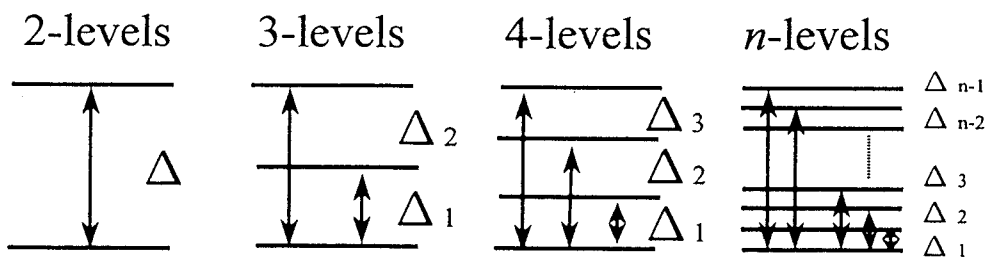

Figure B.1: Notations of the energy levels.

B.2 3-levels

$$
\begin{aligned}
z &= 1+\exp\left(-\frac{\Delta_1}{k_BT}\right)+\exp\left(-\frac{\Delta_2}{k_BT}\right) \\
\frac{C}{R} &= \frac{1}{z^2}\left\{\left(\frac{\Delta_1}{k_BT}\right)^2\exp\left(-\frac{\Delta_1}{k_BT}\right)+\left(\frac{\Delta_2}{k_BT}\right)^2\exp\left(-\frac{\Delta_2}{k_BT}\right)\right. \\
&\quad \left.+\left(\frac{\Delta_1-\Delta_2}{k_BT}\right)^2\exp\left(-\frac{\Delta_1+\Delta_2}{k_BT}\right)\right\}. \qquad \text{(B.4)}
\end{aligned}
$$

In case of $\Delta=\Delta_1=\Delta_2/2$:

$$
\frac{C}{R}=\frac{1}{z^2}\left\{\left(\frac{\Delta}{k_BT}\right)^2\exp\left(-\frac{\Delta}{k_BT}\right)+\left(\frac{2\Delta}{k_BT}\right)^2\exp\left(-\frac{2\Delta}{k_BT}\right)+\left(\frac{\Delta}{k_BT}\right)^2\exp\left(-\frac{3\Delta}{k_BT}\right)\right\}. \qquad \text{(B.5)}
$$

High temperature approximation:

$$
\frac{C}{R}=\frac{2}{3}\left(\frac{\Delta}{k_BT}\right)^2. \qquad \text{(B.6)}
$$

B.3 4-levels

$$
\begin{aligned}
z &= 1+\exp\left(-\frac{\Delta_1}{k_BT}\right)+\exp\left(-\frac{\Delta_2}{k_BT}\right)+\exp\left(-\frac{\Delta_3}{k_BT}\right) \\
\frac{C}{R} &= \frac{1}{z^2}\left\{\left(\frac{\Delta_1}{k_BT}\right)^2\exp\left(-\frac{\Delta_1}{k_BT}\right)+\left(\frac{\Delta_2}{k_BT}\right)^2\exp\left(-\frac{\Delta_2}{k_BT}\right)+\left(\frac{\Delta_3}{k_BT}\right)^2\exp\left(-\frac{\Delta_3}{k_BT}\right)\right. \\
&\quad +\left(\frac{\Delta_1-\Delta_2}{k_BT}\right)^2\exp\left(-\frac{\Delta_1+\Delta_2}{k_BT}\right)+\left(\frac{\Delta_1-\Delta_3}{k_BT}\right)^2\exp\left(-\frac{\Delta_1+\Delta_3}{k_BT}\right) \\
&\quad \left.+\left(\frac{\Delta_2-\Delta_3}{k_BT}\right)^2\exp\left(-\frac{\Delta_2+\Delta_3}{k_BT}\right)\right\}. \qquad \text{(B.7)}
\end{aligned}
$$

In case of $\Delta=\Delta_1=\Delta_2/2=\Delta_3/3$:

$$
\begin{aligned}
\frac{C}{R} &= \frac{1}{z^2}\left\{\left(\frac{\Delta}{k_BT}\right)^2\exp\left(-\frac{\Delta}{k_BT}\right)+4\left(\frac{\Delta}{k_BT}\right)^2\exp\left(-\frac{2\Delta}{k_BT}\right)+10\left(\frac{\Delta}{k_BT}\right)^2\exp\left(-\frac{3\Delta}{k_BT}\right)\right. \\
&\quad \left.+4\left(\frac{\Delta}{k_BT}\right)^2\exp\left(-\frac{4\Delta}{k_BT}\right)+\left(\frac{\Delta}{k_BT}\right)^2\exp\left(-\frac{5\Delta}{k_BT}\right)\right\}. \qquad \text{(B.8)}
\end{aligned}
$$

High temperature approximation:

$$\frac{C}{R} = \frac{5}{4}\left(\frac{\Delta}{k_B T}\right)^2 . \tag{B.9}$$

B.4 n-levels

$$\begin{aligned} z &= 1 + \sum_{i=1}^{n-1} \exp\left(-\frac{\Delta_i}{k_B T}\right) \\ \frac{C}{R} &= \frac{1}{z^2}\left\{\sum_{i=1}^{n-1}\left(\frac{\Delta_i}{k_B T}\right)^2 \exp\left(-\frac{\Delta_i}{k_B T}\right) + \sum_{i<j}^{n-1}\left(\frac{\Delta_i - \Delta_j}{k_B T}\right)^2 \exp\left(-\frac{\Delta_i + \Delta_j}{k_B T}\right)\right\} \end{aligned} \tag{B.10}$$

Acknowledgement

I gratefully acknowledge the valuable advices and the ceaseless encouragement of Prof. K.Amaya. I would like to acknowledge the helpful discussions and the stimulating suggestions of Prof. T.C.Kobayashi.

I am grateful to Prof. Y.Kitaoka and Y.Ōnuki of Osaka University for the valuable discussions and encouragement. I am also grateful to Prof. M.Yamashita of Nagoya University for providing the single crystal of NDMAZ. I would like to thank Dr. N.Kimura of Tohoku University, Dr. R.Settai of Osaka University, Dr. E.Yamamoto and Dr. Y.Haga of JAERI for providing the single crystal of UPt_3.

The high-field magnetization measurement of the single crystal of NDMAZ was carried out at Research center for material science at extreme conditions, Osaka university. I would like to express sincere thanks to Prof. K.Kindo, Dr. Y.Narumi and Mr. K.Tatani for their kind supports.

I wish to thank Dr. H.Tou, Dr. K.Ishida and Dr. K.Shimizu for the helpful advices. I also wish to thank the colleagues of Amaya Laboratory for their cooperations throughout this work.

This work was partially supported by a grant from Research Fellowship of Japan Society for Promotion of Science for Young Scientists.

Bibliography

[1] F.D.M.Haldane, Phys.Rev.Lett. **50** 1153 (1983).

[2] Z.Honda, K.Katsumata, H Aruga Katori, K.Yamada, T.Ohishi, T.Manabe and M.Yamashita: J.Phys.:Condens.Matter **9** L83 (1997).

[3] T.Kobayashi, Y.Tabuchi, K.Amaya, Y.Ajiro, T.Yosida and M.Date: J.Phys.Soc.Jpn. **61** 1772 (1992).

[4] See, for example, *High pressure experimental methods*, M.Eremets (Oxford university press).

[5] H.Bethe: Z.Physik **71** 205 (1931).

[6] L.Hulthén: Arkiv.Mat.Astron.Fysik. **26A** No.11 (1938).

[7] C.N.Yang and C.P.Yang: Phys.Rev. **150** 321 (1966).

[8] R.B.Griffiths: Phys.Rev. **133** A768 (1964).

[9] J.C.Bonner and M.E.Fisher: Phys.Rev. **135** A640 (1964).

[10] P.W.Anderson: Phys.Rev. **86** 694 (1952).

[11] R.Kubo: Phys.Rev. **86** 929 (1952).
R.Kubo: Rev.Mod.Phys. **25** 344 (1953).

[12] J.des Cloizeaux and J.J.Pearson: Phys.Rev. **128** 2131 (1962).

[13] A.R.Miedema, H.v.Kempen, T.Haseda and W.J.Huiskamp: Physica **28** 119 (1962).

[14] T.Haseda and H.Kobayashi: J.Phys.Soc.Jpn **19** 1260 (1964).

[15] K.Takeda, Y.Yoshino, K.Matsumoto and T.Haseda: J.Phys.Soc.Jpn. **49** 162 (1980).

[16] Y.Endo, G.Shirane, R.J.Birgeneau, P.M.Richards and S.L.Holt: Phys.Rev.Lett. **32** 170 (1974).

[17] M.P.Nightingale and H.W.J.Blöte: Phys.Rev. **B33** 659 (1986).

[18] T.Sakai and M.Takahashi: Phys.Rev. **B42** 1090 (1990).

[19] R.Botet and R.Jullien: Phys.Rev. **B27** 613 (1983).
R.Botet, R.Jullien and M.Kolb: Phys.Rev. **B28** 3914 (1983).

[20] J.C.Bonner: J.Appl.Phys. **61** 3941 (1987).

[21] T.Sakai and M.Takahashi: Phys.Rev. **B42** 4537 (1990).

[22] A.Meyer, A.Gleizes, J.J.Girerd, M.Verdaguer and O.Kahn: Inorg.Chem. **21** 1729 (1982).

[23] J.P.Renard, M.Verdaguer, L.P.Renault, W.A.C.Erkelens, J.Rossat-Mignod and W.G.Stirling: Europhys.Lett. **3** 945 (1987).

[24] J.P.Renard, M.Verdaguer, L.P.Renault, W.A.C.Erkelens, J.Rossat-Mignod, J.Ribas, W.G.Stirling and C.Vettier: J.Appl.Phys. **63** 3538 (1988).

[25] S.Ma, C.Broholm, D.H.Reich, B.J.Sternlieb and R.W.Erwin: Phys.Rev.Lett. **69** 357 (1992).

[26] K.Katsumata, H.Hori, T.Takeuchi, M.Date, A.Yamagishi and J.P.Renard: Phys.Rev.Lett. **63** 86 (1989).

[27] Y.Ajiro, T.Goto, H.Kikuchi, T.Sakakibara and T.Inami: Phys.Rev.Lett. **63** 1424 (1989).
T.Goto, H.A.Katori and Y.Ajiro: Tech.Rep.ISSP No.2540 (1992).

[28] T.Sakai and H.Shiba: in *Proceedings of ISSP Symposium on Frotiers in High Magnetic Fields* (1993).

[29] M.Chiba, Y.Ajiro, H.Kikuchi, T.Kubo and T.Morimoto: Phys.Rev. **B44** 2838 (1991).

[30] T.Takeuchi, M.Ono, H.Hori, T.Yosida, A.Yamagishi and M.Date: J.Phys.Soc.Jpn. **61** 3255 (1992).

[31] T.C.Kobayashi, A.Koda, H.Honda, C.U.Hong, K.Amaya, T.Asano, Y.Ajiro, M.Mekata and T.Yosida: Physica **B211** 205 (1995).

[32] J.P.Renard, L.P.Renault and M.Verdaguer: J.de Phys. **49** C8-1425 (1988).

[33] V.Gadet, M.Verdaguer, V.Briois, A.Gleizes, J.P.Renard, P.Beauvillain, C.Chappert, T.Goto, K.Le Dang and P.Veillet: Phys.Rev. **B44** 705 (1991).

[34] L.-K.Chou, K.A.Abboud, D.R.Talham, W.W.Kim and M.W.Meisel: Physica B **194–196** 311 (1994).

[35] H.Deguchi, M.Ito and K.Takeda: J.Phys.Soc.Jpn. **61** 3470 (1992).
M.Ito, M.Mito, H.Deguchi and K.Takeda: J.Phys.Soc.Jpn. **63** 1123 (1994).

[36] T.Kobayashi, A.Kohda, K.Amaya, M.Ito, H.Deguchi, K.Takeda, T.Asano, Y.Ajiro and M.Mekata: J.Phys.Soc.Jpn. **63** 1961 (1994).

[37] H.Mutka, J.L.Soubeyroux, G.Bourleax and P.Colombet: Phys.Rev. **B39** 4820 (1989). C.Playeu, P.Molinie, P.Colombet and G.Fillion: J.Mag.Mag.Mater. **84** 95 (1990).

[38] H.Kikuchi, Y.Ajiro, N.Mori, T.Goto and H.Aruga: Solid.State.Comm. **76** 999 (1990).

[39] A.J.Cox, J.G.Louderbaek and L.A.Bloomfield: Phys.Rev.Lett. **71** 923 (1993).

[40] M.Yamashita: News Letter of the "Molecular Magnetism" No.12 pp.53 (1993).

[41] T.Takeuchi, T.Yosida, K.Inoue, M.Yamashita, T.Kumada, K.Kindo, S.Merah, M.Verdaguer and J.P.Renard: J.Mag.Mag.Matt. **140–144** 1633 (1995).

[42] S.Satoh: Master Thesis, Kyoto University (1996).

[43] T.Sakakibara, H.Mitamura, T.Tayama and H.Amitsuka: Solid State Physics **28** 919 (1993). *in Japanese*

[44] I.Affleck: Phys.Rev. **B41** 6697 (1990).

[45] A.M.Tsvelik: Phys.Rev. **B42** 10499 (1990).

[46] T.Sakai and M.Takahashi: Phys.Rev.**B43** 13383 (1991).

[47] K.Nomura and T.Sakai: Phys.Rev. **B44** 5092 (1991).

[48] E.S.Sørensen and I.Affleck: Phys.Rev.Lett. **71** 1633 (1993).

[49] N.H.van Dijk, A.de Visser, J.J.M.Franse and L.Taillefer: J.Low.Temp.Phys. **93** 101 (1993).

[50] S.Adenwalla, S.W.Lin, Q.Z.Ran, Z.Zhao, J.B.Ketterson, J.A.Sauls, L.Taillefer, D.G.Hinks, M.Levy and B.K.Sarma: Phys.Rev.Lett. **65** 2298 (1990).

[51] K.Hasselbach, L.Taillefer and J.Flouquet: Phys.Rev.Lett. **63** 93 (1989).

[52] G.Bruls, D.Weber, B.Wolf, P.Thalmeier, B.Lüthi, A.de Visser and A.Menovski: Phys.Rev.Lett. **65** 2294 (1990).

[53] K.Bernia, L.Taillefer, J.Flouquet, D.Jaccard, K.Maki and Z.Fisk: J.Low.Temp.Phys. **84** 261 (1991).

[54] G.L.Bullock, B.S.Shivaram and D.G.Hinks: Europhys.Lett. **21** 357 (1993).

[55] B.S.Shivaram, Y.H.Jeong, T.F.Rosenbaum, D.G.Hinks and S.Schmitt-Rink: Phys.Rev. **B35** 5372 (1987).

[56] Y.Kohori, H.Shibai, T.Kohara, Y.Oda, Y.Kitaoka and K.Asayama: J.Mag.Mag.Mat. **76&77** 478 (1988).

[57] C.Broholm, G.Aeppli, R.N.kleiman, D.R.Harshman, D.J.Bishop and E.Bucher: Phys.Rev.Lett. **65** 2062 (1990).

[58] G.Aeppli, E.Bucher, C.Broholm, J.K.Kjems, J.Baumann and J.Hufnagl: Phys.Rev.Lett. **60** 615 (1988).

[59] E.D.Isaacs, P.Zschack, C.L.Broholm, C.Burns, G.Aeppli, A.Ramirez, T.T.M.Palstra, R.W.Erwin, N.Stücheli and E.Bucher: Phys.Rev.Lett. **75** 1178 (1995).

[60] T.Trappmann and H.v.Löhneysen and L.Taillefer: Phys.Rev. B**43** 13714 (1991).

[61] S.M.Hayden, L.Taillefer, C.Vettier and J.Flouquet: Phys.Rev. B**46** 8675 (1992).

[62] M.Boukhny, G.L.Bullock and B.S.Shivaram: Phys.Rev. B**50** 8985 (1994).

[63] B.Bogenberger, H.v.Löhneysen, T.Trappmann and L.Taillefer: Physica **B186–188** 248 (1993).

[64] M.Sieck, H.v.Löhneysen and L.Taillefer: Physica B**206&207** 603 (1995).

[65] E.A.Schuberth, B.Strickler and K.Andres: Phys.Rev.Lett. **68** 117 (1992).
E.A.Schuberth: Int.J.Mod.Phys. **B10** 357 (1996).

[66] A.Sawada, T.Kubo, Y.Fujii, T.Komatsubara, Y.Ōnuki, N.Kimura, E.Yamamoto and Y.Haga: Czech.J.Phys. **46** S2 803 (1996).

[67] N.Kimura: Doctoral Thesis, Osaka University (1997).

[68] H.Tou, Y.Kitaoka, K.Asayama, N.Kimura, Y.Ōnuki, E.Yamamoto and K.Maezawa: Phys.Rev.Lett. **77** 1374 (1996).

[69] H.Tou, Y.Kitaoka, K.Asayama, N.Kimura, Y.Ōnuki, E.Yamamoto and K.Maezawa: Czech.J.Phys. **46** S2 779 (1996).

[70] T.Sakakibara, K.Tenya, M.Ikeda, T.Tayama, H.Amitsuka, E.Yamamoto, K.Maezawa, N.Kimura, R.Settai and Y.Ōnuki: J.Phys.Soc.Jpn. **65** suppl. B202 (1996).

[71] K.Tenya, M.Ikeda, T.Tayama, H.Mitamura, H.Amitsuka, T.Sakakibara, K.Maezawa, N.Kimura, R.Settai and Y.Ōnuki: J.Phys.Soc.Jpn. **64** 1063 (1995).

[72] K.Tenya, M.Ikeda, T.Tayama, T.Sakakibara, E.Yamamoto, K.Maezawa, N.Kimura, R.Settai and Y.Ōnuki: Phys.Rev.Lett. **77** 3193 (1996).

[73] N.Metoki: private communication.

[74] Sato group of Tokyo Metropolitan University perform the measurement of the field dependence of heat capacity and magnetocaloric effect, simultaneously. Firstly, heat capacity is measured at a certain temperature and under a certain external field. Subsequently, magnetocaloric effect is measured with increasing/decreasing to the next target field of the heat capacity measurement.

[75] G.R.Stewart, Z.Fisk, J.O.Willis and J.L.Smith: Phys.Rev.Lett. **52** 679 (1984).

[76] A.de Visser, J.J.M.Franse, A.Menovski and T.T.M.Palstra: J.Phys. F: Met.Phys. **14** L191 (1984).

[77] N.Wada: Solid State Physics **24** 757 (1989). *in Japanese*